

Integration of photo-reactive hydrogels for spatially organized 3D cultures housed in a microfluidic chip

Jennifer E. Ortiz Cárdenas
Luquillo, Puerto Rico

B.A. Chemistry, Binghamton University, 2015

A Dissertation presented to the Graduate Faculty of the University of Virginia in Candidacy for the Degree of Doctor of Philosophy

Department of Chemistry

University of Virginia
August, 2021

Abstract

The research presented in this thesis was conceived as a result of the recent focus on development of organ-on-chip technologies; platforms that aim to emulate at least part of human biology under a controlled environment. These platforms have the long-term goal to serve as a complementary tool to study organ function, model disease, test novel drugs and personalized medicine. While models of various organs have been developed, the lymph node (LN) remains unexplored. Given the important role that the LN plays in immunity, it is vital that a robust model is included amongst all other organs. When considering factors that would create a biomimetic model of the LN both (1) spatial organization and (2) fluid flow control were deemed critical; however, techniques to spatially arrange 3D cultures of primary cells inside microfluidic devices had been limited. This dissertation provides the foundation on how to establish a robust method of micropatterning cell-laden hydrogels on chip and further, it explores ways in which different biomaterials behave under culture conditions. The work will be discussed in two main chapters, followed by a discussion of the necessary next steps to achieve immune function on chip and the vision for subsequent experiments. **Chapter 2** discusses the importance of a multi-assay approach for quality control gelatin-based photo-patternable materials, in order to achieve reproducible results without extensive troubleshooting with every new batch of hydrogel produced. **Chapter 3** provides a detailed account of all necessary components that were optimized to establish a robust photo-patterning set-up, how it was used to assess the performance of gelatin-methacryloyl and gelatin-thiol hydrogels, and investigates how spatial configurations impact the viability of CD4 T cells. Finally, **Chapter 4** will establish the need and approaches to enhance immune cell function within the micropatterned cultures and describes the plans to use spatial

organization as a means to establish and test T-B cell interactions. The work that has been developed and presented in this dissertation will also be useful for the refinement of organ-on-chip platforms to achieve simultaneous control over cellular distribution, local matrix composition, and fluid flow during studies of organized cell-cell interactions in 3D culture.

Acknowledgements

First, I would like to give the biggest thanks to Dr. Rebecca R. Pompano, thank you for being an excellent advisor. From day one, we had a vision of what this project could turn into and slowly but surely, we have seen the team grow and continue to build great things. You've always pushed me out of my comfort zone, motivated me to follow opportunities and offering consistent and thorough feedback. Through your constant support and mentorship, I've become a much better scientist. I am so honored to have been one of the first students in your lab. I cannot wait to see the lab grow even more and be witness to all the things you all will accomplish moving forward.

Dr. Pedro Moreira Allende, tomar tu clase de Biología en décimo grado me cambió la vida. Si hay una persona a la que le debo el nivel de desarrollo profesional que he logrado, es a tí. Además de ser excelente maestro y hacer que me disfrutara la clase como ninguna otra, gracias por reconocer talento que yo misma no pude reconocer, por lanzarme retos y hacer que saliera del pueblo donde me crié a buscar nuevas oportunidades. Por tí me enteré que CROEM existía, tú fuiste quien me dijo que si alguien tenía chance de entrar era yo. Por ese empuje inicial es que estoy donde estoy. Gracias.

A CROEM le debo tanto, como lugar de desarrollo educativo y también como lugar que me brindó amistades para toda la vida. En particular, gracias a Rafael A. López Vargas, mi maestro de Química, que siempre ponía los problemas difíciles que fueron los que me obsesionaron con la materia.

Shanise Kent, I was fortunate to have our paths coincide in Binghamton. Without you, I would not have been introduced to LSAMP which was my entry to research! Thank you for always leaving your office door open so me and everyone else would feel free to come and chat about whatever.

I would also like to thank Dr. Keisha Jones, everybody who gets to meet you it's lucky to. Your care and passion are unparalleled. You have helped so many of us navigate UVA, even when it felt like such a distant place from home.

To LatinX Grad Student Alliance and OURS, although it took until my third year in grad school for these groups to be founded (and for me to even realize how needed they were). I know that your existence will dramatically improve the grad school experience for the next generation of LatinX students at UVA. How could I forget the lunches where we would vent over some Pear Island catering? The best.

To my professors during my spring semester in 2016. Specifically, Dr. Cameron Mura and Dr. Andreas Gahlmann. Thank you both for your understanding and kindness during the most difficult time of my life. And I couldn't forget Dr. Thomas Hall, your incomparable

patience and support was invaluable, I probably would dislike coding way more if it wasn't for you!

I'd like to thank the Biotechnology Training Program, Dr. Gordon Laurie, and all the friends I made outside of Chemistry because of it. The program expanded my professional skills and also gave me opportunities to give back to the local community while having fun with friends outside of campus.

I would like to extend my gratitude to all the Chemistry Department staff, whose hard work on the daily enable us to do our work to the best of our abilities. In particular, I'd like to thank Michael Birckhead who always helped me place orders at the last minute and whose happiness was undeniably contagious! Sandy, thank you for the plants you gifted me, you made my PLSB office much nicer!

To the LN chip team, you all are incredible. Jon, my experience in lab was much lonelier before you joined. Thank you for listening to me at my most frustrated, especially when we could not figure out what the heck was going on with those gels...for months! Thank you specially for always having something grounding to say to me which would help me slow down and allow me to keep pushing forward. Amirus and Tochi, we got so lucky to have you join the team. All three of you have shown me that the best results come from being surrounded by talented and supportive people. To the rest of my labmates, past and present, thank you for the fun times and fostering the collaborative spirit that is so specific to our lab. I wish you all success in your future endeavors.

Tiny and Luna, you'll never be able to read this, but you both bring immense joy into my life just by existing.

Mami y Papi, ustedes han sido mis mayores fans toda mi vida. Desde que me entró la idea de que tenía que estudiar en CROEM y ustedes sin falla conseguian como hacer para que pudiera viejar 3 horas de ida y 3 de vuelta a la esquina opuesta de la Isla todas las semanas. Todo porque creian que mi educación valia la pena. Por el apoyo incondicional durante toda mi carrera y por siempre creer en mi, aún cuando yo siempre ando llena de dudas. Los amo y un día cuando tenga dinero, le voy a pagar a alguien para que traduzca todo este documento y puedan enterarse de todo lo que he hecho.

And last but not least, Maxim. Your support and love have helped me get through the hardest times. You've gone above and beyond my expectations; from leaving NYC to join me in Charlottesville, to sharing a 1-bedroom apartment with my parents for nine months when they got displaced by Hurricane Maria, and so much more. Thank you. We haven't had it easy but I just know that better times are coming for us and now, we know we can take on anything. Oh, and maybe you'll get a chance to skim this document and get a better sense of what "PDMS cell on a chip" actually means. I love you.

Table of Contents

Abstract	ii
Acknowledgements	iv
Table of Contents	vi
Table of Equations	x
Table of Figures	xi
1 Introduction	1
1.1 Tissue Models	1
1.1.1 Background on tissue models	1
1.1.2 Engineered tissue models: organoids and organs-on-chip	2
1.1.3 Role of spatial organization in organ functioning	3
1.1.4 Role of fluid flow in organ functioning	4
1.1.5 Micropatterning of cells	4
1.1.6 Micropatterning on-chip	6
1.1.7 Lymph node as a case study of on-chip micropatterning	14
1.1.8 Existing models of the lymph node	17
1.1.9 Research objectives and concluding remarks	19
1.2 References	21
2 Hydrogel Reproducibility	30
2.1 Abstract	30
2.2 Introduction	31
2.3 Material/Methods	36

2.3.1	Reagents and solvents.....	36
2.3.2	Commercial GelSH	37
2.3.3	Gelatin methacryloyl functionalization.....	37
2.3.4	Gelatin norbornene functionalization.....	37
2.3.5	In-situ rheology measurements.....	38
2.3.6	Ninhydrin assay.....	38
2.3.7	DOF Calculations using NMR	39
2.4	Results.....	40
2.4.1	GelMA batch-to-batch reproducibility and characterization.....	40
2.4.2	GelNB batch-to-batch reproducibility and characterization	43
2.4.3	Commercially available alternatives.....	46
2.5	Conclusion	47
2.6	References	48
3	<i>Micropatterning Hydrogels On-Chip</i>	<i>51</i>
3.1	Abstract	51
3.2	Introduction.....	52
3.3	Materials and Methods	54
3.3.1	Hydrogel materials and sourcing.....	54
3.3.2	Silicon master fabrication	55
3.3.3	Surface functionalization of microfluidic chips.....	55
3.3.4	Assessing patterning resolution	57
3.3.5	GelSH/GelMA characterization and cell encapsulation.....	57
3.3.6	Cell Sourcing.....	58
3.3.7	Photopatterning and viability of murine splenocytes	59

3.3.8	Photopatterning and viability of human T cells (GelSH).....	60
3.3.9	Widefield Imaging.....	61
3.3.10	PDMS bubble trap fabrication	62
3.3.11	Hystem-C hydrogel preparation	62
3.3.12	Permeability of hydrogels.....	62
3.4	Results.....	63
3.4.1	Optimization of microchip design	63
3.4.2	Chip materials and surface modification	67
3.4.3	Equipment Selection: Light Source	70
3.4.4	Selection of light intensity.....	74
3.4.5	Precursor reagents storage and stability: best practices	75
3.4.6	Temperature effects on gelation reproducibility	77
3.4.7	Photopatterning on-chip set up and process.....	78
3.4.8	Precursor formulation for biomimetic storage moduli.....	80
3.4.9	Impact of cell encapsulation in storage moduli as a function of chemistry.....	82
3.4.10	Resolution of features based on gelation chemistry	84
3.4.11	Stability of features based on gelation chemistry.....	90
3.4.12	NHS Rhodamine as a cell tracker	92
3.4.13	Minimization of non-specific cell adhesion via temperature	93
3.4.14	Viability of murine splenocytes based on gel chemistry.....	95
3.4.15	Accessing biomimetic structures via patterning	97
3.4.16	Cell-laden features on-chip	99
3.4.17	Precise patterning of CD4 T cells in GelSH microarray on chip.....	101
3.4.18	Overnight culture of patterned human lymphocytes.....	102
3.4.19	Long term culture conditions: bubbles	105
3.4.20	Permeability of hydrogels as a proxy to mesh density.....	108

3.5	Conclusion	111
3.6	References	112
4	<i>Conclusions and Future Directions</i>	118
4.1	Conclusions	118
4.2	Future Work	118
4.2.1	Enhancing T cell interactions in photopatterned hydrogels.....	118
4.2.2	Establish T-B cell interactions on chip	122
4.3	References	126

Table of Equations

Equation 1-1:.....	7
Equation 1-2:.....	7
Equation 2-1.....	39
Equation 2-2.....	39
Equation 3-1.....	63
Equation 3-2.....	63
Equation 3-3.....	105
Equation 4-1.....	120

Table of Figures

Figure 1-1 Concept figure representing the complexity and set-ups of (a) organoids, clusters of cells resuspended in hydrogels, often cultured on a dish or well plate vs. (b) organs-on-chip, which houses 2D or 3D cultures within a microfluidic chip in a two-compartment configuration which separates two distinct monolayers of cells with the integration of a permeable membrane.	3
Figure 1-2 Popular micropatterning strategies: a) soft-lithography, elastomeric stamps b) bioprinting, fused deposition and c) photolithography using 405 nm light and photoreactive matrix.	5
Figure 1-3 On-chip patterning strategies. a) Example of a patterned culture using physical supports, in the means of micropillars. Reproduced from [61] with permission from the Royal Society of Chemistry. b) Example of patterned channels via coating taking advantage of laminar flow parabolic profile. Reproduced from [58] with permission from the Royal Society of Chemistry.	9
Figure 1-4 Cleavage of lithium acyl-phosphinate (LAP) into two primary radicals upon light exposure.	11
Figure 1-5 Gelatin methacryloyl synthesis and polymerization. (a) Primary amines in a gelatin strand (bold black curve) react with methacrylic anhydride to produce a photoreactive gelatin-derivative containing methacryloyl groups. (b) Schematic of photocrosslinking of GelMA in the presence of a radical (R). Two GelMA strands become covalently bound, forming a hydrogel network. A carbon radical center shown where the reaction would progress.	12
Figure 1-6 Thiol-ene step growth polymerization (a) Reaction scheme between thiol-functionalized gelatin and an 8-arm norbornene-terminated linker. In the presence of light	

and a photoinitiator (P.I.) radical mediate step growth takes place. (b) Mechanism for oxygen scavenging shows that peroxy radicals will abstract a proton from a neighboring thiol group which will further react with other double carbon bonds, propagating the polymerization. 14

Figure 1-7 Key structural features in thick lymph node slices (a) Schematic (b) Female C57Bl-6J mouse LN slice labeled with anti-B220 (FITC, green) and anti-Lyve-1 (eFluor660, purple) revealed key structural features of the lymph node including B cell follicles, lymphatic sinus, and T cell rich zone (B220 dim).⁸ Adapted with permission from *ACS Pharmacol. Transl. Sci.* 2021, 4, 1, 128-142. Copyright 2021 American Chemical Society. 16

Figure 1-8 Lymph node tissue slices a) Schematic representation of slicing the complex three-dimensional lymph node into 300- μ m increments, which yields slices that are heterogeneous in terms of cell population and spatial distribution. B cell follicles shown in green; sinuses in blue. b) Serial 100- μ m thick slices of a fixed lymph node labeled with FITC anti-B220 (green) and Hoechst 33342 (blue) detailing the heterogeneous cell distribution in the lymph node and how it changes with depth in the tissue. Adapted with permission from *ACS Pharmacol. Transl. Sci.* 2021, 4, 1, 128-142. Copyright 2021 American Chemical Society.⁸..... 19

Figure 1-9 Concept schematic of “bottom-up” lymph node chip, process of photopatterning 3D cultures of specific cell types inside of a microfluidic housing to recapitulate key architectural landmarks of the LN. 20

Figure 2-1 Detecting protein functionalization by loss of free amines via the colorimetric ninhydrin assay. (a) Chemical functionalization of a protein by anhydrides or succinimidyl esters occurs primarily at free amines, with minor reactivity towards free hydroxyl and thiol groups (not shown). (b) Reaction products of amine sidechains with methacryloyl or

norbornene groups. (c) In the ninhydrin assay, ninhydrin reacts with free primary amines to generate Ruhemann's Purple, a purple-colored soluble product. (d) The optimized assay with a protein-based standard curve yielded clear solutions, free of precipitation, and a visible color change that corresponded to free amine content in the solution. (e) Functionalized gelatin samples (here, GelMA) produced color changes that inversely correlate with their respective DoF values. Reprinted by permission from Springer, *Analytical and Bioanalytical Chemistry* (2020) 412:6211–6220.¹⁴ 33

Table 2-2 Summary for three different batches of GelMA (synthesized in-house) with DOF's determined by colorimetric assay, NMR and corresponding storage moduli (G') after 60 seconds of exposure. *means the assay was not performed, likely product ran out. + data collected and analyzed by Jonathan Zatorski. 42

Figure 2-2 Comparison of photopolymerization of three distinct batches of in-house produced 8% w/v gelatin-methacryloyl (GelMA) with 0.1% LAP in PBS. (a) Rheometry measurements of the storage modulus of GelMA during *in situ* polymerization. Thick line shows average and dashed lines represent deviation from the mean. Grey shading indicates when light was turned on. (b) Shear storage modulus at different exposure times. Legend indicates different batch synthesis. 43

Table 2-3 Summary for two different batches of GelNB (synthesized in-house) with DOF's determined by colorimetric assay, NMR and corresponding storage moduli (G') after 60 seconds of exposure. *means the assay was not performed, likely product ran out. + data collected and analyzed by Jonathan Zatorski. 44

Figure 2-3 Comparison of photopolymerization of two distinct batches of in-house produced 10% w/v gelatin-norbornene (GelNB) with 15 mM SH and 0.1% LAP in PBS. (a) Rheometry measurements of the storage modulus of GelNB during *in situ* polymerization. Thick line shows average and dashed lines represent deviation from the mean. Grey

shading indicates when light was turned on. (b) Shear storage modulus at different exposure times. Shared legend indicates different batch synthesis. Two-way ANOVA with Sidak's multiple comparisons; *** $p \leq 0.005$ 45

Figure 2-4 Comparison of photopolymerization of two distinct bottles of commercially available gelatin-thiol (GelSH). (a) Rheometry measurements of the storage modulus of GelSH during *in situ* polymerization under light exposure. Thick line shows average and dashed lines represent deviation from the mean. (b) Comparison of shear storage modulus at different exposure times. Grey shading indicates when light was turned on. Legend indicates different bottles same batch synthesis. n.s. $p > 0.05$, * $p \leq 0.05$, via Two-way ANOVA with Sidak's multiple comparisons. 47

Figure 3-1 Micropillar optimization a) Unsuccessful filling with NHS-Rhod labelled precursor. Bubbles accumulate in the chamber and top area of the chamber. Arrows point to "ripped" 100 μm wide micropillars when PDMS was peeled from SU8 master. Scalebar 1 mm. (b) – (c) Modified micropillars showing a successful filling. Dashed lines follow the interface between precursor and air inside the chip, no air gets trapped. 65

Figure 3-2 Optimization of chamber design for efficient filling. a) Examples of microwells and grooves on device substrate contributing to bubble formation on chip. *Reproduced with permission from* [24]. Schematic of (b) original chip design with circular chamber (c) modified chamber with tapered entrance to facilitate filling. 67

Figure 3-3 Chip fabrication and surface functionalization (a) Schematic of chip: thin layer of PDMS bonded to a glass coverslip. (b) Surface functionalization of PDMS. The methyl surface was (i) activated via oxidation with air plasma, followed by (ii) silanization using either thiol-terminated (left) or methacrylate-terminated (right) silane, to match the intended hydrogel. 68

Table 3-1 Summary of PDMS treatment tested to reduce cracks produced during silanization.	69
Figure 3-4 Optimization of plasma treatment. PDMS plasma treated for (a) 80 seconds; cracks in the PDMS, templated hydrogel creating undesired stripe-like pattern. (b) 20 seconds; no cracks developed in the PDMS, smooth pattern achieved. Scalebar 500 μ m.	70
Table 3-2 Compilation of LED light sources tested with comparison in beam irradiance at 365 and 405 nm. Intensity measurements taken at 10 mm from sample, where output beam looked homogenous. *These measurements are somewhat arbitrary since the intensity can be modulated up to \sim 200 mW/cm ²	73
Figure 3-5 Importance of collimated light for micropatterning applications. a) Schematic of highly divergent (incoming rays) passing through a collimator lens only rays that are perpendicular to the surface will get through (collimated rays). b) Sketch of intensity profiles of output beam with and without collimation.	74
Figure 3-6 Optimization of light intensity for photopolymerization of 8% GelMA 0.1% LAP. a) Rheometry measurements of the storage modulus of GelMA during <i>in situ</i> polymerization under light exposure at varied intensities. b) Comparison of shear storage modulus at different exposure times. Legend indicates the light intensity. Grey shading indicates when light was turned on.	75
Table 3-3 Summary of recommended reagent storage/lifetime for hydrogel precursors	76
Figure 3-7 Temperature dependent <i>in situ</i> gelation of 10% w/v GelMA with 0.1%LAP. Grey shading indicates when light was turned on.	78
Figure 3-8 Photo-patterning set-up and process (a) Stepwise schematic of patterning process: 1) The chip was filled with buffer (grey), and 2) the buffer was displaced by precursor (green). 3) A photomask with desired design was aligned against the coverslip,	

supported with a rigid polymer backing (PMMA), clamped (not shown for clarity), and exposed. 4) Unreacted material was removed with a buffer rinse. If needed, the process was repeated with a different precursor to add additional structures. (b) Schematic of photo-patterning set up. The chip was placed upside down on top of two support layers (black) to suspend it below the collimated light source. The channels and chamber of the chip are shown filled with precursor (green). 79

Figure 3-9 (a) Reaction scheme of GelMA (black, reactive carbons in magenta) crosslinking in presence of LAP and 405 nm light. (b) Reaction scheme of GelSH (black, thiol in magenta) with an 8-arm PEG-norbornene linker (grey, NB in green), catalyzed by the photoinitiator LAP and 405 nm light. (c) Rheometry measurements of the storage modulus of GelMA during *in situ* polymerization under constant light exposure at 50 mW/cm². Legend indicates the degree of functionalization (DOF, %) of the gelatin and concentration (% w/v) of GelMA present. n=3. (d) Rheometry measurements of the storage modulus of 5% w/v GelSH during *in situ* polymerization under constant light exposure at 50 mW/cm². Legend indicates the concentration of norbornene, where there is 8 mol norbornene per mol PEG-NB. Lines show mean (solid) and std deviation (dashed), n=3 technical replicates. Grey shading indicates when the light was turned on. 81

Figure 3-10 Impact of cell encapsulation on storage modulus of methacryloyl and thiol-ene hydrogels. (a,b) Shear storage moduli of GelMA and GelSH hydrogels formed in the presence or absence of cells, at varying doses of light, for (c) GelMA (10% w/v) at 32 or 70 % DOF, and (d) 5% w/v GelSH cross-linked with 2.5 or 10 mM norbornene. Legend gives density of human CD4+ T cells, in 10⁶ cells/mL. n.s. p>0.05, * p≤0.05, ** p≤0.01 via Two-way ANOVA with Sidak's multiple comparisons. 83

Figure 3-11 Assessing Pattern Resolution. (a) Fluorescent images of circular hydrogel features patterned on a microfluidic chip. Features ranged from 100-900 μm in diameter.

Shown are features in GelSH with 2.5 mM NB, labelled with NHS-rhodamine, on a chip with a 0.15-mm coverslip. Scalebar 250 μ m. (b-c) Quantification of accuracy. (b) Plot of measured diameter of the hydrogel region versus the diameter of the design on the photomask. Black line represents $y = x$, shown for reference. Measurements were taken after a 30-min incubation and rinse. (c) Calculated percent error of each feature versus the target diameter from the photomask design. The dotted line was drawn arbitrarily at 10% error, and grey area shows values that fall in that region. The shared legend shows 10% GelMA with 70% DOF (n=3) and 5% GelSH with norbornene concentrations of 2.5 mM (n=4) or 10 mM (n=4). Symbols and error bars represent mean and standard deviation; some error bars too small to see. 86

Figure 3-12 Assessing the stability of pattern resolution after incubation. (a-c) Quantification of accuracy between the diameter of the design on the photomask and the resulting diameter of the hydrogel region, measured either immediately after patterning (“patterned”) or after an additional 30-min incubation and rinse (“incubated”). Symbols and error bars represent mean and standard deviation; some error bars too small to see. Significance obtained by Paired T-test, n.s. indicates $p > 0.05$, in all panels. Black line represents $y = x$. (a) data for 1.8 kPa GelMA hydrogel n = 3, $p = 0.0064$. (b) data for 1.8 kPa GelSH, n = 4, n.s. (e) data for 0.17 kPa GelSH, for microfluidic chips made with (left) a 0.15 mm coverslip, n = 4 chips, or (right) a 1 mm glass slide, n = 3 chips. 89

Table 3-4 Stability of patterned hydrogel after overnight perfusion. Reported values are % of successful attempts of features that remained anchored on the chip, as opposed to dissolved or rinsed away, after overnight perfusion. N=4 chips for all hydrogel formulations. (*) indicates not tested due to feature instability at short times. 91

Figure 3-13 Characterization of staining specificity of NHS-Rhodamine on mixed splenocytes. Quantification of (a) Total dead cells with total cell count being a combination

of Calcein (+) cells + DAPI (+) cells, or NHS Rhodamine (+) cells. (b) Actual # of total cell counts by Calcein (+) cells + DAPI (+) cells, or NHS Rhodamine (+) cells. (c) Percentage of cells double stain with NHS+Rhodamine and Calcein or DAPI. 93

Figure 3-14 Rinsing optimization after micropatterning as a function of cell density with a) RT rinse (* $p < 0.05$, One-way ANOVA with Tukey's multiple comparisons) and b) 4°C rinse ($p > 0.05$, One-way ANOVA with Tukey's multiple comparisons). 95

Figure 3-15 Viability of mixed splenocytes after patterning in GelNB, and GelMA. a) Brightfield and b) fluorescence image of splenocytes within GelNB hydrogel, 1 hour after patterning. Cells labelled with Calcein-AM (green) and PI (magenta). c) Quantification of viability 1 hr after patterning. ($p < 0.0001$, One-way ANOVA with Tukey's multiple comparisons). d) Brightfield and e) fluorescence image of splenocytes within GelMA hydrogel, 1 hour after patterning. Cells labelled with Calcein-AM and PI. f) Quantification of viability 1 hr after patterning. Splenocytes retained viability within ~30% of that of fresh, never exposed cells an hour after patterning. (* $p < 0.05$, One-way ANOVA with Tukey's multiple comparisons). 96

Figure 3-16 Geometric versatility achieved by on-chip photo-patterning of GelSH hydrogels. (a) NHS-rhodamine-labelled hydrogel (magenta) used to pattern a curved fluidic path in culture chamber. (b) A central circular island (magenta) surrounded by NHS-fluorescein-labelled GelSH (green). (c) Concentric circles patterned with hydrogel labelled with NHS-rhodamine and NHS-fluorescein in three sequential steps. (d) A patterned UVA Rotunda in three sequential steps. The corresponding photomasks used to achieve patterns are shown above each panel. All scalebars are 500 μm 98

Figure 3-17 In situ photo-patterned cell-laden hydrogel constructs. (a) Fluorescence and (b) brightfield images of a patterned 3D cell culture (cells labelled magenta), patterned into two self-standing lobes. A linear fluidic path was patterned between them, and a second,

curved fluidic path surrounded them for better distribution of media. (c) Fluorescence and (d) brightfield images of two distinct cell populations patterned into a lobular organ geometry. First cell population labelled with NHS-rhodamine (magenta); second population labelled with CFSE (green). Inset shows magnified boundary between two patterned regions. Scale bar is 500 μm in (a-d), 250 μm in inset. Dashed lines denote the boundary of the hydrogel regions; solid white lines indicate the edges of the microfluidic culture chamber. 100

Figure 3-18 Precision of photo-patterned microarray of human CD4 T cells on chip. (a) Nine-circle culture array patterned on-chip with cells pre-labelled with NHS-rhodamine. Scalebar 250 μm . (b) Quantification of cell density inside and outside of the patterned regions in GelSH hydrogels (n=2 and n=3 chips respectively). Two-way ANOVA with Sidak's multiple comparisons; **** $p \leq 0.0001$, ** $p \leq 0.01$ 102

Figure 3-19 Overnight viability of CD4 T cells in patterned cultures. (a) Photo-patterned 3D cultures on chip. White boxes denote "outer" and "inner" areas. Dashed lines represent fluid flow pathways. Scalebar 500 μm . (b) Zoomed-in representative image of yellow outlined-region shown in 1a. Fluorescent image of patterned 3D culture, stained with live (green-Calcein AM) / dead (blue-DAPI) stain after 18 hours of culture under fluid flow. Scalebar 200 μm . (c) Quantification of viability 18 hrs post-patterning. No significant difference was observed between live control and "outer regions." One-way ANOVA, n=5. (d) Nine-circle culture array patterned on-chip. Scalebar 250 μm . (e) Zoomed-in view of 3D culture row from panel d. (Left) Image of NHS-rhodamine labelled cells; (Right) image after viability staining with Calcein-AM (green) and DAPI (blue). Scalebar 250 μm . (f) Quantification of the viability of patterned CD4+ T cells in 5% GelSH with 2.5 and 10 mM NB hydrogels as a function of feature dimensions after overnight culture under continuous

fluid flow, versus off-chip (2D) controls (n.s. $p > 0.05$, ** $p \leq 0.01$ One-way ANOVA with Tukey's multiple comparisons, $n=3$ and $n=2$ for 10 mM and 2.5 mM NB chips, respectively)..... 104

Figure 3-20 PDMS bubble trap fabrication and final connections to pump and chips. Channels (light grey), PDMS (aqua) and coverslip (dark grey), arrows (red) show path for bubbles (dashed) and bubble-free fluid. 107

Figure 3-21 Assessing permeability of hydrogels (a) Assay set-up. (b) Measured permeability of various formulations of hydrogels. * $p \leq 0.05$, ** $p \leq 0.01$, *** $p \leq 0.005$ via One-way ANOVA with Tukey's multiple comparisons, all statistical comparisons are between that sample and Hystem-C, all other comparisons were n.s. >0.05 110

Table 3-5 Formulations for GelSH hydrogels tested for permeability. Except where noted [SH] was based on contribution from GelSH and [NB] contribution was based on 8-arm PEG-NB 20 kDa..... 111

Figure 4-1 Synthesis of gelatin microspheres on chip. (a) Schematic of microsphere generation using T-junction microfluidic device. Carrier (yellow; oil phase) and aqueous gelatin solution (blue). Droplets generated and collected in a centrifuge tube. (b) Gelatin microspheres (blue) embedded in crosslinked matrix (black wavy lines). After hydrogel is formed, it is placed in 37C which dissolves the gelatin, leaving behind a macro-porous scaffold..... 121

Figure 4-2 Current approaches to modeling T cell (green) - DC (yellow) interactions. a) Pairwise trapping of cells in microwells. b) 2D monolayer of cells with cell suspension added above. c) 3D culture of mixed cells. d) Cells seeded in distinct regions of a microchip to investigate chemotaxis..... 123

Figure 4-3 T_{FH} cells (blue) and B cells (green). a) Mixed population of T and B cells. In the absence of SEB, cells will be scattered heterogeneously across hydrogel, whereas in presence of SEB will form T-B conjugated. b) Separated two-region co-culture of T and B cells, in biomimetic organization of B-cell follicle/T cell zone. 125

Some of the figures included in this document were created with Biorender.com

1 Introduction

1.1 Tissue Models

1.1.1 Background on tissue models

Organs in our body are composed of the intricate arrangement of various components: cells, proteins, vasculature and biochemical signals.¹ Studying intact organ tissue is attractive because of the retention of native microenvironment experienced in the body which can lead to better recapitulation of complex events that are mediated by cell–cell and cell–matrix contacts and/or by local accumulation of secreted growth factors.² To that end, many labs have adopted precision cut tissue slices as a “top-down” approach to study organ behavior like heart,³ liver,⁴ brain^{5,6} and lymph nodes^{7,8} outside of the body. However, the majority of analytical fields have focus on developing assays for studying more popular reductionist platforms like 2D culture (cell suspensions) or purified samples. Studying intact tissue can be cumbersome because of complications of non-specific adsorption to ECM components, problems with delivery through thick sections. Development of tissue models in a “bottom-up” manner offer additional control over composition and the complexity of the platform can be increased as needed.

The engineering of biomimetic tissue models offers the potential to replicate at least a portion of, human biology in a controlled system. The concept of engineering a tissue-model *ex vivo* follows the premise that if you place the appropriate cell types within a biodegradable structure that mimics some features of the target organ and supplement them with the appropriate mixture of substances for survival, it will lead to a physiologically relevant platform.⁹ These platforms could then be applied to develop a deep

understanding of how groups of cells or tissues interact with the microenvironment in the body including but not limited to: neighboring cells, biomechanical forces, chemical stimuli and particularly the combination of these interactions can lead to organ function. In the future, the hope is that these platforms could be used to confidently test different drug therapies for pharmacological screening and for personalized medicine applications.^{10,11}

1.1.2 Engineered tissue models: organoids and organs-on-chip

There are currently two main approaches to engineer tissue models: biomaterials-based organoids and microfluidic organs-on-chip (Figure 1-1). Organoid development often relies in the self-organization of stem cells or organ-specific progenitor cells into complex architectures or functionalities reminiscent of native tissue or organs.¹² Cells are seeded on top of or resuspended in porous 3D matrices that are either naturally derived, like gelatin and Matrigel, or that have been engineered to match the composition and/or mechanical properties of the native matrix where the cells reside *in vivo*, usually under static conditions. More specifically, these matrices are often optimized in: (1) composition, to include specific glycosaminoglycans like hyaluronic acid^{13–15}, proteins like fibrinogen^{16,17} and other biochemical cues to trigger specific cell behavior like growth factors^{18,19} (2) biomechanical properties like viscoelasticity, stiffness, porosity and permeability. The fine tuning of these properties have enabled the development of powerful organoid systems of lung bronchi²⁰ and B cell follicle germinal centers²¹, for example. A disadvantage of organoid development is that they are seldom incorporated with fluid flow; a biological phenomenon that has been shown to induce or be critical for differentiation of specific cell types^{22–24} or and creation of vasculature^{25–27}, for example.

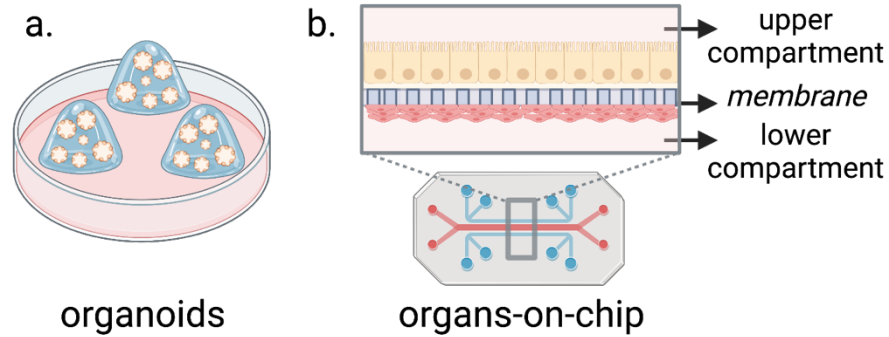


Figure 1-1 Concept figure representing the complexity and set-ups of (a) organoids, clusters of cells resuspended in hydrogels, often cultured on a dish or well plate vs. (b) organs-on-chip, which houses 2D or 3D cultures within a microfluidic chip in a two-compartment configuration which separates two distinct monolayers of cells with the integration of a permeable membrane.

On the other hand, organ-on-chips places cell populations in microfluidic devices in order to enable controlled fluid flow for both nutrient and stimulant delivery. A popular configuration for organ-on-chip platforms is the use of permeable membranes to compartmentalize cell types into distinct regions of a microchip. This allows seeding of cell monolayers on either side of the membrane, while cell communication can still take place through secreted factors. This membrane-based set up has been successfully applied to establish models of different organs, or organ sub-structures, including lung²⁸, kidney²⁹, blood-brain barrier^{30,31}, and liver.³²

1.1.3 Role of spatial organization in organ functioning

Spatial organization is critical to the correct functioning of organs in the body and thus, to keep us alive. Organs are made up of collections of tissues which are combinations of cells at very high densities ($\sim 10^8$ - 10^9 per mL) surrounded by extracellular matrix components, biochemical signals, some connection to vasculature and in some cases stromal networks.³³ Organs have developed over millions of years to capture the

perfect arrangement to allow for efficient and effective cell communication within tissue and carry out organ specific functions. It is understood that disruptions to the organization and thus functioning of the tissue results in disease.³⁴ Therefore, a deep understanding and recapitulation of the cellular components within a tissue are critical when developing biomimetic models of particular organs.³⁵

1.1.4 Role of fluid flow in organ functioning

The total body water content is estimated to be 60% of body weight in men and 50% of body weight in women, with slight variations based on age, body composition, and other factors.³⁶ For a ~154 lb person, total body water is distributed among three types with the following approximate percentages of total body weight: intracellular (33%); interstitial (22.5%); and circulating plasma (4.5% of body weight).³⁷ Cells are bathed in interstitial fluid (IF), given the fact that IF only accounts for only a little more than half the intracellular fluid volume, IF cannot be considered a large reservoir of fluid, and its composition is directly influenced by cellular metabolism.³⁷ As long as cells are alive, they are consuming nutrients and oxygen. If cells were only to rely on the nutrients available in the IF, they could not survive for very long. The circulatory system has evolved the movement of fluid using convection in order to provide constant replenishment of necessary components in the IF, as well as to remove undesired byproducts, or metabolic waste exchange.³⁷

1.1.5 Micropatterning of cells

Current micropatterning techniques for 3D cultures include soft-lithography (microcontact printing and molding), bioprinting, and photolithography (Figure 1-2). Soft-lithography relies on elastomeric stamps or molds to promote selective cell or matrix adhesion³⁸ or directly cast 3D matrices.³⁹ It is simple to use, but requires multi-step

fabrication of a new stamp or mold for each pattern. In contrast, modern bioprinting allows for rapid prototyping of biomaterials in varied patterns based on digital designs, and can generate self-standing 3D cultures at the ~ mm length scale, with no need of physical supports. However, requirements for specific viscosities and surface tensions in extruded hydrogels restrict the options for the culture matrix.^{40,41} On the other hand, photolithography uses light to transfer designs from a photomask to a photo-crosslinkable culture matrix, to generate self-standing 3D cultures. Photolithography may offer higher spatial resolution than extrusion-based printing of bioinks. A significant advantage of this method is the ability to modulate the mechanical properties of the hydrogel, e.g. to match those of a particular tissue, by optimizing the chemical composition of the gel and dose of light, regardless of viscosity. Due to the risk of phototoxicity, photopatterning has been primarily used to pattern hydrogels without cells or was limited to patterning hardy cell lines.⁴²⁻⁴⁴ Photolithography is most commonly used to pattern hydrogels onto coverslips or other substrates that are rarely integrated with a flow control system.⁴⁵⁻⁴⁷

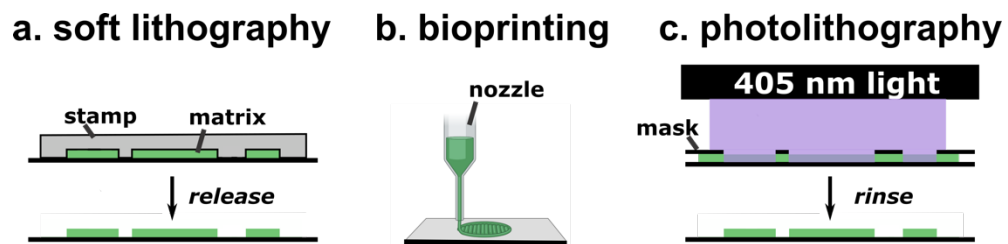


Figure 1-2 Popular micropatterning strategies: a) soft-lithography, elastomeric stamps b) bioprinting, fused deposition and c) photolithography using 405 nm light and photoreactive matrix.

1.1.6 Micropatterning on-chip

1.1.6.1 Microfluidics background

Microfluidics refers to a field that deals with fluids at the scale of nano (nL) to microliters (μL) housed in devices that contain channels that range from micrometers (μm) to a few millimeters (mm). While the field of microfluidics is said to have multiple parents, many consider microelectronics or microelectromechanical systems (MEMS), in particular, to be the most recognizable.⁴⁸ Microfluidic adopted the MEMS fabrication technique, photolithography, which was invented in the 1950's as a result of military needs to integrate small electronic circuits into military proximity fuses. The same technology used to create circuits, was envisioned to be employed to create enclosed channels on silicon substrates for chemistry-based applications such as gas chromatography.⁴⁹

In 1998, the Whitesides group introduced the use of a polymer, poly(dimethylsiloxane) (PDMS), as a more cost-effective alternative to prototype microfluidic devices.⁵⁰ The elastomeric properties of PDMS were attractive because it meant the material could be poured over a silicon-substrate then cured and peeled off, retaining the intricate patterns from the parent mold. PDMS came with additional advantages that made it useful for applications with life sciences, particularly to integrate cell culture on-chip due to the optical transparency, gas permeability, and non-toxicity. Additionally, the enclosed configuration of channels in a PDMS chip allow for integration of fluid flow to cell cultures, a process that can mimic the different vasculature in the body.

Microfluidics offers many advantages including (1) minimization of reagent and sample consumption, (2) in many cases faster reaction times and (3) a whole new world of physics to take advantage of. Because microfluidics operates at a dramatically different scale than regular benchtop laboratories do, some forces become dominant over those to

which we encounter daily. More specifically, concepts like laminar flow and surface tension must be well understood in order to take full advantage of what microfluidics has to offer.

The flow regime of a fluid can be considered turbulent or laminar; The difference between these two regimes is dictated by the ability to predict the position of a particle in the fluid stream as a function of time. In the case of turbulent flow, position of a particle is unpredictable because the fluid is considered chaotic, while in laminar flow all the particles in a fluid follow the same parallel “orderly” path.⁵¹ The Reynolds number is a unitless value that helps determine whether the flow is turbulent or laminar. The Reynolds number (Re) can be calculated by the following equation:

Equation 1-1:

$$Re = \frac{\rho v D}{\mu}$$

in which ρ is the density (kg/m^3), v is the velocity of the fluid (m/s), L is the hydraulic diameter (determined by the channel’s geometry) (m), and μ is the dynamic viscosity of the fluid (kg/m s). When $Re < 2300$, the fluid is considered laminar. As the Re approaches 2300, the fluid will start to show signs of turbulence and will become turbulent by the time is greater than 2300.

Surface tension stems from the cohesions between molecules at an interface. Molecules in a bulk medium are attracted to each other through van der Waals forces or dipole interactions, but at an interface (like liquid/gas) molecules will experience an uneven force since the attractive forces from the alternate medium will likely differ from the medium they are in. The difference in the cohesive energy pulling a molecule into and out of its bulk medium is represented by surface tension. We can find the pressure (force) generated by a liquid surface using the Young-Laplace equation:

Equation 1-2:

$$\Delta P = \gamma \left(\frac{1}{R_1} + \frac{1}{R_2} \right)$$

where γ is the surface tension (or the surface free energy of the liquid) and R_1 , R_2 are the perpendicular radii of curvatures of some point on the surface. This force is a result of surface tension, because a greater curvature leads directly to a greater imbalance between the internal and external cohesive energy of surface molecules.⁵²

Both laminar flow and surface tension have been exploited in clever ways to guide or template fluids into distinct regions of a device with distinct purposes including but not limited to “virtual” walls^{53,54}, burst valves^{55,56}, and patterning of viscous solutions, such as hydrogel precursors for 3D cultures^{57–60}, inside microfluidic devices. In the next section, we will discuss widely used technologies that are used to micropattern 3D cultures on chip.

1.1.6.2 Patterning strategies for on-chip integration

Integration of 3D cultures with fluidic control systems, particularly microfluidics, is often advantageous to control the microenvironment of the culture, but options for doing so are limited. While 3D cultures may be patterned off-chip and subsequently loaded into a microfluidic device, the alignment process may induce mechanical damage, particularly if there is a mismatch between the height of the microchamber and the culture. Therefore, methods for direct micropatterning of 3D cultures inside microfluidic chips have been developed, primarily by taking advantage of laminar flow and/or physical support structures (Figure 1-3). Patterns achieved through laminar flow are highly linear, producing well-controlled lanes of hydrogel. Micropillars and other physical support structures allow more flexibility by patterning via surface tension, but typically also produce linear or gently curved boundaries.⁶¹ These patterning strategies struggle to generate free-standing islands, concentric features, or two or more closely abutting cultures. In addition,

patterning largely relies on pre-determined chip geometries, which means changes to the organization of the 3D culture may require time-consuming new master fabrication.

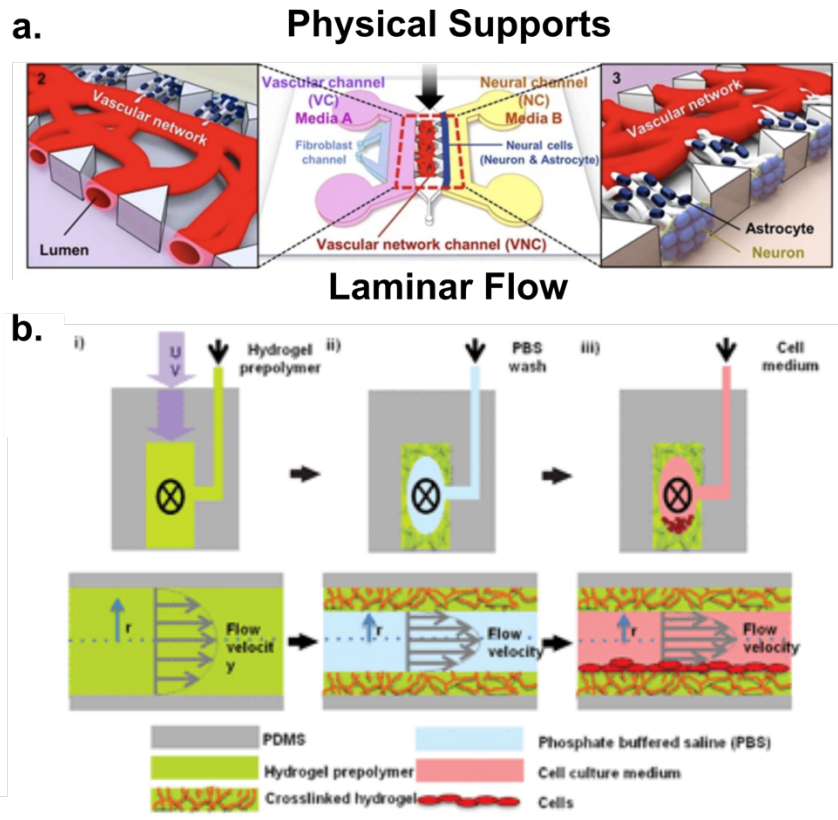


Figure 1-3 On-chip patterning strategies. a) Example of a patterned culture using physical supports, in the means of micropillars. Reproduced from [61] with permission from the Royal Society of Chemistry. b) Example of patterned channels via coating taking advantage of laminar flow parabolic profile. Reproduced from [58] with permission from the Royal Society of Chemistry.

In-situ photolithography overcomes these limitations, and has been used to coat microfluidic channels,⁵⁸ create monolayers of hydrogel onto which cells are later seeded⁶², and to create free-floating microstructures for collection downstream.⁶³ Recently, on-chip photolithography was used to create a cell-laden micropillar array.⁶⁴ However,

photopatterning of more complex, non-linear, self-standing 3D cultures within a microfluidic chip remains a significant challenge.

1.1.6.3 Background on photoreactive hydrogels

Patterning cultures on-chip via photolithography with the goal of recapitulating complex organ architecture requires crosslinking cell-laden hydrogels without cytotoxicity, while still achieving biomimetic mechanical properties and stability under fluid flow. These requirements impose constraints on the choice of biomaterial and extent of photoexposure. Indeed, the risk of phototoxicity has largely limited the use of photopatterning to hydrogels without cells or with hardy cell lines.^{32,42-44,65-67} To understand the considerations one must take with each photochemistry will be discussed in detail below.

Radical mediated photopolymerization of biomaterials to create 3D hydrogels is a well-established technique, used primarily to create *in vitro* systems in which cells can be seeded on top of or embedded within a matrix to study their behavior. For photopolymerization to start, regardless of chemistry, a photoinitiator must be present to catalyze the reaction. In the case of type I (cleavage-type) photoinitiators, after light exposure, the molecule will absorb photons from the light source and cleave into two substituent radicals⁶⁸ that set polymerization in motion (Figure 1-4). When considering the generation of cell-laden hydrogels care must be taken when selecting a suitable photoinitiator; parameters such as high solubility in aqueous solution and sufficient molar absorptivity at biocompatible wavelengths are critical. In the field of photopolymerizable hydrogels Irgacure 2959 has been long used as the photoinitiator of choice, but its low aqueous solubility (< 2 wt%)⁶⁹ and near zero absorptions beyond 370 nm⁷⁰ makes it less than optimal for cell encapsulation of sensitive cells. As an alternative, lithium acylphosphinate (LAP), another type I photoinitiator, provides a wider absorbance spectrum

with moderate molar absorptivity at wavelengths > 400 nm ($25 \text{ M}^{-1} \text{ cm}^{-1}$) making it compatible for excitation under visible light and has been shown to be less damaging to cells.⁷¹ For this reason and based on published data showing improved biocompatibility when using LAP over Irgacure, we selected LAP as our initiator of choice.

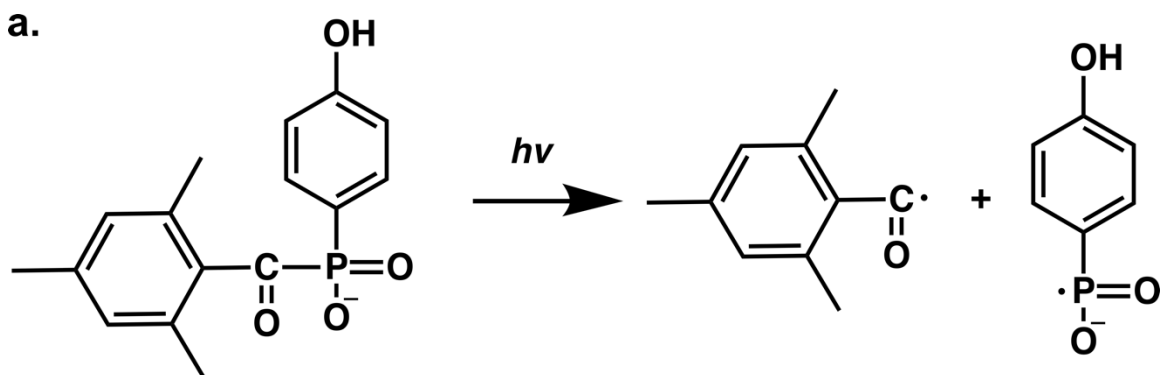


Figure 1-4 Cleavage of lithium acyl-phosphinate (LAP) into two primary radicals upon light exposure.

One of the gold-standard biomaterials in the field of photopolymerizable hydrogels is methacryloyl-functionalized gelatin; a gelatin backbone that in the presence of methacrylic anhydride gets adorned with photoreactive groups primarily at the lysine and hydroxylysine residues (Figure 1-5a). The degree of functionalization can, in theory, be controlled by the amount of methacrylic anhydride that gets fed into the reaction and as the functionalization approaches completion, other residues can begin to be substituted as well.⁷² The resulting methacryloyl groups are self-reacting which means that, in the presence of a photoinitiator, photopolymerization two groups on either the same or distinct gelatin strands will covalently react with each other forming a crosslinked network. The specifics of the reaction are illustrated below (Figure 1-5b). In short, a free radical R, (derived from a cleaved photoinitiator) will abstract a proton from a carbon in the methacryloyl moiety through which the reaction will propagate. The reaction follows chain-

growth polymerization scheme which can be inhibited by oxygen, due to its rapid radical scavenging that results in reactive oxygen species,⁷³ thus under ambient conditions the reaction can take several minutes to complete.

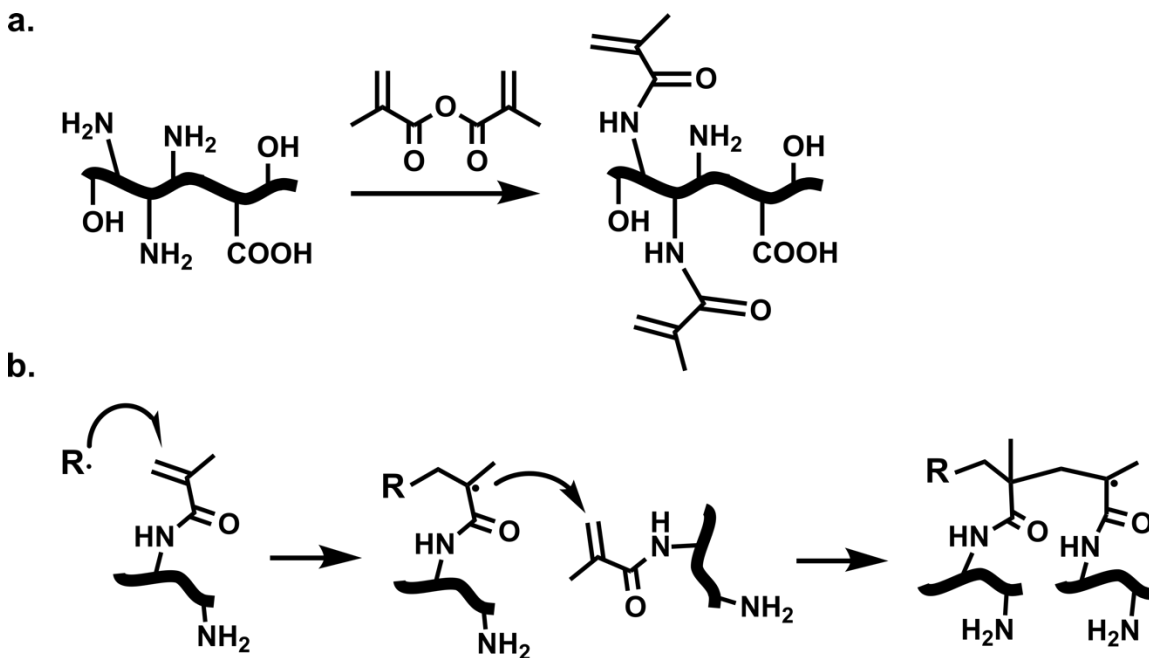


Figure 1-5 Gelatin methacryloyl synthesis and polymerization. (a) Primary amines in a gelatin strand (bold black curve) react with methacrylic anhydride to produce a photoreactive gelatin-derivative containing methacryloyl groups. (b) Schematic of photocrosslinking of GelMA in the presence of a radical (R). Two GelMA strands become covalently bound, forming a hydrogel network. A carbon radical center shown where the reaction would progress.

This delayed polymerization renders GelMA a difficult material for encapsulation of sensitive cell types, where in order to increase biocompatibility is preferable to have quick light exposures that yield stable hydrogels. Nevertheless, GelMA has been used extensively for encapsulation of many cell types both through photolithography and other manufacturing techniques like 3D printing.^{74,73,75}

An alternative for methacryloyl-functionalization of photopolymerizable gelatin derivatives is the inclusion of norbornene (GelNB) or thiol (GelSH) groups to access thiol-ene “click” polymerization.^{76,77} In contrast to acrylate-based polymerization, the functional groups are not homo-polymerizable which means a third component must be included, but inclusion of a complementary linker as part of the hydrogel precursor is straightforward and can provide even more control over reaction kinetics based on its size and concentration.⁷⁸ The thiol-ene chemistry combination follows step-growth polymerization; the general scheme of the radical-polymerization is shown in (Figure 1-6a). A radical (R), derived from the photoinitiator, will abstract a proton from sulfhydryl groups in the GelSH to form thiyl radicals that react with strained vinyl bonds in the norbornene moiety on the linker. This reaction creates thiol-ether bond and a carbon-centered radical capable of generating another thiyl radical. The alternate thiol-norbornene coupling and thiyl radical generation proceeds until the limited moiety (thiol or norbornene) is depleted.⁷⁷ This allows precise control over the mechanical properties of the hydrogels, as well as sites available for post-modification based on the thiol:norbornene ratio present in the reaction. One of the biggest advantages of thiol-ene polymerization over acrylate polymerization is its insensitivity to oxygen quenching. The mechanism shown below (Figure 1-6b) relies on the hydrogen abstraction of a thiol hydrogen by peroxy radicals that are formed by the reaction of carbon-centered propagation radicals with molecular oxygen. In this case, the thiyl radicals formed will feed into carbon-carbon double bonds to continue the main propagation steps.⁷⁹ This process results in more efficient reaction progression, with gel points as low as 12 seconds.⁷⁸ As a result of these properties different groups have compared the performance of thiol-ene based biomaterials to the well-established, but often toxic, methacryloyl-based and have confirmed increased biocompatibility with epithelial cell lines and human mesenchymal stem cells.^{76,78}

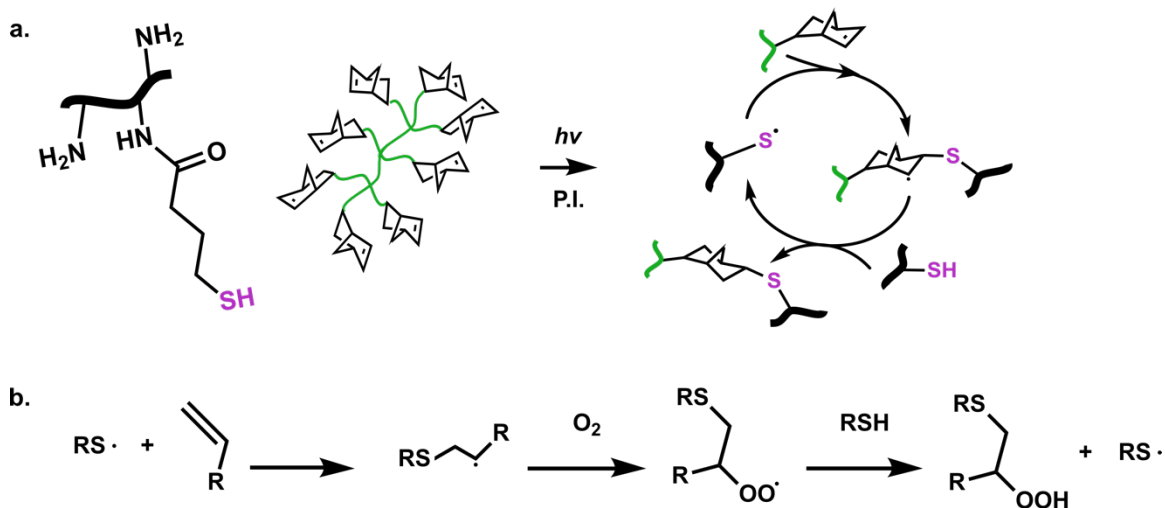


Figure 1-6 Thiol-ene step growth polymerization (a) Reaction scheme between thiol-functionalized gelatin and an 8-arm norbornene-terminated linker. In the presence of light and a photoinitiator (P.I.) radical mediate step growth takes place. (b) Mechanism for oxygen scavenging shows that peroxy radicals will abstract a proton from a neighboring thiol group which will further react with other double carbon bonds, propagating the polymerization.

1.1.7 Lymph node as a case study of on-chip micropatterning

The lymph node (LN) is the secondary lymphoid organ in which adaptive immunity begins. Due to the many entry sites for pathogens, humans have between 500 to 600 LNs distributed throughout the body which offer localized immune responses.⁸⁰ The proximity of LN's to the blood and lymphatic systems allows for efficient antigen sorting and enables entry of immune cells from neighboring tissues.^{81,80} The LN acts as an intermediary by guiding antigens and antigen presenting cells (APC's) towards rare antigen-specific T cells, increasing the possibility of encountering each other and triggering an efficient

adaptive immune response. The LN is also the site that hosts immune responses to events such as infection, vaccination and autoimmunity.

The LN is a highly organized organ in which substructures composed of distinct cell types can be found (Figure 1-7). In a simplified manner, one can think of the LN as having three main regions: the sub-capsular sinus, the B cell follicles, and the deep paracortex, which include many cell types including both T cells and APC's.⁸² Stromal cells mediate cell migration in the LN via release of chemokines such as CCL21, which bind to receptors found on both B and T lymphocytes and facilitate the entry of naive lymphocytes into the paracortex. The entire architecture of the LN is supported by the reticular network, an intricate mesh-like structure composed of reticular fibers, fibrous ECM bundles, and fibroblastic reticular cells (FRCs). The characteristic network made by FRCs seems optimal for providing mechanical strength to the tissue as well as making spaces for immune cells to migrate through. In addition, it may function as a physical barrier for the compartmentalization of immune cells to prohibit their disordered interactions or overgrowth-growth.^{83,84}

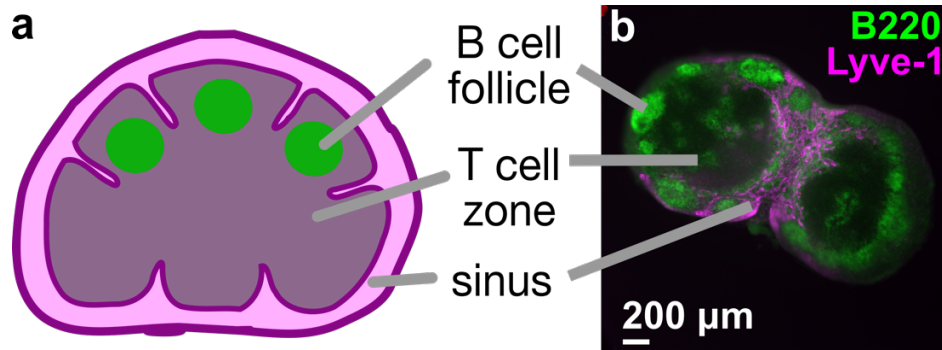


Figure 1-7 Key structural features in thick lymph node slices (a) Schematic (b) Female C57Bl/6J mouse LN slice labeled with anti-B220 (FITC, green) and anti-Lyve-1 (eFluor660, purple) revealed key structural features of the lymph node including B cell follicles, lymphatic sinus, and T cell rich zone (B220 dim).⁸ Adapted with permission from *ACS Pharmacol. Transl. Sci.* 2021, 4, 1, 128-142. Copyright 2021 American Chemical Society.

Fluid flow is a critical component in both healthy and diseased LN's. In short, one can think of the LN as having 3 avenues through which different types of fluid come in: the lymphatic vessels, the high endothelial venules, and vasculature.⁸⁵ For simplicity, we will focus on the role of lymph fluid flow in the LN. However, it is important to keep in mind that the roles of fluid flow observed in other organs, as described in prior sections, such as nutrient, gas and waste exchange still apply. The lymphatic vessels carry lymph fluid from the peripheral tissues towards the LN, bringing with it cellular debris, metabolic intermediates, immune cells, and other substances.⁸⁵ The first role of this fluid is passive antigen drainage; since lymphocyte activation is dependent on antigen exposure, lymph flow is required for the delivery of pathogens to the LN where an immune response can jumpstart. The second role is to assist in cytokine remote signaling; cytokines and chemokines released at a site of infection can be carried via the lymph to the draining LN, contributing to the quality and quantity of immune response. The dynamics of lymph flow

within the LN have significant impact on the ability of the immune system to efficiently respond to peripheral challenge.⁸⁵

1.1.8 Existing models of the lymph node

Based on the role that the LN has within the body, as a catalyst of adaptive immunity, it is vital that an organ-on-chip model of this organ be developed. One of the first models attempting to replicate specific organ-level function of the human lymph node (HuALN) was developed by Giese *et al* in the form of two bioreactors: HIRIS™ III and IG-device.⁸⁶ The first bioreactor was made of polysulfone and contained two culture compartments separated by oxygenating membranes that supported a 3D culture of immobilized cells. The second bioreactor was made up of 12 individual culture compartments, which allowed multiplexing for drug and drug dose testing in one platform. All 12 culture compartments were equipped with handy venting ports, sample collection vials, gas-permeable foil that allowed oxygenation of the culture which were all joined on one common base plate that had dimensions of a standard well-plate. Both platforms were used to test the effect of vaccination with Havrix™, a Hep A vaccine, *in vitro*. The bioreactors were loaded with a mixture of peripheral blood mononuclear cells including T cells, B cells and monocytes, as well as the mature DC and inoculation mixture and were cultured from 14 - 30 days. The platform allowed for daily sampling of culture supernatant to track cytokine secretion profiles. Additionally, through 2-photon microscopy and immunostaining, researchers confirmed organoid self-organization and plasma cell formation, as a function of activation, in both bioreactors after 7 days of culture. This was the first model to demonstrate that micro-organoid formation through self-assembly could be achieved on chip. While self-assembly of cellular components into discrete architectures is a powerful behavior and mimics what occurs *in vivo*, it may be time-

consuming to wait until this occurs and delay the experimental workflow in order to begin testing of specific responses.

On the other hand, a popular platform to study lymph node organ while retaining the native complexity found *in vivo* are lymph node slices pioneered by the Pompano laboratory. In this case, murine lymph node organs are dissected, embedded in agarose and sliced into 300 μm thick slices using a vibratome⁸ (Figure 1-8a). The live slices retain all the extracellular components, preserving the spatial organization of the organ in the absence of fixation. The slices have also been used to visualize the distribution of draining antigen after *in vivo* vaccination with rhodamine-conjugated ovalbumin (OVA) protein. This platform highlights the large heterogeneity in cellular composition between slices, reflective of the complex three-dimensional structure of this organ and the nonuniform distribution of cell types within it (Figure 1-8b). Interestingly, the authors report that variations in large-scale tissue architecture between slices from the same organ exceeded the variations between three types of skin-draining lymph nodes: the inguinal, axial, and brachial. Based on these observations, tissue slices may provide an excellent means to quantify and assess variation in population function across the tissue, whereas methods that begin with tissue homogenization lose this information. However, it may be difficult to investigate the impact on cell organization in a systematic way when the slices are highly heterogenous. Additionally, while all spatial organization is preserved, once the organ is removed from the body it loses its connections to the vasculature, which as discussed earlier are critical to the proper functioning of organs.

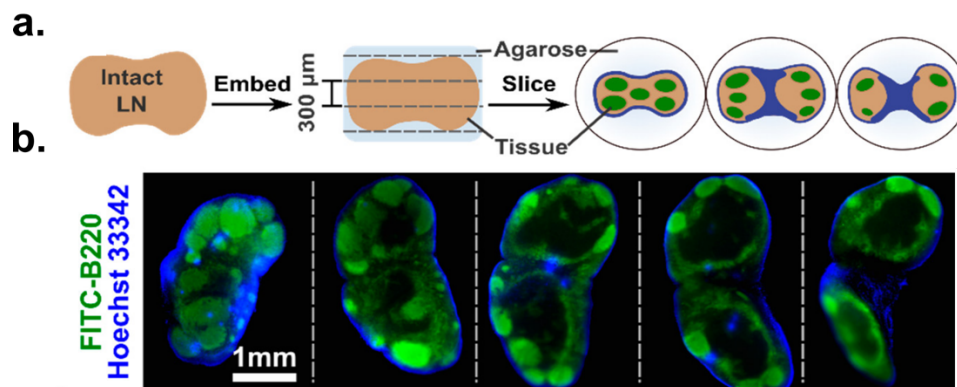


Figure 1-8 Lymph node tissue slices a) Schematic representation of slicing the complex three-dimensional lymph node into 300- μm increments, which yields slices that are heterogeneous in terms of cell population and spatial distribution. B cell follicles shown in green; sinuses in blue. b) Serial 100- μm thick slices of a fixed lymph node labeled with FITC anti-B220 (green) and Hoechst 33342 (blue) detailing the heterogeneous cell distribution in the lymph node and how it changes with depth in the tissue. Adapted with permission from *ACS Pharmacol. Transl. Sci.* 2021, 4, 1, 128-142. Copyright 2021 American Chemical Society.⁸

It is notorious that both spatial organization and fluid flow are critical aspects to the correct functioning of the LN, thus, a fully biomimetic organ-on-chip model should incorporate those aspects. The work discussed in this dissertation was inspired by the overarching goal of utilizing a “bottom-up” approach to construct a lymph node chip.

1.1.9 Research objectives and concluding remarks

The overall objective of this work was to establish a robust and user-friendly methodology to incorporate spatially organized cell-laden hydrogels inside a microfluidic device with the goal of replicating the intricate cellular organization found in organ tissues, with the LN as inspiration, while retaining the ability to incorporate fluid flow. In short, I

propose a method to access total freedom to accommodate cellular components in any configuration in the x-y plane to recapitulate the complex tissue architecture of the lymph node (Figure 1-9).

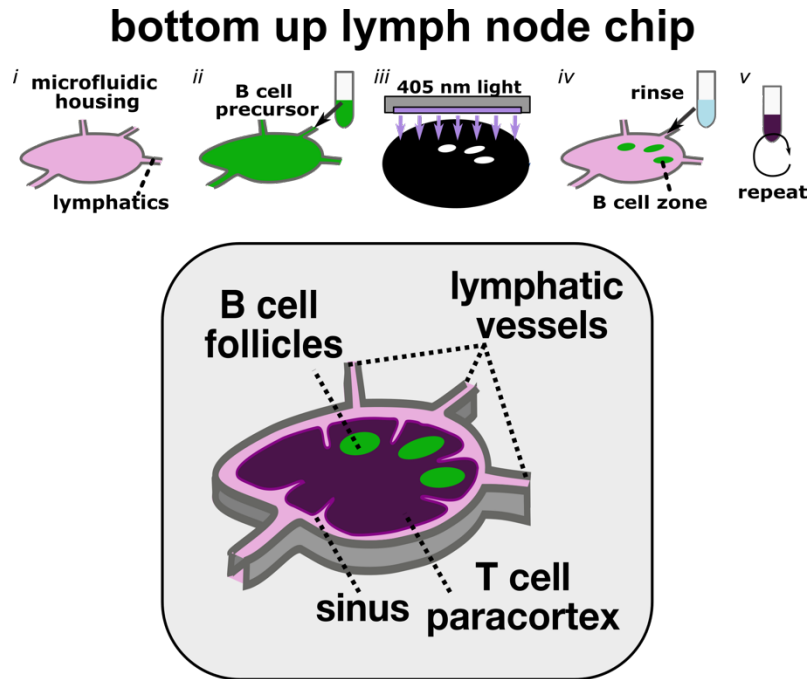


Figure 1-9 Concept schematic of “bottom-up” lymph node chip, process of photopatterning 3D cultures of specific cell types inside of a microfluidic housing to recapitulate key architectural landmarks of the LN.

To achieve this goal, we coupled photolithography with photo-crosslinkable hydrogels in a simple microfluidic housing. The integration of micropatterned 3D cultures with microfluidics in the absence of physical support or pre-determined guiding structures, grants researchers the flexibility to accommodate distinct “tissue substructures” (or varied cell populations) at will without access or expertise to microfluidic fabrication. In order to achieve these goals, in Chapter 2, we will discuss the importance of reproducible synthesis of gelatin-based biomaterials, as well as the development of methods for quality

control of these biomaterials synthesized in house by using a combination of colorimetric assays, rheology and NMR. In Chapter 3, we will discuss considerations to develop a robust on-chip photopatterning set up, including equipment considerations, reagent selection, microfluidic device design optimization and finally we will explore the applicability of different gelatin-based biomaterials that follow distinct polymerization chemistries and the impact on accuracy, resolution, stability and biocompatibility using murine and human primary cells. Finally, I will conclude Chapter 4 with a discussion on the impact that this technology can have in the field of organ-on-chip as well as recommendations for further tailoring of photo-patternable materials for enhanced interaction of lymphocytes.

1.2 References

1. Lander, A. D. How Cells Know Where They Are. *Science* **339**, 923–927 (2013).
2. Hammel, J. H., Cook, S. R., Belanger, M. C., Munson, J. M. & Pompano, R. R. Modeling Immunity In Vitro: Slices, Chips, and Engineered Tissues. *Annu. Rev. Biomed. Eng.* (2021) doi:10.1146/annurev-bioeng-082420-124920.
3. Wang, K. *et al.* Cardiac tissue slices: preparation, handling, and successful optical mapping. *Am. J. Physiol. - Heart Circ. Physiol.* **308**, H1112–H1125 (2015).
4. Olinga, P. & Schuppan, D. Precision-cut liver slices: A tool to model the liver ex vivo. *J. Hepatol.* **58**, 1252–1253 (2013).
5. De Simoni, A. & MY Yu, L. Preparation of organotypic hippocampal slice cultures: interface method. *Nat. Protoc.* **1**, 1439–1445 (2006).
6. Buskila, Y. *et al.* Extending the viability of acute brain slices. *Sci. Rep.* **4**, 5309 (2014).

7. Groff, B. D., Kinman, A. W. L., Woodroof, J. F. & Pompano, R. R. Immunofluorescence staining of live lymph node tissue slices. *J. Immunol. Methods* **464**, 119–125 (2019).
8. Belanger, M. C. *et al.* Acute Lymph Node Slices Are a Functional Model System to Study Immunity Ex Vivo. *ACS Pharmacol. Transl. Sci.* **4**, 128–142 (2021).
9. Moysidou, C.-M., Barberio, C. & Owens, R. M. Advances in Engineering Human Tissue Models. *Front. Bioeng. Biotechnol.* **8**, (2021).
10. Low, L. A. & Tagle, D. A. Tissue chips - innovative tools for drug development and disease modeling. *Lab. Chip* **17**, 3026–3036 (2017).
11. Ronaldson-Bouchard, K. & Vunjak-Novakovic, G. Organs-on-a-Chip: A Fast Track for Engineered Human Tissues in Drug Development. *Cell Stem Cell* **22**, 310–324 (2018).
12. Rossi, G., Manfrin, A. & Lutolf, M. P. Progress and potential in organoid research. *Nat. Rev. Genet.* **19**, 671–687 (2018).
13. Xu, X., Jha, A. K., Harrington, D. A., Farach-Carson, M. C. & Jia, X. Hyaluronic Acid-Based Hydrogels: from a Natural Polysaccharide to Complex Networks. *Soft Matter* **8**, 3280–3294 (2012).
14. Levett, P. A., Hutmacher, D. W., Malda, J. & Klein, T. J. Hyaluronic Acid Enhances the Mechanical Properties of Tissue-Engineered Cartilage Constructs. *PLoS ONE* **9**, e113216 (2014).
15. Unal, D. B., Caliarì, S. R. & Lampe, K. J. 3D Hyaluronic Acid Hydrogels for Modeling Oligodendrocyte Progenitor Cell Behavior as a Function of Matrix Stiffness. *Biomacromolecules* **21**, 4962–4971 (2020).
16. Janmey, P. A., Winer, J. P. & Weisel, J. W. Fibrin gels and their clinical and bioengineering applications. *J. R. Soc. Interface* **6**, 1–10 (2009).

17. Pradhan, S., Hassani, I., Seeto, W. J. & Lipke, E. A. PEG-fibrinogen hydrogels for three-dimensional breast cancer cell culture. *J. Biomed. Mater. Res. A* **105**, 236–252 (2017).
18. Silva, A. K. A., Richard, C., Bessodes, M., Scherman, D. & Merten, O.-W. Growth Factor Delivery Approaches in Hydrogels. *Biomacromolecules* **10**, 9–18 (2009).
19. Wylie, R. G. *et al.* Spatially controlled simultaneous patterning of multiple growth factors in three-dimensional hydrogels. *Nat. Mater.* **10**, 799–806 (2011).
20. Miller, A. J. *et al.* Generation of lung organoids from human pluripotent stem cells in vitro. *Nat. Protoc.* **14**, 518–540 (2019).
21. Purwada, A. *et al.* Ex vivo engineered immune organoids for controlled germinal center reactions. *Biomaterials* **63**, 24–34 (2015).
22. Yamamoto, K. *et al.* Fluid shear stress induces differentiation of Flk-1-positive embryonic stem cells into vascular endothelial cells in vitro. *Am. J. Physiol.-Heart Circ. Physiol.* **288**, H1915–H1924 (2005).
23. Riehl, B. D., Donahue, H. J. & Lim, J. Y. Chapter 17 - Fluid Flow Control of Stem Cells With Investigation of Mechanotransduction Pathways. in *Biology and Engineering of Stem Cell Niches* (eds. Vishwakarma, A. & Karp, J. M.) 257–272 (Academic Press, 2017). doi:10.1016/B978-0-12-802734-9.00017-2.
24. Tomei, A. A., Siegert, S., Britschgi, M. R., Luther, S. A. & Swartz, M. A. Fluid flow regulates stromal cell organization and CCL21 expression in a tissue-engineered lymph node microenvironment. *J. Immunol. Baltim. Md 1950* **183**, 4273–4283 (2009).
25. Fathi, P., Holland, G., Pan, D. & Esch, M. B. Lymphatic Vessel on a Chip with Capability for Exposure to Cyclic Fluidic Flow. *ACS Appl. Bio Mater.* acsabm.0c00609 (2020) doi:10.1021/acsabm.0c00609.

26. Montgomery, M., Zhang, B. & Radisic, M. Cardiac Tissue Vascularization From Angiogenesis to Microfluidic Blood Vessels. *J. Cardiovasc. Pharmacol. Ther.* **19**, 382–393 (2014).
27. Smith, Q. & Gerecht, S. Going with the flow: microfluidic platforms in vascular tissue engineering. *Curr. Opin. Chem. Eng.* **3**, 42–50 (2014).
28. Huh, D. *et al.* Reconstituting Organ-Level Lung Functions on a Chip. *Science* **328**, 1662–1668 (2010).
29. Wilmer, M. J. *et al.* Kidney-on-a-Chip Technology for Drug-Induced Nephrotoxicity Screening. *Trends Biotechnol.* **34**, 156–170 (2016).
30. Park, T.-E. *et al.* Hypoxia-enhanced Blood-Brain Barrier Chip recapitulates human barrier function and shuttling of drugs and antibodies. *Nat. Commun.* **10**, 2621 (2019).
31. Ahn, S. I. *et al.* Microengineered human blood–brain barrier platform for understanding nanoparticle transport mechanisms. *Nat. Commun.* **11**, 175 (2020).
32. Skardal, A., Devarasetty, M., Soker, S. & Hall, A. R. In situ patterned micro 3D liver constructs for parallel toxicology testing in a fluidic device. *Biofabrication* **7**, 031001 (2015).
33. Belanger, M. C., Anbaei, P., Dunn, A. F., Kinman, A. W. L. & Pompano, R. R. Spatially Resolved Analytical Chemistry in Intact, Living Tissues. *Anal. Chem.* **92**, 15255–15262 (2020).
34. The extracellular matrix at a glance | Journal of Cell Science | The Company of Biologists. <https://journals-biologists-com.proxy01.its.virginia.edu/jcs/article/123/24/4195/31378/The-extracellular-matrix-at-a-glance>.

35. Strand, D. W., Franco, O. E., Basanta, D., Anderson, A. R. A. & Hayward, S. W. Perspectives on Tissue Interactions in Development and Disease. *Curr. Mol. Med.* **10**, 95–112 (2010).
36. Engle, J. E. Clinical Physiology of Acid-Base and Electrolyte Disorders. *JAMA* **263**, 2375–2376 (1990).
37. Pittman, R. N. *The Circulatory System and Oxygen Transport. Regulation of Tissue Oxygenation* (Morgan & Claypool Life Sciences, 2011).
38. Offenhäusser, A. *et al.* Microcontact printing of proteins for neuronal cell guidance. *Soft Matter* **3**, 290–298 (2007).
39. Qin, D., Xia, Y. & Whitesides, G. M. Soft lithography for micro- and nanoscale patterning. *Nat. Protoc.* **5**, 491–502 (2010).
40. Miri, A. K. *et al.* Bioprinters for organs-on-chips. *Biofabrication* **11**, 042002 (2019).
41. Miri, A. K. *et al.* Microfluidics-Enabled Multimaterial Maskless Stereolithographic Bioprinting. *Adv. Mater.* **30**, 1800242 (2018).
42. Sato, K. *et al.* Patterned Co-culture of Live Cells on a Microchip by Photocrosslinking with Benzophenone. *Anal. Sci.* **32**, 113–116 (2016).
43. Zhu, M. *et al.* Gelatin methacryloyl and its hydrogels with an exceptional degree of controllability and batch-to-batch consistency. *Sci. Rep.* **9**, 6863 (2019).
44. Takeuchi, M. *et al.* On-Chip Fabrication of Cell-Attached Microstructures using Photo-Cross-Linkable Biodegradable Hydrogel. *J. Funct. Biomater.* **11**, (2020).
45. Lampi, M. C., Guvendiren, M., Burdick, J. A. & Reinhart-King, C. A. Photopatterned Hydrogels to Investigate the Endothelial Cell Response to Matrix Stiffness Heterogeneity. *ACS Biomater. Sci. Eng.* **3**, 3007–3016 (2017).
46. Gurkan, U. A. *et al.* Simple Precision Creation of Digitally Specified, Spatially Heterogeneous, Engineered Tissue Architectures. *Adv. Mater.* **25**, 1192–1198 (2013).

47. Peela, N. *et al.* A three dimensional micropatterned tumor model for breast cancer cell migration studies. *Biomaterials* **81**, 72–83 (2016).
48. Whitesides, G. M. The origins and the future of microfluidics. *Nature* **442**, 368–373 (2006).
49. Terry, S. C., Jerman, J. H. & Angell, J. B. A gas chromatographic air analyzer fabricated on a silicon wafer. *IEEE Trans. Electron Devices* **26**, 1880–1886 (1979).
50. Duffy, D. C., McDonald, J. C., Schueller, O. J. A. & Whitesides, G. M. Rapid Prototyping of Microfluidic Systems in Poly(dimethylsiloxane). *Anal. Chem.* **70**, 4974–4984 (1998).
51. Beebe, D. J., Mensing, G. A. & Walker, G. M. Physics and Applications of Microfluidics in Biology. *Annu. Rev. Biomed. Eng.* **4**, 261–286 (2002).
52. Vowell, S. *Microfluidics: The Effects of Surface Tension*. (2009).
53. Barlow, J. Virtual walls for microfluidics. *Nat. Biotechnol.* **19**, 319–319 (2001).
54. Lai, H.-H., Xu, W. & Allbritton, N. L. Use of a virtual wall valve in polydimethylsiloxane microfluidic devices for bioanalytical applications. *Biomicrofluidics* **5**, 024105 (2011).
55. Riegger, L. *et al.* Dye-based coatings for hydrophobic valves and their application to polymer labs-on-a-chip. *J. Micromechanics Microengineering* **20**, 045021 (2010).
56. Silva, G., Leal, N. & Semiao, V. Critical pressure for capillary valves in a Lab-on-a-Disk: CFD and flow visualization. *Comput. Struct.* **88**, 1300–1309 (2010).
57. Therriault, D., White, S. R. & Lewis, J. A. Chaotic mixing in three-dimensional microvascular networks fabricated by direct-write assembly. *Nat. Mater.* **2**, 265–271 (2003).
58. Annabi, N. *et al.* Hydrogel-coated microfluidic channels for cardiomyocyte culture. *Lab. Chip* **13**, 3569–3577 (2013).

59. Rosa, P. M., Gopalakrishnan, N., Ibrahim, H., Haug, M. & Halaas, Ø. The intercell dynamics of T cells and dendritic cells in a lymph node-on-a-chip flow device. *Lab. Chip* **16**, 3728–3740 (2016).
60. Kim, H. J., Du, W. & Ismagilov, R. F. Complex Function by Design Using Spatially Pre-Structured Synthetic Microbial Communities: Degradation of Pentachlorophenol in the Presence of Hg(II). *Integr. Biol. Quant. Biosci. Nano Macro* **3**, 126–133 (2011).
61. Bang, S. *et al.* A Low Permeability Microfluidic Blood-Brain Barrier Platform with Direct Contact between Perfusable Vascular Network and Astrocytes. *Sci. Rep.* **7**, 8083 (2017).
62. Ebrahimi, M. *et al.* Enhanced skeletal muscle formation on microfluidic spun gelatin methacryloyl (GelMA) fibres using surface patterning and agrin treatment. *J. Tissue Eng. Regen. Med.* **12**, 2151–2163 (2018).
63. Panda, P. *et al.* Stop-Flow Lithography to Generate Cell-Laden Microgel Particles. *Lab. Chip* **8**, 1056–1061 (2008).
64. Hu, X. *et al.* On-chip hydrogel arrays individually encapsulating acoustic formed multicellular aggregates for high throughput drug testing. *Lab. Chip* **20**, 2228–2236 (2020).
65. Rajan, S. A. P., Skardal, A. & Hall, A. R. Multi-Domain Photopatterned 3D Tumor Constructs in a Micro-Physiological System for Analysis, Quantification, and Isolation of Infiltrating Cells. *Adv. Biosyst.* **4**, e1900273 (2020).
66. Aung, A., Kumar, V., Theprungsirikul, J., Davey, S. K. & Varghese, S. An Engineered Tumor-on-a-Chip Device with Breast Cancer–Immune Cell Interactions for Assessing T-cell Recruitment. *Cancer Res.* **80**, 263–275 (2020).
67. LeValley, P. J. *et al.* Fabrication of Functional Biomaterial Microstructures by in Situ Photopolymerization and Photodegradation. *ACS Biomater. Sci. Eng.* **4**, 3078–3087 (2018).

68. Majima, T., Schnabel, W. & Weber, W. Phenyl-2,4,6-trimethylbenzoylphosphinates as water-soluble photoinitiators. Generation and reactivity of $\text{O}\ddot{\text{P}}(\text{C}_6\text{H}_5)(\text{O}^-)$ radical anions. *Makromol. Chem.* **192**, 2307–2315 (1991).
69. Fouassier, J.-P., Burr, D. & Wieder, F. Water-soluble photoinitiators: Primary processes in hydroxy alkyl phenyl ketones. *J. Polym. Sci. Part Polym. Chem.* **29**, 1319–1327 (1991).
70. Bryant, S. J., Nuttelman, C. R. & Anseth, K. S. Cytocompatibility of UV and visible light photoinitiating systems on cultured NIH/3T3 fibroblasts in vitro. *J. Biomater. Sci. Polym. Ed.* **11**, 439–457 (2000).
71. Fairbanks, B. D., Schwartz, M. P., Bowman, C. N. & Anseth, K. S. Photoinitiated polymerization of PEG-diacrylate with lithium phenyl-2,4,6-trimethylbenzoylphosphinate: polymerization rate and cytocompatibility. *Biomaterials* **30**, 6702–6707 (2009).
72. Claaßen, C. *et al.* Quantification of Substitution of Gelatin Methacryloyl: Best Practice and Current Pitfalls. *Biomacromolecules* **19**, 42–52 (2018).
73. Lim, K. S. *et al.* New Visible-Light Photoinitiating System for Improved Print Fidelity in Gelatin-Based Bioinks. *ACS Biomater. Sci. Eng.* **2**, 1752–1762 (2016).
74. Yue, K. *et al.* Synthesis, properties, and biomedical applications of gelatin methacryloyl (GelMA) hydrogels. *Biomaterials* **73**, 254–271 (2015).
75. Van Hoorick, J. *et al.* (Photo-)crosslinkable gelatin derivatives for biofabrication applications. *Acta Biomater.* **97**, 46–73 (2019).
76. McCall, J. D. & Anseth, K. S. Thiol–Ene Photopolymerizations Provide a Facile Method To Encapsulate Proteins and Maintain Their Bioactivity. *Biomacromolecules* **13**, 2410–2417 (2012).
77. Lin, C.-C., Ki, C. S. & Shih, H. Thiol-norbornene photo-click hydrogels for tissue engineering applications. *J. Appl. Polym. Sci.* **132**, (2015).

78. Muñoz, Z., Shih, H. & Lin, C.-C. Gelatin hydrogels formed by orthogonal thiol–norbornene photochemistry for cell encapsulation. *Biomater. Sci.* **2**, 1063–1072 (2014).
79. Hoyle, C. E., Lee, T. Y. & Roper, T. Thiol–enes: Chemistry of the past with promise for the future. *J. Polym. Sci. Part Polym. Chem.* **42**, 5301–5338 (2004).
80. Grant, S. M., Lou, M., Yao, L., Germain, R. N. & Radtke, A. J. The lymph node at a glance – how spatial organization optimizes the immune response. *J. Cell Sci.* **133**, jcs241828 (2020).
81. Bajénoff, M. *et al.* Stromal Cell Networks Regulate Lymphocyte Entry, Migration, and Territoriality in Lymph Nodes. *Immunity* **25**, 989–1001 (2006).
82. Worbs, T. & Förster, R. T Cell Migration Dynamics Within Lymph Nodes During Steady State: An Overview of Extracellular and Intracellular Factors Influencing the Basal Intranodal T Cell Motility. in *Visualizing Immunity* (eds. Dustin, M. & McGavern, D.) 71–105 (Springer, 2009). doi:10.1007/978-3-540-93864-4_4.
83. Katakai, T., Hara, T., Sugai, M., Gonda, H. & Shimizu, A. Lymph Node Fibroblastic Reticular Cells Construct the Stromal Reticulum via Contact with Lymphocytes. *J. Exp. Med.* **200**, 783–795 (2004).
84. Novkovic, M. *et al.* Topological Small-World Organization of the Fibroblastic Reticular Cell Network Determines Lymph Node Functionality. *PLOS Biol.* **14**, e1002515 (2016).
85. Jafarnejad, M., Zawieja, D. C., Brook, B. S., Nibbs, R. J. B. & Moore, J. E. A Novel Computational Model Predicts Key Regulators of Chemokine Gradient Formation in Lymph Nodes and Site-Specific Roles for CCL19 and ACKR4. *J. Immunol.* **199**, 2291–2304 (2017).
86. Giese, C. *et al.* Immunological substance testing on human lymphatic micro-organoids in vitro. *J. Biotechnol.* **148**, 38–45 (2010).

2 Hydrogel Reproducibility

Some text and figures are adapted from: Zatorski, J.M., Montalbino, A.N., Ortiz-Cárdenas, J.E. *et al.* Quantification of fractional and absolute functionalization of gelatin hydrogels by optimized ninhydrin assay and ^1H NMR. *Anal Bioanal Chem* **412**, 6211–6220 (2020)

2.1 Abstract

3D cell culture in protein-based hydrogels often begins with chemical functionalization of proteins with cross-linking agents such as methacryloyl or norbornene. An important and variable characteristic of these materials is the degree of functionalization (DoF), which controls the reactivity of the protein for cross-linking and therefore impacts the mechanical properties and stability of the hydrogel. A thorough assessment of DoF is essential to understand the biomaterial and ^1H NMR has emerged as the most accurate technique for quantifying absolute DoF of chemically modified proteins, but colorimetric techniques, such as the ninhydrin assay, still dominate in actual use and may be more useful for quantifying fractional or percent DoF. Furthermore, important factors to consider when utilizing functionalized biomaterials are polymerization kinetics, as well as the resulting mechanical properties of the hydrogel. In this chapter, we implemented an optimized colorimetric assay for DoF of common gelatin-based biomaterials in tandem with ^1H NMR and rheology measurements to assess hydrogel reproducibility by characterizing their chemical and mechanical properties. We show that rheology measurements are the most convenient way to scan the correct set of photo-exposure to achieve functional

biomaterials. These methods will be valuable for quality control analysis of protein-based hydrogels and 3D cell culture biomaterials.

2.2 Introduction

Collagen and gelatin (denatured collagen) are one of the most commonly used materials in the field of 3D cultures and tissue engineering because they are components found in abundance throughout the body's native tissues,¹ thus are understood to be biocompatible. Naturally-derived biomaterials like collagen or gelatin, provide advantages for cell encapsulation due to the presence of arginine-glycine-aspartic acid (RGD) cell binding motifs in the backbone which promote integrin-mediated cell migration.² Additionally, these biomaterials can be enzymatically degradable by metalloproteases (MMP's) which allow cells to remodel the matrix and spread, as needed.³ However, hydrogels created solely by collagen or gelatin are often mechanically unstable and batch-to-batch variability can arise depending on the animal source (bovine, rat, etc) as well as the type of hydrolytic degradation (either acidic or basic) used to obtain gelatin.⁴ As a result, bioengineers have come up with strategies to make these naturally-derived materials, in particular gelatin, more controllable.

One strategy to increase control and reproducibility of gelatin is the incorporation of photo-reactive motifs (such as methacryloyl, GelMA, or norbornene, GelNB) in the free amines or carboxylic acid terminus of amino-acids in the gelatin backbone (Figure 2-1 a,b). This process, referred to as "functionalization," indicates the total amount of groups that have been exchanged by photoreactive functional groups. The total degree of functionalization (DOF) can be modulated to alter the final biomechanical properties of the hydrogels. For example, it has been shown that a macromer with higher degree of functionalization leads to overall stiffer hydrogels when exposed under the same

conditions.⁵ Functionalization of a naturally-derived macromer like gelatin, coupled with an appropriate photoinitiator allows for generation of photocurable hydrogels that are stable under physiological conditions. These hydrogel chemistries are rapidly gaining popularity, with recent studies focusing on improved processability and larger batch sizes.^{6,7} As interest grows in scaled-up production and novel chemical modifications of gelatin, so does the need for reproducible and simple assays for quality control and prototyping.⁸

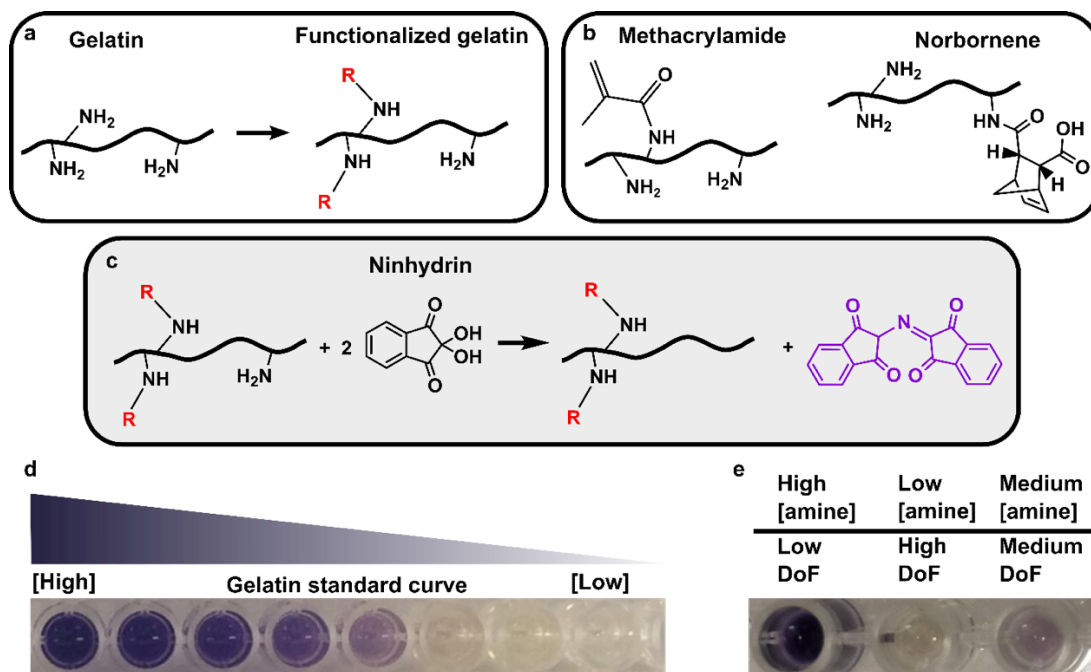


Figure 2-1 Detecting protein functionalization by loss of free amines via the colorimetric ninhydrin assay. (a) Chemical functionalization of a protein by anhydrides or succinimidyl esters occurs primarily at free amines, with minor reactivity towards free hydroxyl and thiol groups (not shown). (b) Reaction products of amine sidechains with methacryloyl or norbornene groups. (c) In the ninhydrin assay, ninhydrin reacts with free primary amines to generate Ruhemann's Purple, a purple-colored soluble product. (d) The optimized assay with a protein-based standard curve yielded clear solutions, free of precipitation, and a visible color change that corresponded to free amine content in the solution. (e) Functionalized gelatin samples (here, GelMA) produced color changes that inversely correlate with their respective DoF values. Reprinted by permission from Springer, *Analytical and Bioanalytical Chemistry* (2020) 412:6211–6220.¹⁴

During functionalization of gelatin with photoreactive groups, the DOF, the quantity or fraction of functional groups exchanged, will vary as a function of both the gelatin starting material and the reaction conditions. Both the exact amino acid content and the availability of reactive functional groups can vary between batches and sources of gelatin

(Table 2-1) due to it being a natural product sourced from animal-derived collagen and extensively processed in acidic or basic conditions.

Table 2-1 Reported lysine content and amine content of bovine and porcine gelatin.

Gelatin (species, type)	Gelatin source tissue	Lysine (mmol / g gelatin)	Amines (mmol / g gelatin)	Reference
Bovine, type B	Skin	Not Reported	0.35	6
Bovine, type B	Skin	0.28	0.385	9,10
Bovine, type B	Skin	0.100 ^a	Not reported ^b	11
Porcine, type A	Skin	0.245 ^a	Not reported ^b	11
Porcine, type A	Skin	0.259	0.325 ^c	12
Porcine, type A	Not Reported	0.245 ^a	0.300 ^{a,c}	13

^a These data were reported as “residue / 1000 amino acids”. The values were converted to “mmol / g gelatin” by assuming an average amino acid molecular weight of 110 g/mole of amino acid.

^b Neither the hydroxylysine nor the total amine content was reported.

^c This value was determined by adding reported data for lysine and hydroxylysine.

Measurements for quality control of in-house synthesized biomaterials are not well-defined in the field, thus every time a new batch is produced, lengthy process of re-optimization takes place. When a laboratory is interested in incorporating photocrosslinkable hydrogels, it can be difficult to recognize the need for careful examination of DOF because most published literature will only report the photo-exposure conditions that worked for their particular hydrogel system, which are not likely to work for a different batch of modified proteins. The optimization of these photo-exposure parameters can be time-consuming, particularly if a lab does not have access to the necessary equipment. If optimizing the photo-exposure conditions empirically requires experiments in which multiple parameters have to be changed at once including, but not limited to, (1) macromer and complementary linker concentrations, (2) photoinitiator concentration (3) light intensity and (4) time of exposure.

The methods often used for these purposes are colorimetric assays like the ninhydrin assay and NMR. The ninhydrin assay is a colorimetric assay in which primary amines react with the ninhydrin molecule to generate Ruhemann's Purple (Figure 2-1c). When comparing the signal to a calibration curve, with known amounts of free amines, the assay provides a measure of the free amines that remain post-functionalization, from which a fractional DoF can be derived. The assay was originally developed for solutions of free amino acids but has been adapted to characterize biomaterials like gelatin methacryloyl given that primary amines are the primary site of functionalization under typical reaction conditions (Figure 2-1d,e).¹⁴

Alternatively, NMR can be used as a direct method to quantify DoF of functionalized proteins. ¹H-NMR offers direct quantification of the DoF, because the spectral peak(s) corresponding to the functional group can be easily identified and integrated. Furthermore, using an internal standard has allowed for precise determination of absolute DoF in units of moles of functional group (e.g. MA) per gram of protein ¹². However, unless the amine content is known, e.g. from sequencing, the fraction of amines functionalized cannot be quantified by NMR. Furthermore, despite the accuracy of NMR methods, many biomedical researchers prefer and continue to use of colorimetric DoF assays ¹⁵⁻¹⁷. Furthermore, while DOF values can give you a sense of the general reactivity of the protein during crosslinking, factors like gel time and achievable stiffnesses require additional characterization.

Shear rheometry is one of the most used techniques to define the mechanical properties of hydrogels.¹⁸⁻²⁰ This technique allows the characterization of the rheological properties of a bulk material. In particular using *in situ* rheology, a photopolymerizable material can be characterized in a rheometer-UV (or visible) light source setup while the sample is irradiated, capturing the transition from sol to gel.²¹ These measurements are

ideal to understand the interplay between kinetics of crosslinking reactions and the mechanical properties of the developing hydrogel. Results from these curves can inform how light intensity, precursor formulation, and light dose influence the dynamics of the photo-crosslinking. These effects are particularly important to understand in cases where cell encapsulation is taking place. For example, the minimum light dose required can be determined by observing when the hydrogel reaches the target storage modulus or when it reaches its plateau modulus and avoid exposing beyond the completion of the crosslinking reaction, minimizing any cytotoxic impact the process may have on cells.

In this Chapter we will discuss how the combination of these measurements can be applied to monitor quality control of hydrogels, applied them to in-house functionalized gelatin biomaterials and discuss how to ensure reproducibility of photo-patternable biomaterials.

2.3 Material/Methods

2.3.1 Reagents and solvents

Ethanol (190 proof) was obtained from Decon Labs, Inc. Phosphate-buffered saline (PBS) was prepared in house by adding 2.7 mM KCl, 13.7 mM NaCl, 10 mM Na₂HPO₄, and 1.8 mM KH₂PO₄ to 18 MΩ Millipore water. Methacrylic anhydride, carbic anhydride, 5-Norbornene-2-carboxylic acid (endo/exo mixture), *N*-hydroxysuccinimide, *N*-(3-Dimethylaminopropyl)-*N*-ethylcarbodiimide (EDC), anhydrous DMSO, ninhydrin, and Sodium trimethylsilylpropanesulfonate (DSS) were obtained from Sigma. Ninhydrin was dissolved in ethanol to the stated concentration and used within two days. DSS was used as the internal standard (δ 0.0 ppm) and D₂O (Cambridge Isotope Laboratories, Inc.) was used as the solvent in ¹H-NMR experiments. DSS was dissolved in D₂O to at 0.25 mg/mL to make the internal standard solution.

2.3.2 Commercial GelSH

Thiol-modified gelatin (GelSH; Lot: MKCJ5413) was obtained from Sigma Aldrich and used as provided. The vendor-reported absolute degree of functionalization for this material, determined by free thiol assay, was 0.223 mmol -SH / g gelatin. 8-arm PEG-NB 20 kDa (Jenkem Technologies), 4-arm PEGSH 5kDa (Jenkem Technologies), lithium phenyl-2,4,6-trimethylbenzoylphosphinate (LAP; Sigma Aldrich), and 1x phosphate buffered saline without calcium or magnesium (1x PBS; Lonza) were also used as provided.

2.3.3 Gelatin methacryloyl functionalization

Gelatin from porcine skin, Gel Strength 300, type A (Sigma-Aldrich) was used as the starting material for all reactions. Gelatin methacryloyl (GelMA) was prepared in-house as described by Loessner et al. (2016).³ The ratio of methacrylic anhydride to gelatin was 13 mmol/ g.

2.3.4 Gelatin norbornene functionalization

Gelatin norbornene (GelNB) was prepared from gelatin as described by Muñoz et al. (2014)¹⁹ with the following exceptions: The carbic anhydride (Acros Organics) was varied from 0.4 to 3.7 mM to produce GelNB samples having a range of DoFs. Additional sodium hydroxide (50% w/v) (30– 50 mL) was needed to reach and maintain the reaction at pH 8 as the concentration of carbic anhydride was increased. The resulting product was centrifuged at 3500×g for 3 min and the supernatant was dialyzed in 4 L of ultrapure water for 10 days at 40 °C with daily water changes before freezing and lyophilization.

One batch of GelNB (GelNB-NHS) was prepared using EDC/NHS conjugation chemistry as described by Van Hoorick et al. (2018).⁷ Briefly, norbornene carboxylic acid (1.5 equivalents) was dissolved in 500 mL of dry DMSO, followed by the addition of EDC

(1 equivalent) and NHS (1.25 equivalents), degassed 3 times and left to react for 24 h under N₂ conditions. The next day, 10 g of gelatin was dissolved in 150 mL of dry DMSO under N₂ and reflux conditions. Once dissolved, the 5-norbornene-2-succinimidyl ester mixture was transferred into the gelatin flask using a transfer syringe and left to react at 50 °C for 18 h. The solution was precipitated using 10× excess acetone, then filtered through a Büchner filter. The obtained solids were dried under vacuum for 20 h. The product was dissolved at 2.5% in ultrapure water by stirring overnight; pH adjusted to 7 using NaOH and dialyzed in 4 L of ultrapure water for 24 h at 40 °C before freezing and lyophilization.

2.3.5 In-situ rheology measurements

Rheological characterization was performed using a MCT302 Anton Parr Rheometer, operated in oscillatory time sweep mode with 5% strain, 1 Hz frequency, and 0.1 mm gap to assess gel polymerization rate and storage modulus. A UV-curing stage was fitted with a 20-mm parallel plate, the light source was filtered through a 400-500 nm filter, and the stage temperature was maintained at 25 °C. 30 µL of precursor solution was pipetted onto the stage. After measuring baseline shear storage modulus for 30 seconds, light exposure was initiated with constant intensity of 50 mW/cm², unless otherwise noted.

2.3.6 Ninhydrin assay

Ninhydrin assay was performed as optimized in Zatorksi et al.¹⁴ Briefly, a standard curve was created by dissolving gelatin from 0-10 mg/mL in an ethanolic ninhydrin solution as described below. Ninhydrin solution was made by dissolving at 20 mg/mL in a 1:8 v/v ratio of ethanol:PBS for a final concentration of 2.2 mg/mL ninhydrin. Functionalized-gelatin samples were dissolved in the ethanolic ninhydrin solution at 10 mg/mL. Standard samples and functionalized-gelatin samples were plated in a 96 well-plate, covered with

optical sealing tape, and incubated to react at 70 °C for 30 min. Absorbance of samples was measured at 570 nm using a plate reader. The mean absorbance for each gelatin standard was plotted to form a standard curve. For functionalized samples the fraction of amines available was determined by:

Equation 2-1

$$\text{Fraction of amines available} = \frac{\text{Apparant sample conc.}}{\text{Actual sample conc.}}$$

where the apparent concentration was obtained by comparison with the standard curve, and the nominal concentration was defined as the concentration at which the protein sample solution was prepared. The (percent) DoF was determined by

Equation 2-2

$$\text{DoF (\%)} = 100 \times \left(1 - \frac{\text{Apparent sample conc.}}{\text{Actual sample conc.}} \right)$$

2.3.7 DOF Calculations using NMR

Quantification of DoF in mmol -R / g gelatin was performed according to the method described by Classen et al.¹² Samples were prepared for ¹H-NMR by dissolving lyophilized gelatin, GelMA, or GelNB, in the internal standard solution at 20 mg/mL gelatin. This produced a known DSS to gel ratio of 0.0573 mmol DSS / g gelatin. The ¹H-NMR spectra were obtained at room temperature using a Bruker Avance III 600 MHz spectrometer at 14.1 tesla. Spectra were analyzed using Mestranova software. All spectra were phase adjusted and baseline corrected.

Total degree of norbornene functionalization (mmol NB) of the GelNB samples was assessed by integrating the single peak at 6.0 ppm for 2 protons, corresponding to two vinyl protons of norbornene, and normalizing to the DSS peak (9 protons). The GelNB-

NHS sample was assessed by integrating the four peaks appearing from 5.8 – 6.3 ppm for 4 protons, corresponding to 2 vinyl protons of endo-norbornene and 2 vinyl protons of exo-norbornene,⁷ and normalizing to the DSS peak (9 protons). This value was multiplied by the mmol DSS / g gel ratio to determine DoF in units of (mmol NB / g gelatin). For GelMA, total degree of methacryloylation (mmol MA) was assessed according to the method from Classen et al.¹² Briefly, the two peaks at 5.5 – 5.7 ppm, corresponding to a single acrylic proton of methacrylate and a single acrylic proton of methacrylamide (Fig 4a), were integrated. The sum of both peaks was integrated for 1 proton and normalized to the DSS peak (9 protons) to determine mmol MA. This value was multiplied by the (mmol DSS / g gel) ratio to determine DoF in units of (mmol MA / g gelatin). To estimate the fractional functionalization for comparison to the ninhydrin assay, (mmol -R / g gelatin) was divided by the reported density of amines on gelatin (0.300 mmol amines / g gelatin) (see Table 2-1).¹⁰

2.4 Results

2.4.1 GelMA batch-to-batch reproducibility and characterization

First, we collected three batches of GelMA that had been synthesized in-house under the same conditions with the intention to achieve the same degree of functionalization (Table 2-2). Precursors were prepared following the same formulation, 8% w/v GelMA 0.1% LAP, and *in situ* rheology was performed. All three samples exhibited differences in both the photopolymerization kinetics and resulting storage moduli (Figure 2-2). From these data, one could deduce that batches A-C had increasingly higher levels of DOF in that respective order, with batch A having the lowest DOF achieving a plateaued moduli the quickest followed by B and finally batch C. In other words, if batch A had less functional groups available to create bonds between or within gelatin strands, then it would

have lower crosslinking density which would lead to lower storage moduli. In comparison, batch C, experienced a linear increase in moduli over a larger range with its resulting storage moduli being higher than that of either batch A or B by a factor of 2.8 and 1.8, respectively. However, when inspecting the results from both the ninhydrin and NMR assays (Table 2-2) all DOF values fall along the margin of error.

Two things are worth noting while interpreting these results. First, these storage moduli are being plotted and analyzed in a linear scale. Often, these values are plotted in a logarithmic scale in which case these differences might not seem as extreme. However, experimentally we found that differences within an order of magnitude particularly for GelMA, resulted in drastic differences in stability of micropatterned constructs. This is likely a factor of the slow polymerization dynamics of the particular reaction. At the exposure times plotted (Figure 2-2) the polymerization is still in a linear regime and has yet to achieve completion. Inherently, exposure times in this regime will have high variability in resulting storage moduli which will impact the stability of patterned hydrogels. In an ideal scenario, the patterned hydrogel and the corresponding dose will be selected by ensuring that the reaction has been completed in a reasonable amount of time while still achieving the target stiffness. This is difficult to achieve with GelMA hydrogels because of the propensity to oxygen inhibition and will be discussed further in Chapter 3. Second, with respect to reproducibility and flexibility in tailoring a hydrogel's mechanical properties, based on these data these hydrogels would only be useful to access a storage moduli of $< 1\text{kPa}$, with only one batch accessing values larger than $> 0.5\text{ kPa}$, at least at this concentration.

Table 2-2 Summary for three different batches of GelMA (synthesized in-house) with DOF's determined by colorimetric assay, NMR and corresponding storage moduli (G') after 60 seconds of exposure. *means the assay was not performed, likely product ran out. + data collected and analyzed by Jonathan Zatorski.

Batch of GelMA	Date Synthesized	Feed Ratio (g MA/g gelatin)	Ninhydrin (fractional, %)+	NMR (abs) (mmol - MA/g gelatin)+	G' at 60 s exposure (Pa)	G' at 120 s exposure (Pa)
A	June 2018	1.5/2.5	36 +/- 5	0.26	190	280
B	July 2018	1.5/2.5	32 +/- 7	0.26	280	430
C	Dec 2018	1.5/2.5	44 +/- 11	*	540	780

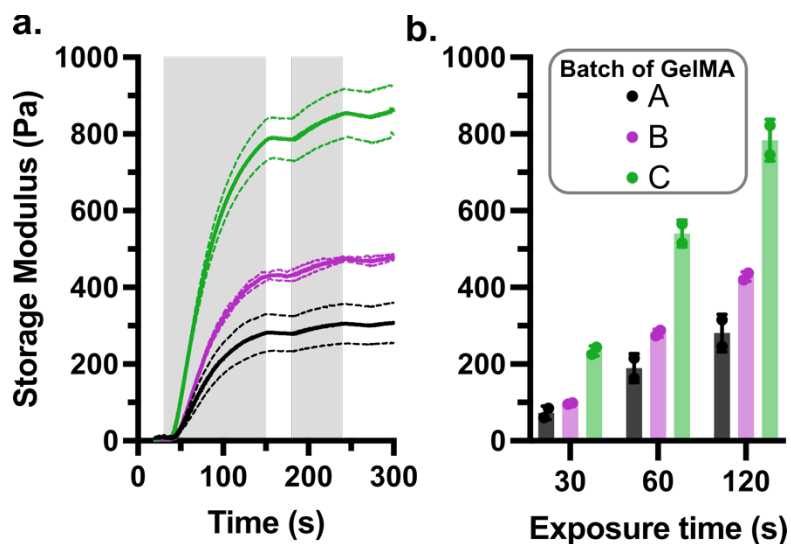


Figure 2-2 Comparison of photopolymerization of three distinct batches of in-house produced 8% w/v gelatin-methacryloyl (GelMA) with 0.1% LAP in PBS. (a) Rheometry measurements of the storage modulus of GelMA during *in situ* polymerization. Thick line shows average and dashed lines represent deviation from the mean. Grey shading indicates when light was turned on. (b) Shear storage modulus at different exposure times. Legend indicates different batch synthesis.

2.4.2 GelNB batch-to-batch reproducibility and characterization

Similar issues of highly variable hydrogel performance were obtained when synthesizing GelNB in house (Table 2-3). Below are two examples showing batches “A” and “B” of GelNB that have similar DOF’s, at least by ninhydrin assay, but have completely different photopolymerization dynamics, with batch A having slightly delayed gel point and storage moduli at 45s lower than the one from batch B by ~3x (Figure 2-3). These results are somewhat explained by the DOF quantified by NMR which showed it was ~12% higher for batch B than batch A. While this small increase in photoreactive groups would not lead to the expectation of such different polymerization kinetics, the trend of higher storage moduli as a result of higher DOF, holds true.

Table 2-3 Summary for two different batches of GeINB (synthesized in-house) with DOF's determined by colorimetric assay, NMR and corresponding storage moduli (G') after 60 seconds of exposure. *means the assay was not performed, likely product ran out. + data collected and analyzed by Jonathan Zatorski.

Batch of GeINB	Date Synthesized	Feed Ratio (g NB/g gelatin)	Ninhydrin (fractional, %)+	NMR (abs) (mmol - MA/g gelatin)+	G' at 30 s exposure (Pa)	G' at 45 s exposure (Pa)
A	Aug 2019	10/1.7	64 +/- 30%	0.191	520	640
B	Feb 2020	0.48/10	78.9+/-0.05%	0.216	1930	1990

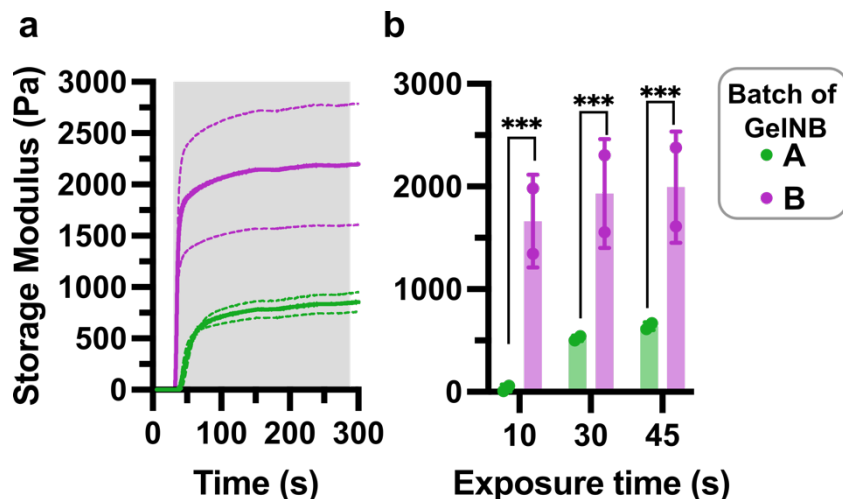


Figure 2-3 Comparison of photopolymerization of two distinct batches of in-house produced 10% w/v gelatin-norbornene (GeINB) with 15 mM SH and 0.1% LAP in PBS. (a) Rheometry measurements of the storage modulus of GeINB during *in situ* polymerization. Thick line shows average and dashed lines represent deviation from the mean. Grey shading indicates when light was turned on. (b) Shear storage modulus at different exposure times. Shared legend indicates different batch synthesis. Two-way ANOVA with Sidak's multiple comparisons; *** $p \leq 0.005$.

However, it is worth noting that batch B was synthesized following the synthesis method described by Van Hoorick,⁷ which introduces norbornene functionalities through the use of carbodiimide/*N*-hydroxysuccinimide coupling (EDC/NHS) chemistry between the carboxylic acid functionality of 5-norbornene-2-carboxylic acid. This synthesis produces both endo- and exo- isomers of the norbornene functionality. While the effect that stereochemistry may have in the polymerization has not been, to our knowledge, investigated in the literature, it may be an interesting area of study.

These results, similarly to the ones from GeIMA batches, show the difficulty of achieving consistent performance by in-house synthesized biomaterials, at least without

a highly controlled infrastructure. While there may be room to improve the reproducibility of these reactions, it is out of the scope of this work.

2.4.3 Commercially available alternatives

At the beginning of this project, the only way to access functionalized-gelatin, either MA or NB-SH, was to synthesize it in-house. As demonstrated above, in-house synthesis without a controlled environment leads to variations in DOF between batches, depending on how frequent these are used these could last as little as 3 months. As of 2021, vendors such as Sigma are selling alternatives like gelatin methacrylate with “low, medium, and high” DOF’s as well as gelatin thiol, currently available as one offering. Below is a comparison of in situ gelation of 5% GelSH (from Sigma-Aldrich) in the presence of 2.5 mM NB. While there are slight variations in the final storage modulus depending on which bottle, those variations would be acceptable for the range of storage moduli we are targeting. Our suggestion is that laboratories that are not equipped for overly controlled synthesis set-ups, find a commercial alternative that works, optimize all the photo-exposure parameters and buy the same lot product in bulk from the vendor. In our case, we were able to buy 10g of gelatin-thiol, in increments of 1g bottles.

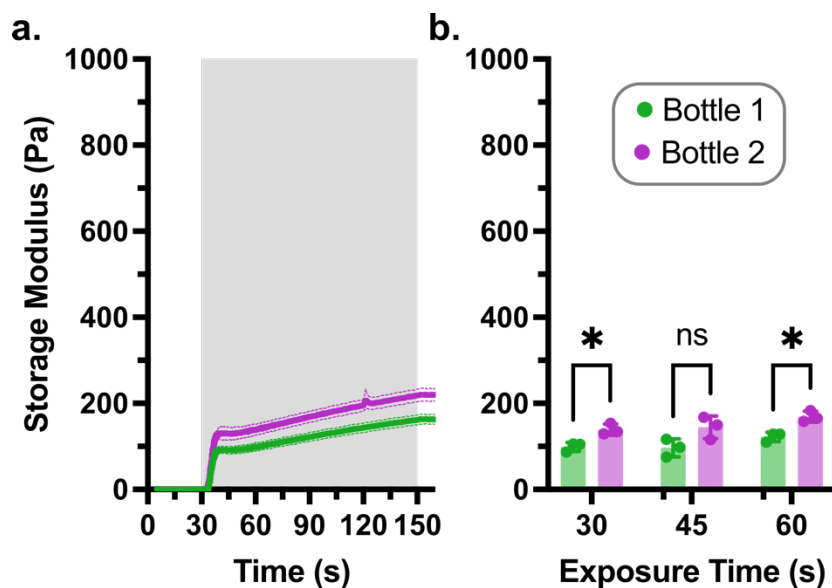


Figure 2-4 Comparison of photopolymerization of two distinct bottles of commercially available gelatin-thiol (GelSH). (a) Rheometry measurements of the storage modulus of GelSH during *in situ* polymerization under light exposure. Thick line shows average and dashed lines represent deviation from the mean. (b) Comparison of shear storage modulus at different exposure times. Grey shading indicates when light was turned on. Legend indicates different bottles same batch synthesis. n.s. $p > 0.05$, * $p \leq 0.05$, via Two-way ANOVA with Sidak's multiple comparisons.

2.5 Conclusion

Here, a set of techniques for tracking “quality control” of functionalized-gelatin biomaterials is described, establishing the emphasis for following such procedures for every new batch synthesized or bought. These techniques include assessment of DOF by ^1H NMR and ninhydrin assay and assessment of polymerization kinetics through shear rheology. Additionally, we highlight the difficulty of fine-tuning degree of functionalization in-house using standard laboratory techniques. We conclude that, when possible, it may be preferable to buy these biomaterials as they are largely becoming more commercially

available from well-known vendors like Sigma and others, to reduce batch-to-batch variability and maintaining the reproducibility of gelation without constant re-optimization.

2.6 References

1. Shoulders, M. D. & Raines, R. T. COLLAGEN STRUCTURE AND STABILITY. *Annu. Rev. Biochem.* **78**, 929–958 (2009).
2. Davidenko, N. *et al.* Evaluation of cell binding to collagen and gelatin: a study of the effect of 2D and 3D architecture and surface chemistry. *J. Mater. Sci. Mater. Med.* **27**, 148 (2016).
3. Loessner, D. *et al.* Functionalization, preparation and use of cell-laden gelatin methacryloyl-based hydrogels as modular tissue culture platforms. *Nat. Protoc.* **11**, 727–746 (2016).
4. Caliari, S. R. & Burdick, J. A. A Practical Guide to Hydrogels for Cell Culture. *Nat. Methods* **13**, 405–414 (2016).
5. Nichol, J. W. *et al.* Cell-laden microengineered gelatin methacrylate hydrogels. *Biomaterials* **31**, 5536–5544 (2010).
6. Van Den Bulcke, A. I. *et al.* Structural and Rheological Properties of Methacrylamide Modified Gelatin Hydrogels. *Biomacromolecules* **1**, 31–38 (2000).
7. Van Hoorick, J. *et al.* Highly Reactive Thiol-Norbornene Photo-Click Hydrogels: Toward Improved Processability. *Macromol. Rapid Commun.* **39**, e1800181 (2018).
8. Zhu, M. *et al.* Gelatin methacryloyl and its hydrogels with an exceptional degree of controllability and batch-to-batch consistency. *Sci. Rep.* **9**, 6863 (2019).
9. Hoorick, J. V. *et al.* Highly Reactive Thiol-Norbornene Photo-Click Hydrogels: Toward Improved Processability. *Macromol. Rapid Commun.* **39**, 1800181 (2018).

10. Vlierberghe, S. V., Fritzing, B., Martins, J. C. & Dubruel, P. Hydrogel Network Formation Revised: High-Resolution Magic Angle Spinning Nuclear Magnetic Resonance as a Powerful Tool for Measuring Absolute Hydrogel Cross-Link Efficiencies. *Appl. Spectrosc.* **64**, 1176–1180 (2010).
11. Hafidz, R., Yaakob, C. M., Amin, I. & Noorfaizan, A. Chemical and functional properties of bovine and porcine skin gelatin. *Int. Food Res. J.* **18**, 813–817 (2011).
12. Claaßen, C. *et al.* Quantification of Substitution of Gelatin Methacryloyl: Best Practice and Current Pitfalls. *Biomacromolecules* **19**, 42–52 (2018).
13. Karim, A. A. & Bhat, R. Fish gelatin: properties, challenges, and prospects as an alternative to mammalian gelatins. *Food Hydrocoll.* **23**, 563–576 (2009).
14. Zatorski, J. M., Montalbino, A. N., Ortiz-Cárdenas, J. E. & Pompano, R. R. Quantification of fractional and absolute functionalization of gelatin hydrogels by optimized ninhydrin assay and ¹H NMR. *Anal. Bioanal. Chem.* **412**, 6211–6220 (2020).
15. Yue, K. *et al.* Structural analysis of photocrosslinkable methacryloyl-modified protein derivatives. *Biomaterials* **139**, 163–171 (2017).
16. Shirahama, H., Lee, B. H., Tan, L. P. & Cho, N.-J. Precise Tuning of Facile One-Pot Gelatin Methacryloyl (GelMA) Synthesis. *Sci. Rep.* **6**, 1–11 (2016).
17. Aldana, A. A., Malatto, L., Rehman, M. A. U., Boccaccini, A. R. & Abraham, G. A. Fabrication of Gelatin Methacrylate (GelMA) Scaffolds with Nano- and Micro-Topographical and Morphological Features. *Nanomaterials* **9**, 120 (2019).
18. D. O’Connell, C. *et al.* Tailoring the mechanical properties of gelatin methacryloyl hydrogels through manipulation of the photocrosslinking conditions. *Soft Matter* **14**, 2142–2151 (2018).
19. Muñoz, Z., Shih, H. & Lin, C.-C. Gelatin hydrogels formed by orthogonal thiol–norbornene photochemistry for cell encapsulation. *Biomater. Sci.* **2**, 1063–1072 (2014).

20. Greene, T. & Lin, C.-C. Modular Cross-Linking of Gelatin-Based Thiol–Norbornene Hydrogels for in Vitro 3D Culture of Hepatocellular Carcinoma Cells. *ACS Biomater. Sci. Eng.* **1**, 1314–1323 (2015).

21. Khan, S. A., Plitz, I. M. & Frantz, R. A. In situ technique for monitoring the gelation of UV curable polymers. *Rheol. Acta* **31**, 151–160 (1992).

3 Micropatterning Hydrogels On-Chip

Some text and figures are adapted from: Ortiz-Cárdenas, J.E., Zatorski, J.M., Arneja A.

et al. In situ photopatterning of cell laden biomaterials

for spatially organized 3D cell cultures in a microfluidic chip. In review. *BioRxiv preprint.*

<https://doi.org/10.1101/2020.09.09.287870>

3.1 Abstract

Micropatterning techniques for 3D cell cultures enable the recreation of tissue-level structures, but the combination of patterned hydrogels with organs-on-chip to generate organized 3D cultures under microfluidic perfusion remains challenging. To address this technological gap, we developed a user-friendly in-situ micropatterning protocol that integrates photolithography of crosslinkable, cell-laden hydrogels with a simple microfluidic housing, and tested the impact of crosslinking chemistry on stability and spatial resolution. In this work we explained through the process of setting up a robust micropatterning-on-chip in a laboratory, identified equipment requirements and parameters to ensure reproducible gelation. Then we used the system to test gelatin functionalized with photo-crosslinkable moieties and found that inclusion of cells at high densities ($\geq 10^7/\text{mL}$) did not impede thiol-norbornene gelation, but decreased the storage moduli of methacryloyl hydrogels. Hydrogel composition and light dose were selected to match the storage moduli of soft tissues. To generate the desired pattern on-chip, the cell-laden precursor solution was flowed into a microfluidic chamber and exposed to 405 nm light through a photomask. The on-chip 3D cultures were self-standing and the designs were interchangeable by simply swapping out the photomask. Thiol-ene hydrogels yielded highly accurate feature sizes from 100 – 900 μm in diameter, whereas methacryloyl hydrogels yielded slightly enlarged features. Furthermore, only thiol-ene hydrogels were mechanically stable under perfusion overnight. Repeated patterning readily generated

multi-region cultures, either separately or adjacent, including non-linear boundaries that are challenging to obtain on-chip. As a proof-of-principle, primary human T cells were patterned on-chip with high regional specificity. Viability remained high (> 85%) after overnight culture with constant perfusion. We envision that this technology will enable researchers to pattern 3D co-cultures to mimic organ-like structures that were previously difficult to obtain.

3.2 Introduction

Photolithography of hydrogels in the presence of cells requires a careful balance of reduced cytotoxicity, while still achieving targeted biomimetic mechanical properties and features that remain stable under fluid flow. These requirements limit the choice of biomaterial and the extent of photo-exposure which has resulted in photopatterning largely limited to hydrogels without cells or with robust cell lines.¹⁻⁷ As discussed in the Introduction chapter, there are many considerations that must be considered when selecting a photoreactive chemistry for 3D culture implementation.

Radical mediated photopolymerization of biomaterials for 3D cultures is a well-established technique. For photopolymerization to start, regardless of chemistry, a photoinitiator must be present to catalyze the reaction. For this work we selected a type I (cleavage-type) photoinitiator, lithium acyl phosphinate (LAP) due to its moderate molar absorptivity at wavelengths > 400 nm ($25 \text{ M}^{-1} \text{ cm}^{-1}$) making it compatible for excitation under visible light and has been shown to be less damaging to cells.⁸

In terms of macromer selection, we decided to use naturally derived gelatin-based hydrogels because of their accessibility, the ability to control the mechanical properties and the lack of need for additional doping for cell adhesion motifs. There are two main polymerization chemistries utilized with these modified biomaterials: acrylate-based chain-growth (via gelatin-methacryloyl, GelMA)⁹ and thiol-ene based step growth polymerization

(via norbornene- or thiol-gelatin, GelNB or GelSH).^{10,11} While the specifics of each polymerization are described in the Introduction chapter, one of the biggest differentiators between these polymerization chemistries is the reactivity with dissolved oxygen. Chain-growth polymerization can be inhibited by oxygen, due to its rapid radical scavenging that results in reactive oxygen species,¹² thus under ambient conditions the reaction can take several minutes to complete. On the other hand, thiol-ene polymerization is insensitive to oxygen quenching. This allows for a much more efficient reaction progression, with gel points as low as 12 seconds.¹³ As a result of these enhanced properties, different groups have compared the performance of thiol-ene based biomaterials to the well-established, but often toxic, methacryloyl-based biomaterials and have confirmed increased biocompatibility with epithelial cell lines and human mesenchymal stem cells.^{10,13} However, GelMA has been used extensively for encapsulation of many cell types both through photolithography and other manufacturing techniques like 3D printing.^{14,12,15}

While both GelMA and GelNB/GelSH hydrogels have been used to encapsulate cells in 3D culture, these are seldom included with a fluidic system. A unique requirement for on-chip culture of free-standing cell-laden hydrogels is their stability under continuous fluid flow so that patterned hydrogels are not dissolved or washed away. Without systematic testing of what factors control such stability, it remains difficult for laboratories to adopt on-chip photopatterning without extensive materials optimization. Additionally, there has not been a systematic testing of how these two biomaterials that follow distinct polymerization chemistries differ in terms of accuracy or how the mechanical properties of the hydrogels are affected by the inclusion of cells at high densities, which are essential to mimic organ tissues.¹⁶

In this work, we provide a route towards spatially organized organ-on-chip cultures by developing a method to pattern cell-laden hydrogels into customizable, free-standing

structures on a microfluidic chip by in situ photolithography. Throughout the Chapter, we will discuss in detail all necessary components to create a robust on-chip photopatterning set up in a laboratory; from selecting equipment, best practices for reagent handling, impact of temperature in reproducibility and optimization of the microfluidic housing. Once a robust process for photopatterning was in place, we investigated the performance of gelatin-based biomaterials with either methacryloyl or thiol-ene polymerization chemistries. We determined the effect of cell encapsulation on the storage moduli of each type of hydrogel and established conditions for biomimetic stiffness typical of soft tissues. We tested the effect of gelation chemistry and storage modulus on resolution and accuracy of the patterning on-chip, as well as the mechanical stability of free-standing micropatterns under fluid flow. Using this method, we demonstrated the capacity to create self-standing arrays and complex, non-linear hydrogel features using sequential photomasks. Finally, we demonstrated the use of in-situ photo-patterning for primary human cells, specifically T lymphocytes, and determined the cytocompatibility and spatial specificity of this micropatterning method.

3.3 Materials and Methods

3.3.1 Hydrogel materials and sourcing

Thiol-modified gelatin (GelSH; Lot: MKCJ5413) was obtained from Sigma Aldrich and used as provided. The vendor-reported absolute degree of functionalization for this material, determined by free thiol assay, was 0.223 mmol -SH / g gelatin. 8-arm PEG-NB 20 kDa (Jenkem Technologies), lithium phenyl-2,4,6-trimethylbenzoylphosphinate (LAP; Sigma Aldrich), and 1x phosphate buffered saline without calcium or magnesium (1x PBS; Lonza) were also used as provided. Gelatin methacryloyl (GelMA; Lots: MKCK4076 and MKCK5644) with vendor-reported fractional degrees of functionalization of 70% and 32%, respectively, were obtained from Sigma Aldrich. The absolute degrees of functionalization

were also measured in-house by H-NMR, as described by Zatorski et. al. (2020) ¹⁷ and found to be 0.232 and 0.088 mmol -MA/g GelMA, respectively.

3.3.2 Silicon master fabrication

A one-layer microfluidic device was fabricated using standard soft lithography methods. Transparency masks were drawn in AutoCAD LT 2017-2019 and printed at 20,000 DPI by CAD/Art Services, Inc. (Brandon, OR). The master molds were fabricated using SU-8 3050 photoresist spun to 124 – 136 μm thickness (Microchem, Westborough MA, USA) on 3" silicon wafers (University Wafer, South Boston MA, USA) and vapor silanized with Trichloro(1*H*,1*H*,2*H*,2*H*-perfluorooctyl) silane (Sigma Aldrich) for 2 hours. Degassed polydimethylsiloxane (PDMS) was prepared at a 10:1 ratio of elastomer base to curing agent (Slygard 184 Silicone Elastomer, Ellsworth Adhesives, Germantown WI, USA), poured over the silicon SU-8 master, and cured in a 70 °C oven for at least 2 hours.

3.3.3 Surface functionalization of microfluidic chips

Once cured, the PDMS was removed from the master and punched at the channel ends using a 0.75-mm I.D. tissue punch (World Precision Instruments, Sarasota FL, USA) to create inlets for PTFE TT-30 tubing (Weico Wire Inc.). The PDMS layer and a Goldseal cover glass (35 x 50 mm x 0.15 mm, actual thickness 0.13-0.16 mm, Ted Pella, Inc.) were oxidized in a plasma cleaner for 20 seconds (air plasma; Tegal Plasmod) or for 10 seconds with BD-20AC laboratory corona treater¹⁸ (Electro-Technic Products, Chicago IL, USA), manually assembled, and incubated in a 120 °C oven for 10 minutes to complete the bonding process.

A rigid poly (methyl methacrylate) (PMMA) cover was fabricated to serve as a backing for the photomask. To avoid light scattering or absorption during photocrosslinking, a hole was cut into the PMMA over the culture chamber. Specifically, a 50 x

45 x 1.5 mm acrylic sheet (McMaster-Carr, Princeton, NJ USA) was etched with a 10-mm central hole by using a CO₂ laser (Versa Laser 3.5, Universal Laser System, Scottsdale, AZ) set to 20% power and 1% speed.

3.3.3.1 Methacryloylation of surfaces

Glass slides or cover-slips were rinsed with 200-proof ethanol and DI water 3x and dried with N₂. Liquid phase silanization was performed by creating a fresh solution of 1:200 dilution of 3-(Trimethoxysilyl)propyl methacrylate (TMSPMA, methacrylate silane; Sigma Aldrich) in ethanol containing 3% v/v of 1:10 diluted acetic acid was and submerging plasma treated (60 s) pieces of glass and punched PDMS for 30 minutes. Surfaces were rinsed with ethanol and DI water and dried with N₂. A PDMS mask, was placed on top of the device chamber and both PDMS and glass slides were exposed to plasma for 60s before being brought into contact for non-reversible bonding. The device was covered with tape to prevent dust accumulation and stored in a desiccator containing Dri-rite. MA-functionalized devices were used within 2 days of being silanized.

3.3.3.2 Thiolation of surfaces

Once bonded, the device was then purged with nitrogen for 10 min, followed by 90 min of vapor silanization using (3-Mercaptopropyl) trimethoxy silane (SH-terminated silane, Sigma Aldrich) in a nitrogen-filled environment. After silanization, the device was rinsed with 70% ethanol and distilled water, purged with a nitrogen gun to remove excess moisture, and placed in a 120 °C oven to dry completely for at least 10 min. Once dried, the device was covered with tape to prevent dust accumulation and stored in a desiccator containing Dri-rite. SH-functionalized devices were used within a week.

3.3.4 *Assessing patterning resolution*

Chips were assembled as described above, with the bottom layer comprised of either a coverslip (0.13 – 0.16 mm thickness) or a 1-mm thick Corning® Glass Slides, 75 x 50 mm (Ted Pella, Inc.). In the case of GelSH, a precursor solution composed of 5% GelSH, 0.313- or 1.25-mM PEG-NB linker, 3.4 mM LAP, and 5 μ M NHS-Rhodamine was patterned on-chip as described above, using a 45 second exposure at 50 mW/cm². In the case of GelMA, a precursor solution composed of 10% GelMA, 3.4 mM LAP, and 5 μ M NHS-Rhodamine was patterned on-chip as described above, using exposure at 50 mW/cm². The exposure times were 119 and 30 seconds for 70% and 32% DOF GelMA, respectively. For GelMA samples, the chips were placed in the incubator immediately for 1 min after light exposure to reduce the viscosity of the material for rinsing. Un-crosslinked material was rinsed out with 1x PBS for 5 min at 5 μ L/min, after which the inlet and outlet were closed using TT-30 (Weico Wire) tubing filled with PDMS. The chips were placed in an incubator (37 °C, 5% CO₂) for 30 minutes in the absence of flow, then chips rinsed once more with 1x PBS for 5 minutes at 5 μ L/min. Features were imaged by brightfield and fluorescence microscopy on a Zeiss AxioZoom microscope (HE 43 filter set). The diameter of each feature was quantified from the fluorescence images by using line tools in ImageJ v1.52k.

3.3.5 *GelSH/GelMA characterization and cell encapsulation*

For rheological measurements of GelSH hydrogels, the precursor solution was prepared by combining reagents to a final concentration of 5% w/v GelSH, 2.5 or 10 mM norbornene (0.313- or 1.25-mM PEG-NB linker), and 3.4 mM LAP in 1x PBS. The PEG-NB linker was added right before the sample was to be pipetted onto the stage of the rheometer. For GelMA, reagents were combined to a final concentration of 5 or 10% w/v

GelMA and 3.4 mM LAP in 1x PBS. When cells were included during photopolymerization, cells were spun down and resuspended at 10 or 15 x 10⁶ cells/mL in precursor solution.

Rheological characterization was performed using a MCT302 Anton Parr Rheometer, operated in oscillatory time sweep mode with 5% strain, 1 Hz frequency, and 0.1 mm gap to assess gel polymerization rate and storage modulus. A UV-curing stage was fitted with a 20-mm parallel plate, the light source was filtered through a 400-500 nm filter, and the stage temperature was maintained at 25 °C, unless otherwise noted. 30 μ L of precursor solution was pipetted onto the stage. After measuring baseline shear storage modulus for 30 seconds, light exposure was initiated with constant intensity of 50 mW/cm², unless otherwise noted.

3.3.6 Cell Sourcing

3.3.6.1 Murine splenocytes

C57BL/6 mice were purchased from Jackson Laboratory or Taconic (USA) and housed in the University of Virginia vivarium with food and water ad libitum. All animal work was approved by the Institutional Animal Care and Use Committee at the University of Virginia under protocol #4042, and was conducted in compliance with guidelines the Office of Laboratory Animal Welfare at the National Institutes of Health (United States).

On the day of the experiment, the animal was anesthetized with isoflurane and euthanized by cervical dislocation. The spleen was removed, and immediately placed into ice-cold DPBS without calcium or magnesium (Lonza, Walkersville MD, #17-512F) with 2% heat-inactivated FBS (Gibco, Fisher Scientific, Waltham, MA). Spleens were crushed through a 70 μ m mesh filter into 10 mL complete media. Complete media consisted of RPMI (Lonza RPMI 1640 without L-glutamine, #12-167F) supplemented with 10% FBS, 1% L-glutamine, and 1% Pen/Strep, 50 μ M beta-mercaptoethanol, 1 mM pyruvate, 1%

non-essential amino acids, and 20 mM HEPES (Fisher Scientific). All centrifugal steps were for 5 minutes at 400xg. Samples were centrifuged, supernatant removed, and lysed with 2mL ACK lysing buffer for 1 minute. 2 mL of 2% serum in PBS (flow buffer) was immediately added. Samples were centrifuged, supernatant removed, and suspended in 10mL complete media. Cells were counted on inverted microscope with hemocytometer and trypan blue (Fisher Scientific) (1:10 sample:trypan blue v/v) and kept in ice until needed.

3.3.6.2 Human CD4+ T cells

Human naïve CD4+ T cells were purified from TRIMA collars, a byproduct of platelet apheresis, obtained from healthy donors (Crimson Core, Brigham and Women's Hospital, Boston, MA and INOVA Laboratories, Sterling, VA). Initially, total CD4+ T cells were isolated using a combination of the human CD4+ T cell RosetteSep™ kit (STEMCELL Technologies) and Ficoll-Paque (Cytiva Inc.) density centrifugation. Naïve CD4+ T cells were then enriched from total CD4+ T cells through immuno-magnetic negative selection with the EasySep™ Naïve CD4+ T cell isolation kit (STEMCELL Technologies). Naïve CD4+ T cell post-isolation purity (CD4+CD45RA+CD45RO-) was determined through flow cytometry.

3.3.7 Photopatterning and viability of murine splenocytes

Murine splenocytes collected as specified above. “Fresh” controls are cells never exposed to light and “Killed” controls were obtained after resuspending cells in 35% ethanol for 10 minutes. For GelMA: Precursor was prepared to a final concentration of 10% GelMA and 3.4 mM LAP photoinitiator in 1x PBS. Photo-patterning occurred as explained above with an exposure time of 60 seconds at 50 mW/cm². For GelNB precursor solution was prepared to a final concentration of 5% GelNB, 15 mM 4 arm PEG-thiol 5

kDa and 3.4 mM LAP in 1x PBS. Photo-patterning occurred as explained above with an exposure time of 60 seconds at 50 mW/cm². Chips were incubated for 1 hour under fluid flow at 0.5 μ L/min driven by a Chemyx Fusion 200 syringe pump. Cells were stained with 5 μ M Calcein-AM and 5 μ M Propidium Iodide for 20 minutes and rinsed with PBS for 5 minutes. Imaged with Zeiss AxioZoom microscope. Data analyzed as mentioned above. Live cells determined by #Calcein-AM stained cells/# Calcein-AM+#DAPI cells.

3.3.8 Photopatterning and viability of human T cells (GelSH)

CD4⁺ T cells were labelled using 10 μ M NHS-rhodamine for 20 min at room temperature, rinsed in 1x PBS to remove excess dye by centrifugation at 400 x g for 5 min and resuspended in AIM V serum-free medium (Gibco; Thermo Fisher Scientific, Inc.) supplemented with 10 ng/mL recombinant human IL-7 (R&D Systems; Bio-technie, Inc.) until use.

For micropatterning, cells were resuspended in precursor solution at 1.5×10^7 cells/mL. The 8 arm PEG-NB was added to the precursor to a final concentration of 0.313 mM or 1.25 mM for final concentrations of 2.5 or 10 mM norbornene, respectively, immediately before filling the syringe. Cells were flowed into the device for 2 min at 5 μ L/min and photo-patterned as described above. Micropatterned cultures were incubated in a cell culture incubator (37 °C, 5% CO₂) for 12 hours under continuous perfusion of media (AIM-V, supplemented with 10 ng/mL recombinant human IL-7) at 1.2 μ L/min.

After the culture period, the viability of cells was assessed by flowing in a staining solution of Calcein-AM (10 μ M) and DAPI (1 μ M) in 1x PBS for 2 min at 5 μ L/min, which was incubated on-chip for 20 min at 37 °C, then rinsed out for 10 min with 1x PBS at 5 μ L/min using a syringe pump. Images were collected using a Zeiss AxioZoom microscope, collecting two to four focal planes per location. Data analysis was performed in ImageJ,

as follows: The z-stack images from each location were stacked and converted into a Max Intensity Projection. Cells were identified by using the Particle Analyzer tool (circularity 0.5 – 1, size 12.5 – 500 μm^2). The percent of live cells was quantified as Calcein-positive cells/ (Calcein-positive + DAPI-positive cells). In preliminary experiments, we confirmed that this concentration of DAPI was low enough to label only the dead cells, and did not double-label Calcein-positive cells.^{19,20}

To quantify cell density inside and outside of the patterned structures, images were analyzed using ImageJ. Cells were identified by using the Particle Analyzer tool (circularity 0.5 – 1, size 12.5 – 500 μm^2). Cell density was calculated as the number of cells per unit area (mm^2), by selectively analyzing the area inside of all hydrogel features and the negative space in the chamber outside of the features.

3.3.9 Widefield Imaging

Except where noted below, imaging was performed on an upright Zeiss AxioZoom microscope equipped with a HXP 200C metal halide lamp, PlanNeoFluor Z 1x objective (0.25 NA, FWD 56 mm), and Axiocam 506 mono camera. For fluorescence imaging, filters used were Zeiss Filter Set 38 HE (Ex: 470/40, Em: 525/50), 43 HE (Ex: 550/25, Em: 605/70); 64 HE (Ex: 587/25, Em: 647/70); and 49 HE (Ex: 365, Em: 445/50). Brightfield images were collected using transmitted light. Zen 2/3 Blue software was used for image collection, and images were analyzed in ImageJ v1.52k.

For imaging cells after overnight culture, we used a Zeiss AxioObserver 7 inverted microscope equipped with a Colibri.7 LED light source, EC Plan-Neofluar 5x objective (N.A.=0.16, WD=18.5 mm), and ORCA-Flash4.0 LT+ sCMOS camera (Hamamatsu). For fluorescence imaging, the filter used was a Zeiss 112 HE LED penta-band. Zen 3 Blue software was used for image collection.

3.3.10 PDMS bubble trap fabrication

To minimize accumulation of bubbles in the microdevice, home-made PDMS bubble traps were used based on the design described by Jiang et al.²¹ In short, a thick (3.5 mm) piece of PDMS containing an 8 mm-long channel (380 μm wide x 585 μm high) was punched with a 5-mm tissue punch to make a cylindrical reservoir. A 0.75-mm tissue punch was used to create a horizontal inlet near the top of the reservoir, to accommodate TT-30 tubing. An outlet was made using a 2.5 mm tissue punch, to accommodate polysiloxane tubing (0.5 mm I.D., 2.2 mm O.D., BioChemFluidics). All tissue punches were from World Precision Instruments, (Sarasota FL, USA). The PDMS layer was plasma bonded to a 1-mm thick glass slide to close the channel, and a flat piece of PDMS was plasma bonded to the open top of the reservoir to close it.

3.3.11 HyStem-C hydrogel preparation

Hydrogels were prepared according to the manufacturer's protocol (HyStem®-C, Advanced Biomatrix, Carlsbad, CA). Briefly, Gelin-S, Extralink and Glycosil solutions were left to thaw for 1 hour at room temperature, then placed on a rocker for 15 min. The components were added in a 1:2:2 ratio in the following order: Extralink, Gelin S and Glycosyl. The mixture was carefully pipetted up and down to ensure well mixing and avoiding introduction of too many air bubbles. 100 μL of this mixture were pipetted onto the transwell and placed in an incubator for 60 minutes to ensure complete crosslinking, before being used.

3.3.12 Permeability of hydrogels

The hydrogel precursor of interest is added to the top side of the membrane of a 12 mm Transwell, pore size 12 μm (10 mm ID, MilliCell) and allowed to solidify via thermal

gelation or through photocrosslinking. The transwell is then placed inside the well in a 24-well culture plate, on top of 100 μL of PBS covering the bottom part of the membrane, preventing air gaps that can lead to fluid flow resistance. A column of PBS (700 μL), with known height L , can be placed on top of the hydrogel, creating a pressure difference that will induce flow to pass through.

Equation 3-1

$$k = \frac{\mu L Q}{A * \Delta P}$$

where k is the hydraulic permeability (cm^2), μ is the fluid viscosity ($\text{Pa}\cdot\text{s}$), Q is the flow rate (cm^3/s), A is the cross-sectional area of the transwell (cm^2) and ΔP is the change in pressure (Pa) and

Equation 3-2

$$\Delta P = g\rho L$$

where g is the acceleration constant ($1/\text{s}^2$), ρ is density of fluid (g/cm^3) and L is the height of column of fluid (cm).

3.4 Results

3.4.1 Optimization of microchip design

3.4.1.1 Main Design Considerations

Design of a microchip that would serve as housing for micropatterned 3D cultures that would mimic a lymph node had to have the following components: (1) incoming channels (simulating afferent vessels) (2) culture chamber (3) outgoing channels (simulating efferent vessels).

3.4.1.2 Microposts

Based on computational simulations, it is believed that 90% of lymph fluid flow occurs through the LN's subcapsular sinus (SCS), with flow velocities on the scale of mm/min and $\mu\text{m}/\text{min}$ for the cell-packed sub-architectures of the LN.²² In early iterations of the microfluidic device, we sought to create a path with low resistance to fluid when compared to a hydrogel, to mimic the SCS. Microposts or micropillars are useful in microfluidics to create separation between components by taking advantage of the air-liquid surface tension.²³ Thus implementation of microposts in the chip design was intended to help in two ways (1) would create a biomimetic separation between bulk hydrogel and the walls of the device, mimicking subcapsular sinus of the lymph node (2) and help direct filling, minimizing air pockets and. With this goal in mind, a barrier of microposts was designed into the chamber area of the chip. The spacing of these microposts was $\sim 25 \mu\text{m}$ enough for the viscous hydrogel precursor to be pinched at the interface. Additionally, the diameter of the microposts was optimized at $200 \mu\text{m}$ and the geometry changed from rectangular posts to circular posts, this ensured easier removal from the master mold. Since in order to obtain micropillars, the SU-8 master mold has to have a negative impression, or a microwell, it was often difficult to remove uncured SU-8 photoresist from inside the wells when they diameter was smaller than $200 \mu\text{m}$ and with a rectangular geometry. This created inconsistent development of micropillars which would leak to leakage into the "sinus" area (Figure 3-1a). Moreover, the placement of the pillars was slightly modified to prevent air accumulation at the top of the chamber which could expand at warmer temperatures like in an incubator (Figure 3-1b,c).

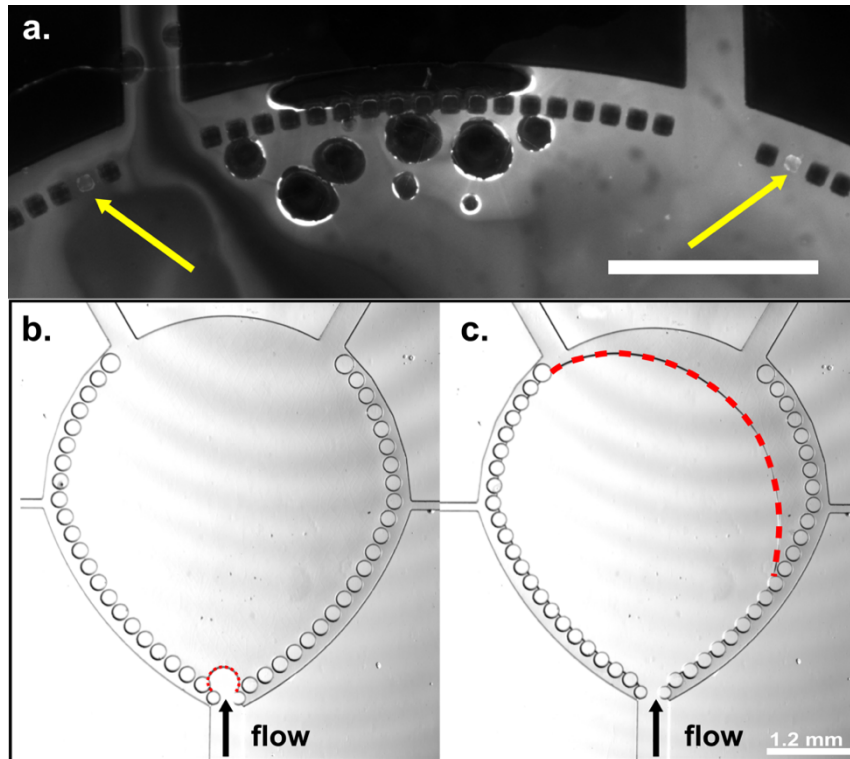


Figure 3-1 Micropillar optimization a) Unsuccessful filling with NHS-Rhod labelled precursor. Bubbles accumulate in the chamber and top area of the chamber. Arrows point to “ripped” $100\ \mu\text{m}$ wide micropillars when PDMS was peeled from SU8 master. Scalebar 1 mm. (b) – (c) Modified micropillars showing a successful filling. Dashed lines follow the interface between precursor and air inside the chip, no air gets trapped.

The microposts were no longer needed, based on other improvements like decreased chamber size and high patterning resolution, and were eventually eliminated in later iterations of the microfluidic chip. However, if necessary, the optimization in size and spacing could be implemented in other types of devices like those who wish to incorporate temperature-dependent hydrogels.

3.4.1.3 Chamber design

Initially, the culture chamber of the chip was designed to resemble the dimensions of human lymph nodes, approximately 1 cm. To this end, we created a circular 10 mm

wide culture chamber, with enough surface area to accommodate large, 3D cell cultures (Figure 3-2). However, even with the inclusion of the microposts discussed above, issues with inconsistent filling persisted. We decided to make two design changes. The first was to reduce the total volume of the chip by modeling the dimensions on murine lymph nodes which are in the range of a few mm, reducing the diameter from 10 mm to 4.4 mm. Next, we decided to taper the chamber at each end to facilitate smooth filling (Figure 3-2). Similar to problems faced when filling microwells or grooves where the advancing angle θ_a is larger than the angle α , defined as the angle between the wall and the diagonal of the well, the liquid will touch the opposite edge of the microwell before completely filling, creating an air pocket. Geometrical changes to the well/groove design leading to a larger angle α , such as a tapered aperture or an increased width to height ratio, can ensure a good filling.²⁴ These changes circumvented issues of air trapping while filling and are recommended to remain for future iterations of the device.

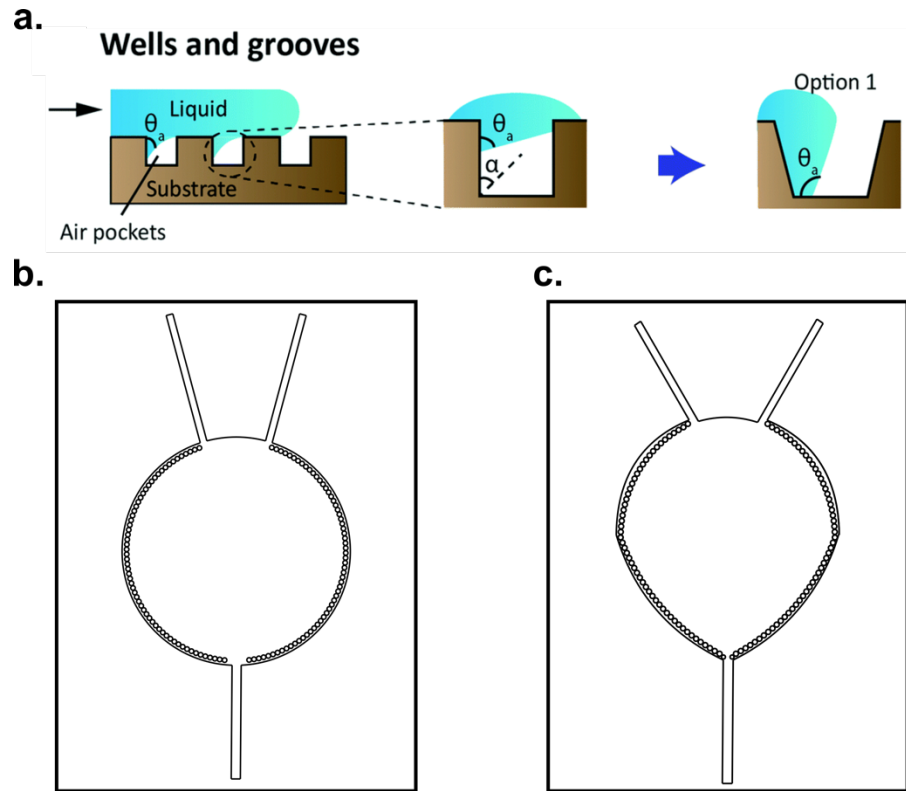


Figure 3-2 Optimization of chamber design for efficient filling. a) Examples of microwells and grooves on device substrate contributing to bubble formation on chip. *Reproduced with permission from* [24]. Schematic of (b) original chip design with circular chamber (c) modified chamber with tapered entrance to facilitate filling.

3.4.2 Chip materials and surface modification

The device was constructed from a thin layer of polydimethylsiloxane (PDMS) that was irreversibly bonded to a glass coverslip (Figure 3-3a). PDMS is a well characterized, gas-permeable polymer that has been successfully used for many on-chip cell culture applications, is readily silanized to control surface chemistry, and is transparent for photocrosslinking and optical imaging.²⁵ For this work, the microchamber was designed with a 130- μm depth, sufficient to mimic a 3-dimensional tissue structure, and a 4.4-mm diameter at its widest point to provide sufficient surface area for complex patterns. These dimensions could be tailored readily in the future for specific applications. The chamber

was tapered at each end to facilitate smooth filling.²⁴ In order to covalently anchor the patterned, norbornene- or methacryloyl-bearing hydrogel to the surface of the chip, the interior of the device was oxidized in a plasma cleaner and functionalized with either a thiol- or methacrylate-terminated silane, respectively (Figure 3-3b).

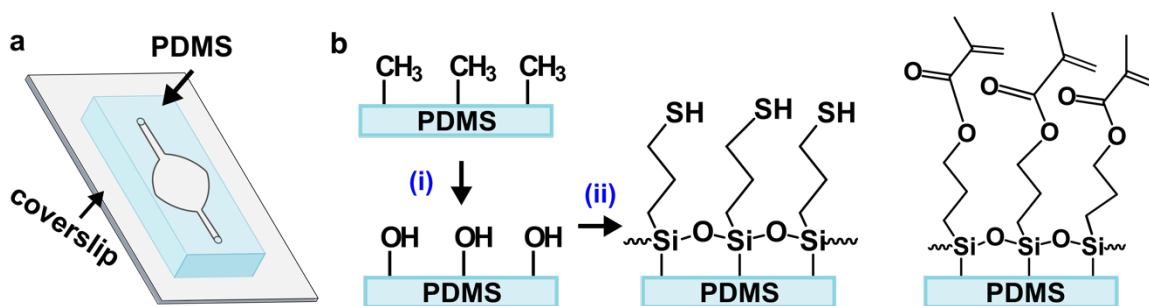


Figure 3-3 Chip fabrication and surface functionalization (a) Schematic of chip: thin layer of PDMS bonded to a glass coverslip. (b) Surface functionalization of PDMS. The methyl surface was (i) activated via oxidation with air plasma, followed by (ii) silanization using either thiol-terminated (left) or methacrylate-terminated (right) silane, to match the intended hydrogel.

3.4.2.1 Optimization of surface oxidation

An unexpected issue was observed when attempting to pattern hydrogels inside the PDMS-glass microfluidic device. Unintentional stripes were being templated in the PDMS and transferred to the hydrogels. The following conditions were tested to try to reduce PDMS cracks. Initially, silanization of the surfaces was being done in liquid phase. One hypothesis about what was causing the cracks was potential heterogeneous deposition of silane. In order to test this, 1) the phase of silanization was changed to vapor deposition which could give a more homogeneous surface treatment. However, this change did not result in improvements to crack's appearance. Next, we tested 2) decreasing silanization treatment time from 30 min to 3 min. This would test the hypothesis that cracks

were the result of excess silane being deposited on the surface; cracks were still apparent. Another potential cause could be heat expansion of the PDMS during “drying” time, after excess silane had been rinsed off. To test this, 3) PDMS pieces were dried under vacuum, rather than through direct heat, but cracks remained visible. We also investigated the effect of solvent induced swelling, since the PDMS may have been swelling in the presence of ethanol. We varied the solvent composition to 1:1 water to ethanol, while retaining the concentration of silane constant, but cracks still appeared. All the conditions and outcomes are summarized below (Table 3-1).

Table 3-1 Summary of PDMS treatment tested to reduce cracks produced during silanization.

Treatment	Cracks (Y/N)
Vapor Deposition of Silane	Y
Liquid Deposition of Silane	Y
Reduced silanization time (10x less)	Y
PDMS drying via vacuum (no oven)	Y
Reduced solvent induced swelling	Y
Reduced time of plasma exposure	N

Finally, we tested reducing the amount of air plasma time exposure of the PDMS, down to 20 seconds from the original 80 seconds (Figure 3-4). Laboratories often have established protocols with arbitrary times for air plasma treatment, which are normally determined by having enough oxidation to bond PDMS to glass. However, small cracks may occur if the surface is over-treated. This is explained by what happens during the plasma treatment; oxidation of the PDMS surface forms a thin, stiff silicate layer on the surface. When the PDMS cools, it contracts and places the silicate layer under compressive stress. This stress is relieved by buckling to form patterns of waves with wavelengths from 0.5 to 10 μm . The waves are locally ordered near a step or edge in

the PDMS.²⁶ These cracks are small defects on the PDMS surface which are unlikely to create noticeable issues to flow or other macrolevel applications. However, for our purposes, it was critical not to over-treat the PDMS surface with oxygen plasma, which caused cracks in the PDMS that templated defects in the hydrogel. This air plasma treatment optimization may be dependent on the specific equipment used for surface oxidation and may vary from laboratory to laboratory.

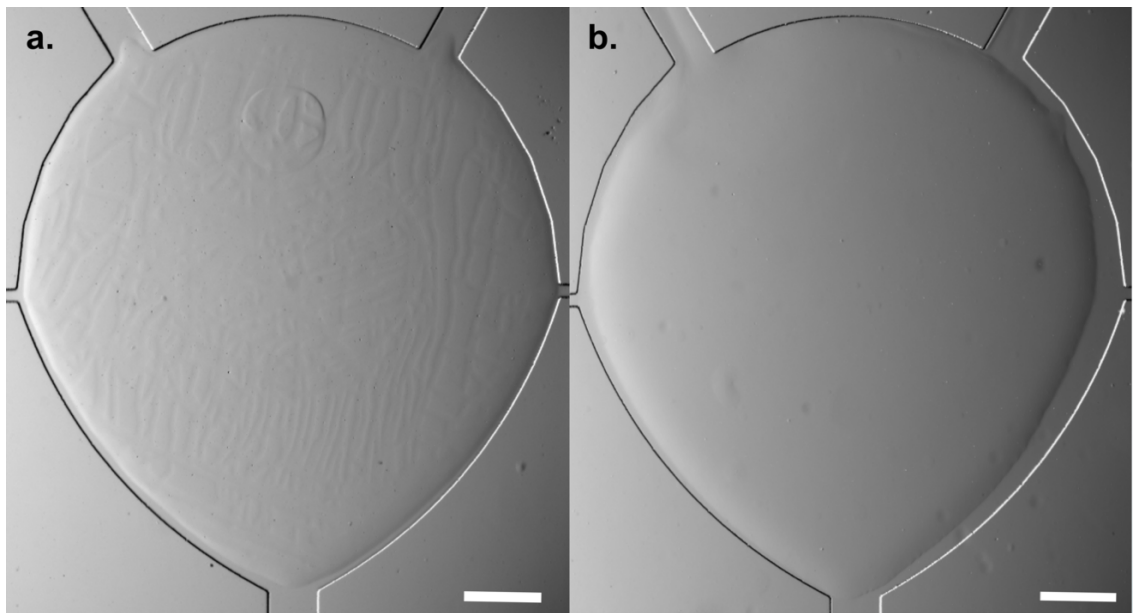


Figure 3-4 Optimization of plasma treatment. PDMS plasma treated for (a) 80 seconds; cracks in the PDMS, templated hydrogel creating undesired stripe-like pattern. (b) 20 seconds; no cracks developed in the PDMS, smooth pattern achieved. Scalebar 500 μm .

3.4.3 Equipment Selection: Light Source

3.4.3.1 Halogen lamp vs LED

Halogen lamps are widely popular in research labs, particularly in fluorescence microscopy set-ups due to their wide emission spectra that coupled with appropriate filter cubes can provide powerful combination of excitation and emission spectra leading to multi-color imaging. Light emitting diodes (LED's) on the other hand, are characterized for

having relatively narrow emission profiles. When considering which light source to use when building a photopatterning experimental platform, one must consider the ultimate use the light might have. For example, if your photoinitiator is excited in a wide range of wavelengths, the narrow bandwidth of an LED emission might be beneficial since it will minimize undesired absorbance particularly at shorter wavelengths. While this effect could be remedied in the halogen lamp by inclusion of bandpass filters, it requires additional funds which might be totally circumvented by switching to a narrow emission LED. However, if the research lab has a wide range of biomaterials that required exposure at different wavelengths or one decides to investigate the performance of a particular component at varied wavelengths, it could be more cost effective to purchase a halogen or arc lamp.

Amongst the drawbacks with halogen lamps are the subpar energy efficiency when compared with LED's. For example, in halogen lamps, up to 70% of the input power is converted to heat, with only 10% resulting in visible light.²⁷ This results in an overall shorter life-span for halogen bulbs and over time, other components like reflectors or filters may need replacement due to wear for operating at high temperatures. In contrast, LED's generate minimal heat and have expected lifetime of several thousands of hours,²⁸ making it both energy and cost-efficient alternative to halogen lamps. Because of all these advantages, we decided to select an LED-based system.

3.4.3.2 Collimated Light

There are many LED systems that can be easily purchased at drugstores, big-box retailers and online. These are often marketed for day-to-day applications like long-term nail polish curing, stain detection, night-time fishing and others. While these options might seem worth testing due to their relatively low cost (<\$200) compared to professional

equipment (>\$2000), they will not perform in a robust manner, leading to unnecessary troubleshooting. One of their limitations is the constricted modulation of light intensity. Many of these LED's are battery operated, which means as the battery drains, your output power may be decreasing and it may be difficult to ensure consistent doses. Additionally, these light sources often work in an on/off configuration, although more sophisticated ones may have a few power settings like "low, medium and high." These conditions restrict the ability to carefully select a particular output intensity and although the intensity of the light can be varied as a function of distance to the sample, where shorter distance often leads to higher intensity, one must consider the shape and size of the output beam. This becomes particularly problematic because the biggest shortcoming of LED's when applied to photolithography is their semi-spherical radiation pattern makes them less than ideal for illumination purposes that require high uniformity, particularly at small scales.²⁹ While a non-collimated light with moderate intensity may be sufficient to cure a bulk-hydrogel, they will not work for micropatterning at high resolution. Below is a list of commercially available light sources tested (Table 3-2).

Table 3-2 Compilation of LED light sources tested with comparison in beam irradiance at 365 and 405 nm. Intensity measurements taken at 10 mm from sample, where output beam looked homogenous. *These measurements are somewhat arbitrary since the intensity can be modulated up to ~200 mW/cm².

Model	Vendor	365 nm (mW/cm ²)	405 nm (mW/cm ²)	Collimation	Reproducible gelation?
VBestLife Mini LED Pen Light	Amazon	0.072	0.306	No	No
SUNUV, LED Nail Lamp	Amazon	2.66	27.48	No	No
LEDPL-5- UV395-PK	Larson Electronics	1.54	13	No	No
Tovatec UV LED Diving Light	Amazon	1.36	20	No	No
Fiber Coupled Violet LED light source + 0.5-inch fiber collimator	Prizmatix	1.113*	84.50*	Sold separately, included in calculations	Yes

In the end, a high power-violet (405nm) LED Light source coupled with a 1 mm optical fiber and a matching collimator was selected. A collimator, sometimes known as a condenser, transforms the diverging light-emission from an optical fiber to a parallel beam of light, creating a beam of homogenous intensity distribution (Figure 3-5). A collimator works by controlling the angular distribution of the illumination. It was important to match the numerical aperture (NA) of the collimator to the NA aperture of the optical fiber,

otherwise if the NA of the collimator were smaller, highly divergent rays will be lost causing a loss in a power output as well.

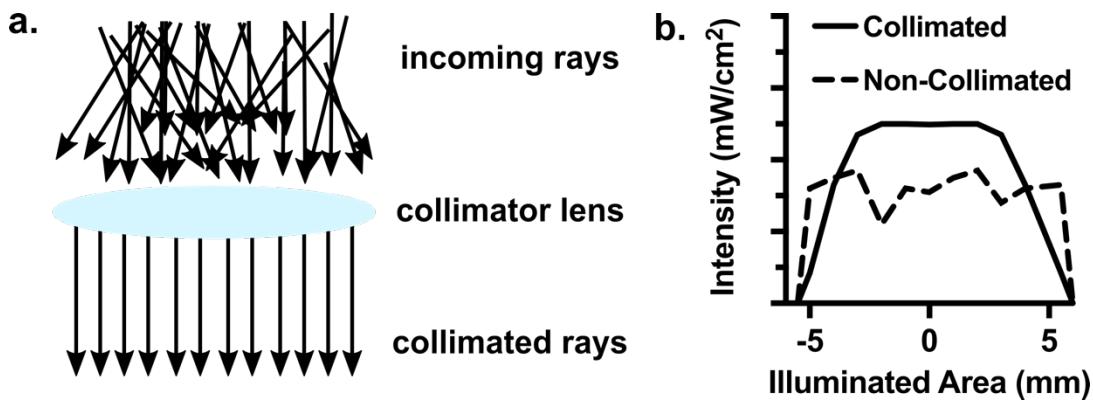


Figure 3-5 Importance of collimated light for micropatterning applications. a) Schematic of highly divergent (incoming rays) passing through a collimator lens only rays that are perpendicular to the surface will get through (collimated rays). b) Sketch of intensity profiles of output beam with and without collimation.

3.4.4 Selection of light intensity

One of the many variables that can influence the kinetics and the final mechanical properties of a photopolymerizable biomaterial is the choice of light intensity. The light intensity will directly correlate to a higher activation energy for the photoinitiators which increases the rate at which radicals are produced. Based on prior literature, it was expected that an increase in the amount of radicals produced would offset the rate of radicals quenched by oxygen present in the system.³⁰ The lowest intensity tested was 10 mW/cm², a commonly used value in the literature. We tested increments to 50 and 200 mW/cm² and tracked the photopolymerization (Figure 3-6). As expected, with the lowest intensity, there was a delay in polymerization, likely due to oxygen inhibition. Under atmospheric conditions (and a characteristic low rate of polymerization), the photoinitiator

absorbs light and reacts to form radicals that are preferentially consumed by dissolved oxygen.³⁰ A much faster polymerization was observed when using 50 mW/cm² with even more improvement when using 200 mW/cm², however it was concluded that the polymerization was not improved that much more to justify an increase of 4x the dose and risk cell damage. From this data, we selected 50 mW/cm² to use for all subsequent experiments, this was also informed by use of this intensity in similar GelMA photo-encapsulation published work.¹²

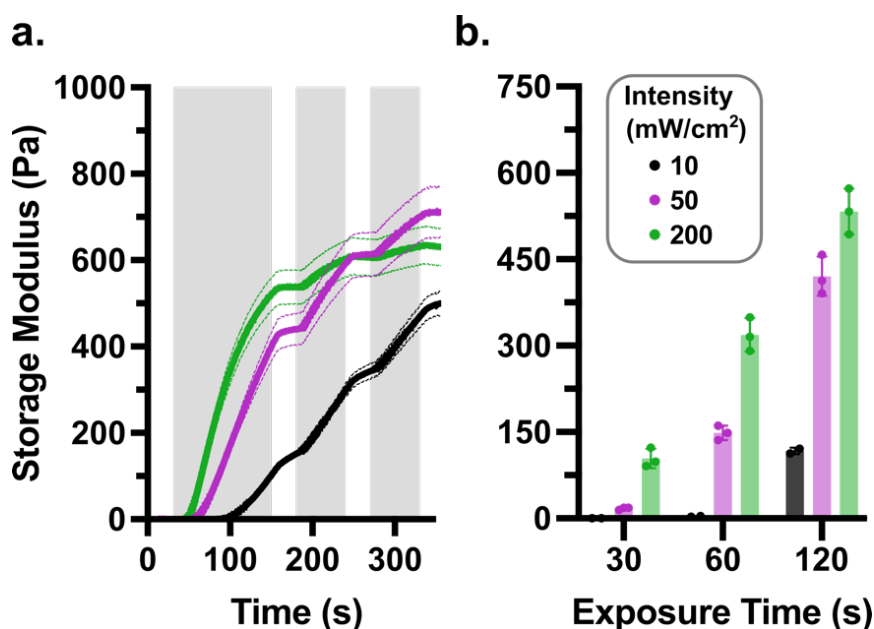


Figure 3-6 Optimization of light intensity for photopolymerization of 8% GelMA 0.1% LAP.

a) Rheometry measurements of the storage modulus of GelMA during *in situ* polymerization under light exposure at varied intensities. b) Comparison of shear storage modulus at different exposure times. Legend indicates the light intensity. Grey shading indicates when light was turned on.

3.4.5 Precursor reagents storage and stability: best practices

In order to obtain reproducible gelation of these biomaterials, it is critical to follow correct storage timing and conditions, values which are usually not reported in detail in the

literature. It is well-known that you must “prepare” your precursor the day before use, which usually means dissolving the lyophilized functionalized-gelatin biomaterial in PBS, adding the photoinitiator, and storing in in the fridge overnight to allow for full-hydration of the protein.⁹ However, newer laboratories adopting protocols might make small mistakes with storage or use of old reagents which can affect the gelation performance. For example, there is not much guidance about how long in advance you can prepare the precursor, or *if* and how “leftover” precursor from an experiment could be saved and used for a subsequent experiment. This section is meant to act as a quick reference guide, while also noting that slight modifications may have to be applied depending on the specific reagents and/or solvents used for a particular application. Below is a summary of good practices for storage and use of general precursor components (Table 3-3). While these were never systematically tested, through many years of use we have found useful to use the following guidelines.

Table 3-3 Summary of recommended reagent storage/lifetime for hydrogel precursors

Reagent	Vendor	Storage Temperature	Reagent Lifetime
LAP photoinitiator stock solution (0.75% in PBS)	Made in house; LAP: Sigma-Aldrich	4°C	3 months
PEG-(NB/SH) linkers in solution	Made in house; Linkers: Jenkem or Sigma Aldrich	4°C	1 month
Lyophilized Gel-(MA/NB/SH)	In-house synthesized or Sigma Aldrich	-20°C	6 months – 1 year
Dissolved precursor	-	4°C	3 - 5 days
Leftover precursor	-	4°C	1 additional freeze thaw cycles

When a batch of functionalized-gelatin is either synthesized in-house or bought from a commercial source, it often is synthesizing or shipped in at least 1 g aliquots. While it may be convenient to store the entire aliquot in one bottle, and remove smaller aliquots as needed, constant removal from the -20°C storage, means the protein will go through partial freeze-thaw cycles. We found that calculating approximately how much material is used in an average experiment and creating aliquots of this quantity, greatly decreased the degradation rate of the functionalized protein. Current aliquots that are stored in 3 mL conical tubes weight approximately 0.02 g, which yield 400 μ L of precursor for a 5% w/v solution. Sometimes one may prepare an aliquot, have significant leftover amounts and be tempted to use again to reduce reagent consumption. During use, these precursors are normally stored in an incubator, at 37°C, to prevent thermal gelation. We have had success with using leftover precursor within a day or two, but since it has already experienced a freeze thaw cycle, it is critical it is stored in the fridge overnight, and not kept in the incubator. Following these guidelines should ensure reproducibility of gelation.

3.4.6 Temperature effects on gelation reproducibility

Similar to other processes in a regular laboratory that require re-optimization based on difference in ambient temperature or humidity levels, we observed that reproducible gelation seemed to be impacted. An experiment was designed to directly test the effects of temperature in the reproducibility of mechanical properties of hydrogels. We varied the rheometer glass stage's temperature from 27, 25 and 23°C and compared gelation kinetics and resulting shear storage moduli (Figure 3-7). We observed that warmer temperatures, slightly delayed the rate of crosslinking. Additionally, when looking closer at the storage moduli values, although they were not statistically significant, we see greater variability within samples in warmer conditions. We hypothesized this is likely due

to the decreased viscosity of the precursor at warmer temperatures, which could enhance the diffusion of O₂ within the hydrogel precursor, which particularly for these GelMA samples could negatively affect the efficiency of crosslinking. Thus, we decided to include a cooling step in our photopatterning process that would ensure constant temperatures and eliminate temperature variations as a potential gelation inhibitor.

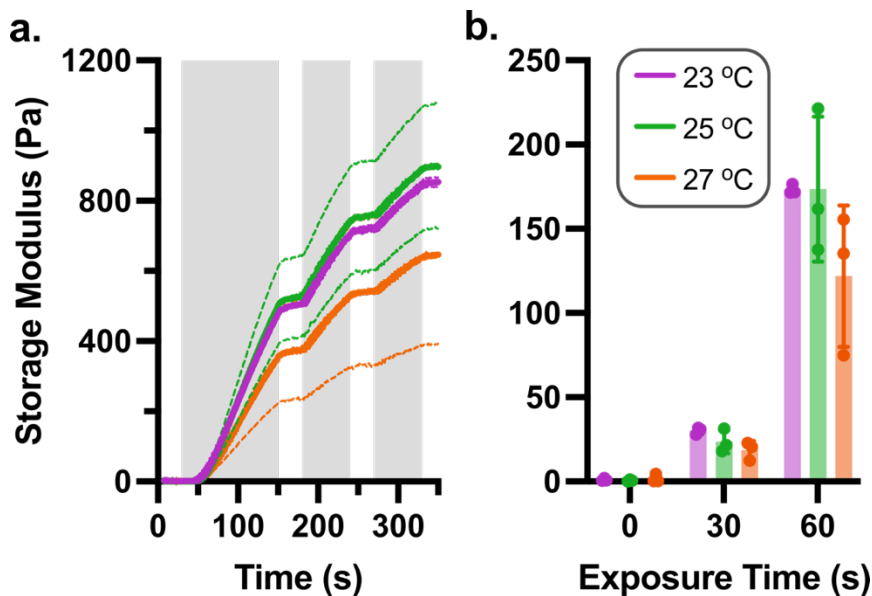


Figure 3-7 Temperature dependent *in situ* gelation of 10% w/v GelMA with 0.1%LAP. Grey shading indicates when light was turned on.

3.4.7 Photopatterning on-chip set up and process

The patterning process consisted of four steps (Figure 3-8a): After sterilization, the device was pre-wet with phosphate-buffered saline (PBS), filled with a precursor solution, and sealed off to prevent air entry. Precursor solutions consisted of gelatin monomer and any linkers, LAP, and the desired population of cells in suspension. The chip was placed briefly on a cooling stage to lower the temperature and ensure consistent gelation. Next, the photo-mask was aligned against the coverslip of the chip, and the chip was placed upside down below a collimated 405 nm LED light source and exposed (Figure 3-8b).

Finally, the inlet was unplugged, and unreacted precursor was removed by flowing PBS, leaving only the patterned culture.

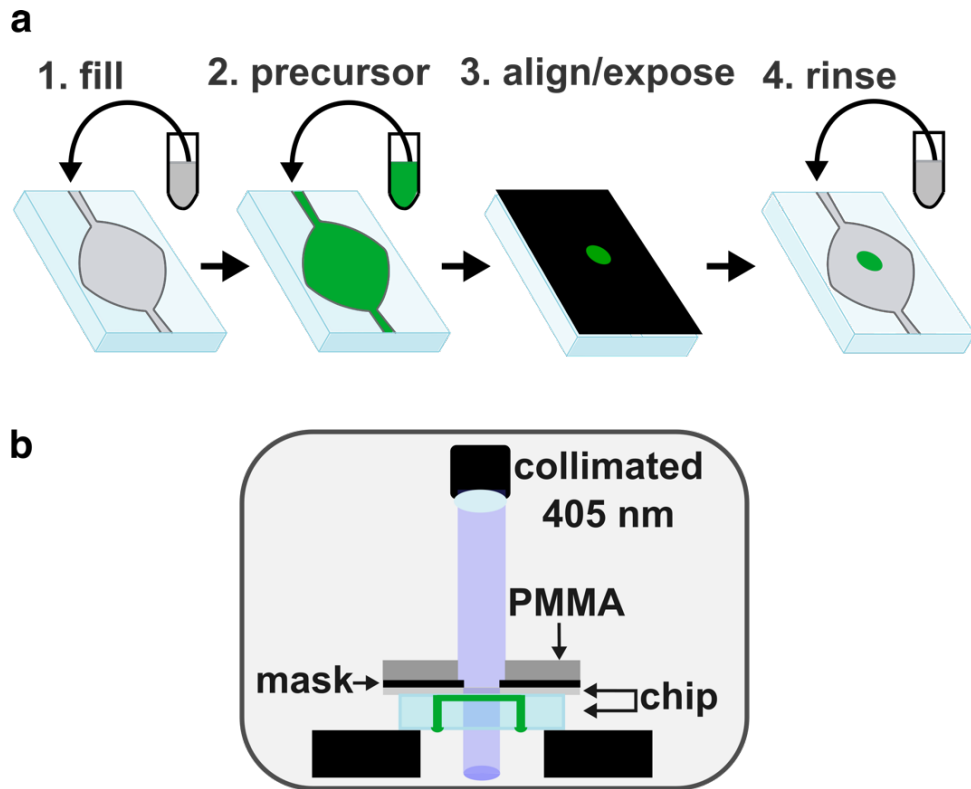


Figure 3-8 Photo-patterning set-up and process (a) Stepwise schematic of patterning process: 1) The chip was filled with buffer (grey), and 2) the buffer was displaced by precursor (green). 3) A photomask with desired design was aligned against the coverslip, supported with a rigid polymer backing (PMMA), clamped (not shown for clarity), and exposed. 4) Unreacted material was removed with a buffer rinse. If needed, the process was repeated with a different precursor to add additional structures. (b) Schematic of photo-patterning set up. The chip was placed upside down on top of two support layers (black) to suspend it below the collimated light source. The channels and chamber of the chip are shown filled with precursor (green).

The process was sequentially repeated with additional precursor solutions, e.g., containing different material compositions or different populations of cells. Once all

patterning steps were completed, culture media was flowed into the chip and transferred to a cell culture incubator for continued culture.

3.4.8 Precursor formulation for biomimetic storage moduli

In initial experiments in the absence of cells, the concentrations of gelatin-based macromer and linkers were selected to provide a biomimetic range of shear storage moduli (G'), 120 – 3000 Pa. This range matches that of typical soft tissues such as brain³¹ and lymphoid tissue (Figure 3-9).^{32,33} To access the lower and upper limits of the range, we used GelMA with varying degrees of functionalization (DOF) or varied the concentration of NB linker for GelSH, while the concentration of macromer was held constant. For GelMA, we selected 70% DOF 10% and 32 DOF 10% as the formulations to use moving forward with optimized doses of 5.95 J/cm² and 1.60 J/cm², respectively. For GelSH, we optimized doses for 2.5 mM NB and 10 mM NB to be 2.25 J/cm².

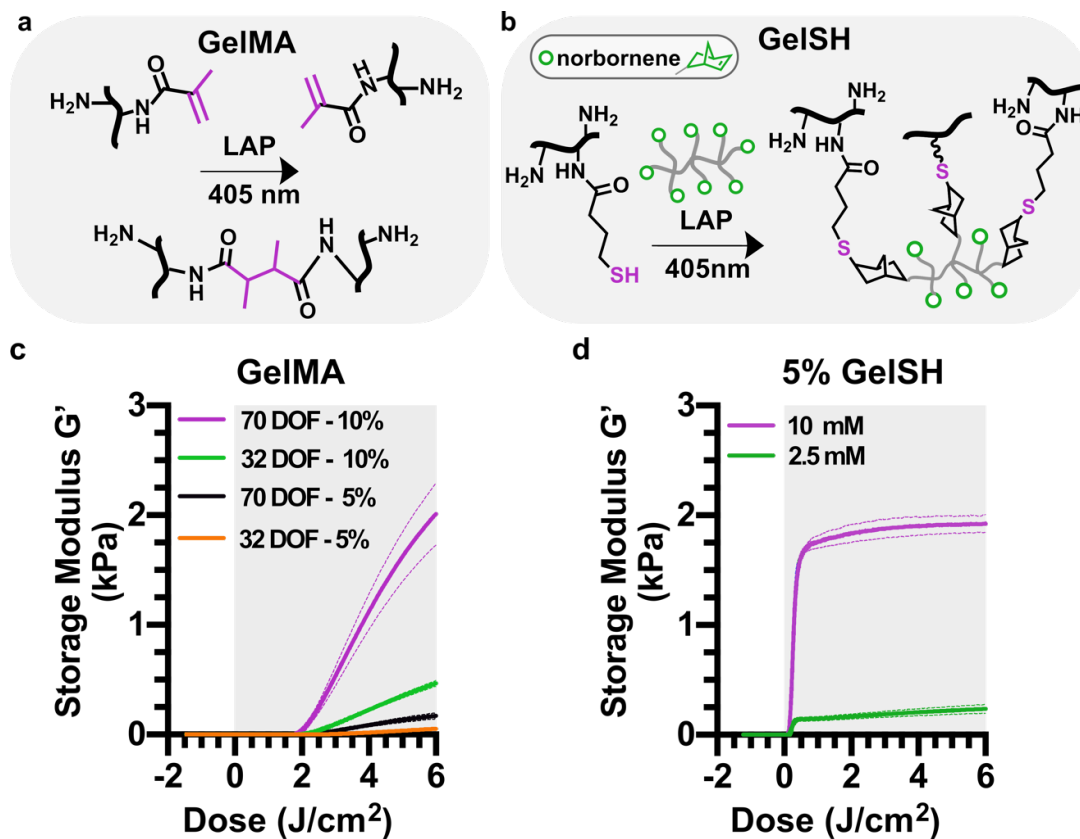


Figure 3-9 (a) Reaction scheme of GelMA (black, reactive carbons in magenta) crosslinking in presence of LAP and 405 nm light. (b) Reaction scheme of GelSH (black, thiol in magenta) with an 8-arm PEG-norbornene linker (grey, NB in green), catalyzed by the photoinitiator LAP and 405 nm light. (c) Rheometry measurements of the storage modulus of GelMA during *in situ* polymerization under constant light exposure at 50 mW/cm². Legend indicates the degree of functionalization (DOF, %) of the gelatin and concentration (% w/v) of GelMA present. n=3. (d) Rheometry measurements of the storage modulus of 5% w/v GelSH during *in situ* polymerization under constant light exposure at 50 mW/cm². Legend indicates the concentration of norbornene, where there is 8 mol norbornene per mol PEG-NB. Lines show mean (solid) and std deviation (dashed), n=3 technical replicates. Grey shading indicates when the light was turned on.

3.4.9 Impact of cell encapsulation in storage moduli as a function of chemistry

Since our approach to gelation required cells being present in the precursor as it polymerized, we investigated the extent of which the presence of cells at high densities influenced the mechanical properties of the various hydrogels. Inclusion of cells substantially altered the stiffness of GelMA hydrogels (Figure 3-10a). At low DOF (32%), 10 to 15 x 10⁶ cells/mL decreased the shear storage modulus by approximately 2-fold. At high DOF (70%), 15 x 10⁶ cells/mL had a similar effect. The data suggested that high cell densities may hinder the methacryloyl groups from reacting with one another, particularly at lower DOF. In contrast, in the GelSH-NB system, inclusion of cells had no impact on the storage modulus at low (2.5 mM) or high (10 mM) concentrations of the NB linker (Figure 3-10b).

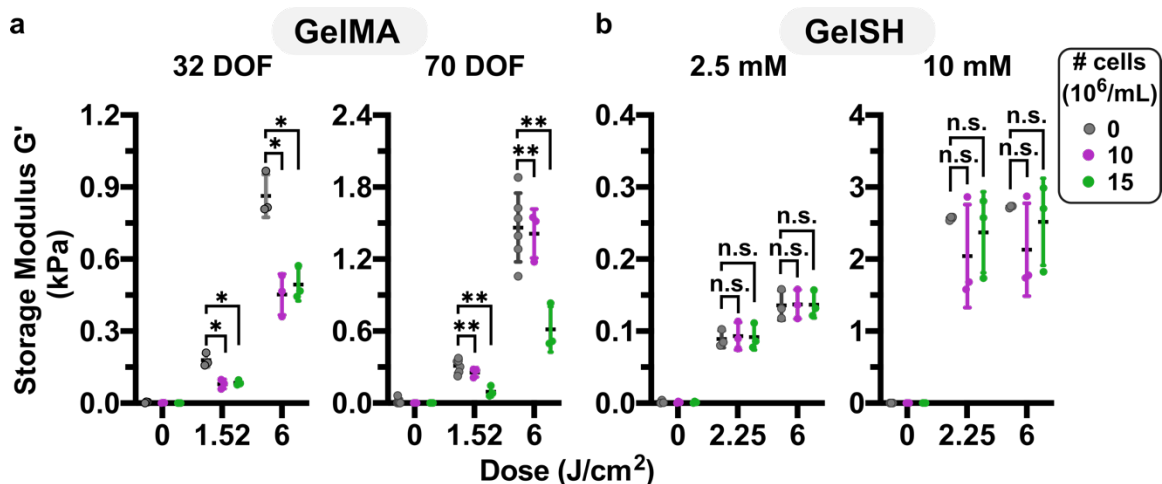


Figure 3-10 Impact of cell encapsulation on storage modulus of methacryloyl and thiol-ene hydrogels. (a,b) Shear storage moduli of GelMA and GelSH hydrogels formed in the presence or absence of cells, at varying doses of light, for (c) GelMA (10% w/v) at 32 or 70 % DOF, and (d) 5% w/v GelSH cross-linked with 2.5 or 10 mM norbornene. Legend gives density of human CD4+ T cells, in 10^6 cells/mL. n.s. $p > 0.05$, * $p \leq 0.05$, ** $p \leq 0.01$ via Two-way ANOVA with Sidak's multiple comparisons.

We speculate that the lack of effect of cells on storage moduli may be related to the network organization of the step-growth polymerized thiol-ene hydrogel. In the 10 mM NB hydrogels, G' values varied by ~ 2 -fold in the presence of cells, which we attribute to the challenge of adequately mixing the highly viscous precursor solution while maintaining cell integrity. While for some applications such variability may cause changes to biological activity, for our purposes the resulting G' values were within the range of interest. In sum, these formulations of GelMA and GelSH were able to form soft (< 1 kPa) hydrogels in the presence of high densities of cells, but GelSH was less affected and retained the ability to form gels in the 1-3 kPa regime as well.

3.4.10 Resolution of features based on gelation chemistry

The resolution and fidelity of patterning thick hydrogels by on-chip photolithography is expected to be limited by scattering of the incoming light and by diffusion of reactive species, as well as the mechanical properties of the hydrogel itself.⁷ Therefore, we tested the resolution and ability to pattern GelMA and GelSH hydrogels, whose different mechanisms of polymerization result in different organization of crosslinked networks.¹⁵ We initially hypothesized that hydrogels with a lower storage modulus, due to their lower cross-linking density, would have higher swelling ratios,³⁴ which would result in dimensions larger than intended. Resolution and accuracy of on-chip patterning were tested by using photomasks with circular features ranging from 100 to 900 μm in diameter (Figure 3-11a). Chips were filled with precursor, exposed, rinsed with PBS to remove un-crosslinked material, and imaged immediately to determine the dimensions of the freshly patterned structures. To remove any poorly crosslinked regions, chips were imaged again to determine the dimensions of the features after a 30-min incubation and rinse (“incubated”; Figure 3-11b). While circular free-standing features are very difficult to achieve on microfluidic chips with standard methods, they were straightforward to produce by on-chip photolithography.

As expected, all hydrogel features were linearly dependent on the dimensions defined by the photomasks (Figure 3-11b). Furthermore, features were obtained reproducibly down to 100 μm , the smallest size tested, for GelSH and for 70% DOF GelMA. In stiffer GelSH hydrogels ($G' > 1$ kPa, 10 mM NB), the feature dimensions obtained were highly accurate, matching those of the photomask with $< 10\%$ error for all feature sizes, except for 100 μm which had 16% error (Figure 3-11c). Features patterned

with lower storage moduli ($G' < 0.5$ kPa, 2.5 mM NB) were slightly larger than intended, but nevertheless also had $< 10\%$ error when larger than $100 \mu\text{m}$ (Figure 3-11c).

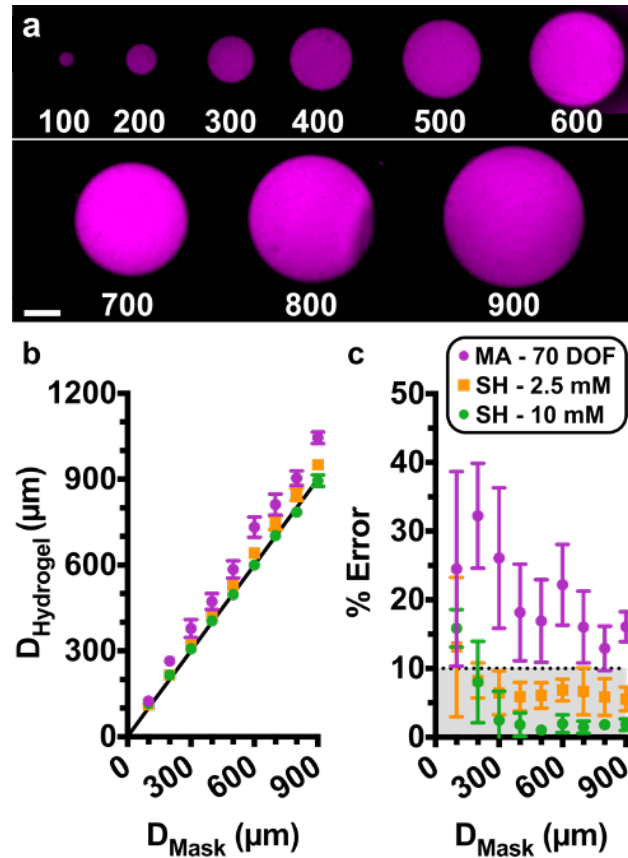


Figure 3-11 Assessing Pattern Resolution. (a) Fluorescent images of circular hydrogel features patterned on a microfluidic chip. Features ranged from 100-900 μm in diameter. Shown are features in GelSH with 2.5 mM NB, labelled with NHS-rhodamine, on a chip with a 0.15-mm coverslip. Scalebar 250 μm . (b-c) Quantification of accuracy. (b) Plot of measured diameter of the hydrogel region versus the diameter of the design on the photomask. Black line represents $y = x$, shown for reference. Measurements were taken after a 30-min incubation and rinse. (c) Calculated percent error of each feature versus the target diameter from the photomask design. The dotted line was drawn arbitrarily at 10% error, and grey area shows values that fall in that region. The shared legend shows 10% GelMA with 70% DOF ($n=3$) and 5% GelSH with norbornene concentrations of 2.5 mM ($n=4$) or 10 mM ($n=4$). Symbols and error bars represent mean and standard deviation; some error bars too small to see.

For both GelSH materials, there was no significant change in dimensions between freshly patterned and incubated features, suggesting all weakly cross-linked or uncrosslinked material was fully removed during the first rinsing step, and that no significant swelling took place during incubation (Figure 3-12). On the other hand, in stiffer GelMA hydrogels ($G' > 1$ kPa, 70% DOF), the hydrogel features were larger than the dimensions of the photomask by 13 – 32%. The larger features may be a result of the relatively long exposure time needed to generate the desired storage modulus, which may allow for diffusion of reaction species beyond the area illuminated by the photomask. Furthermore, the GelMA features grew significantly after incubation (Figure 3-12), suggesting significant levels of swelling. Features formed using soft GelMA ($G < 0.5$ kPa, 32% DOF) were observable after initial exposure but dissolved completely after a 30 min incubation period (not shown), making this formulation unsuitable for patterning. Therefore, the accuracy of patterning and initial feature stability was dependent not just on storage modulus, but also on the chemistry of gelation.

While the data above were collected using a glass coverslip (0.15 mm) for the bottom of the device, we also tested the extent to which resolution of features in GelSH was affected by the use of a thicker glass layer (1 mm), which is often preferred over coverslips to make more robust chips. Under this condition, while the diameter of the patterned features remained linearly dependent on the dimensions of the photomask, a small corona was formed around the patterns, resulting in larger dimensions (Figure 3-12c). The corona largely disappeared following incubation, indicating the formation of loosely cross-linked materials that later dissolved or were rinsed out. With the 1 mm glass, features were obtained reproducibly down to 200 μm in all tests; 100 μm features did not gel consistently. Therefore, while better resolution and pattern fidelity were obtained with

the 0.15 mm coverslip, the more robust chip may be an acceptable tradeoff for applications where larger features are sufficient.

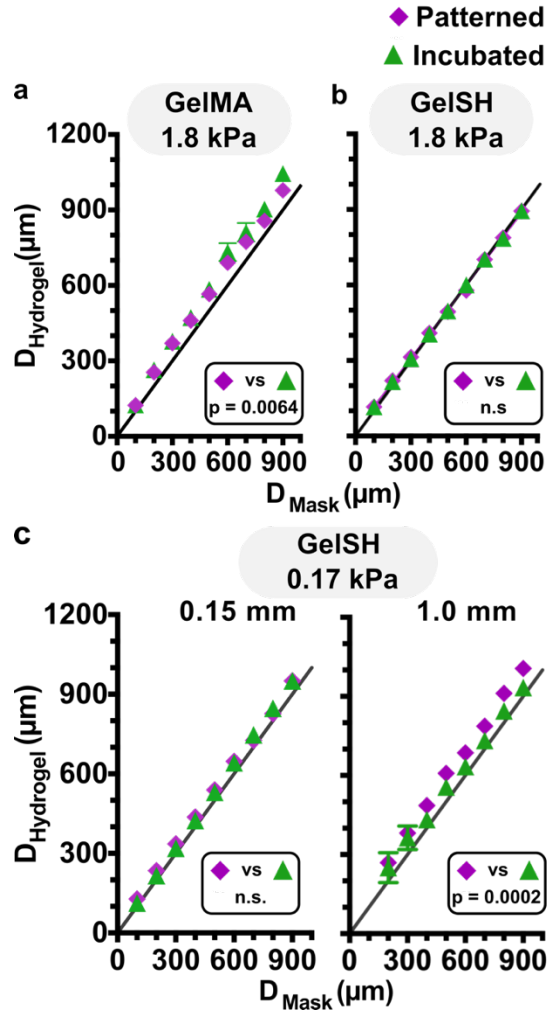


Figure 3-12 Assessing the stability of pattern resolution after incubation. (a-c) Quantification of accuracy between the diameter of the design on the photomask and the resulting diameter of the hydrogel region, measured either immediately after patterning (“patterned”) or after an additional 30-min incubation and rinse (“incubated”). Symbols and error bars represent mean and standard deviation; some error bars too small to see. Significance obtained by Paired T-test, n.s. indicates $p > 0.05$, in all panels. Black line represents $y = x$. (a) data for 1.8 kPa GelIMA hydrogel $n = 3$, $p = 0.0064$. (b) data for 1.8 kPa GelSH, $n = 4$, n.s. (c) data for 0.17 kPa GelSH, for microfluidic chips made with (left) a 0.15 mm coverslip, $n = 4$ chips, or (right) a 1 mm glass slide, $n = 3$ chips.

Finally, we tested the robustness of the patterning method to a change in light source. As expected and discussed in prior sections, reproducible gelation absolutely required the use of the collimated light source. Patterning with uncollimated light under the same conditions resulted in inconsistent gelation across chips, in some cases with regions left un-crosslinked, or with features that were weakly cross-linked but washed out after the 30-min incubation period. This phenomenon was consistent with the need for collimated light to provide uniform light intensity during photolithography in other settings, i.e., to mitigate light scattering, interference, and heterogenous dose across the exposed area.

35,36

3.4.11 Stability of features based on gelation chemistry

Having established the resolution and stability of patterned features under static conditions, we next assessed the mechanical stability of the patterned hydrogels under conditions mimicking those required for cell culture, i.e., under continuous perfusion overnight inside a humidified cell culture incubator (Table 3-4). GelSH hydrogels of higher storage modulus (10 mM NB) maintained 100% of the features that were 300 μm and larger, while smaller features, 200 and 100 μm , were stable in 75% and 50% of chips, respectively. For GelSH hydrogels of lower storage modulus (2.5 mM NB), we observed that features larger than 300 μm remained stable in majority of the chips patterned (75%), while features smaller than 300 μm were unstable in all chips. We speculate that the greater stability of larger GelSH features may be due to their higher contact area and thus more crosslinks to the PDMS and glass surfaces of the chip, or to their smaller surface/volume ratio that reduces exposure to shear flow in the chamber. In contrast to the relative stability of the GelSH features, even the stiffer GelMA hydrogels (70% DOF) proved unstable after overnight perfusion in features of all sizes. 32% DOF GelMA

hydrogels were not tested under these conditions, because features were not stable after a 30 min incubation period.

Table 3-4 Stability of patterned hydrogel after overnight perfusion. Reported values are % of successful attempts of features that remained anchored on the chip, as opposed to dissolved or rinsed away, after overnight perfusion. N=4 chips for all hydrogel formulations. (*) indicates not tested due to feature instability at short times.

Macromer	Formulation	Expected G' (kPa)	Feature Size (μm)						
			600	500	400	300	200	100	
5% GeISH	[NB]								
	10 mM	1	100%	100%	100%	100%	75%	50%	
	2.5 mM	0.1	75%	75%	75%	75%	0%	0%	
10% GeIMA	% DOF								
	70	1	0%	0%	0%	0%	0%	0%	
	32	0.1	*	*	*	*	*	*	

These data again revealed differences in feature stability as a function of both the storage modulus and the gelation chemistry. This may ultimately be a consequence of the cross-linking density of the network, with less dense networks being less mechanically stable. Indeed, for both chemistries, the micropatterned features were less stable in softer gels, which have fewer crosslinks than stiffer gels. Furthermore, under these conditions, micropatterned GeISH hydrogels proved to be more mechanically stable than micropatterned GeIMA hydrogels, regardless of storage modulus. We speculate that the instability of GeIMA features may be related to the short exposure times that were required to minimize cytotoxicity, which constrained the material to the linear stage the polymerization reaction, where cross-linking is incomplete (Figure 3-9). On the other hand,

the faster thiol-ene polymerization reached a saturated cross-linking density in this time period. We note that physical stability of patterned features also likely depends in part on the quality of the surface functionalization with reactive silane; indeed, we observed changes in overnight stability when a different plasma cleaner was used. In summary, the stability of micropatterned features under flow was a function of hydrogel formulation, storage modulus (likely as a proxy for degree of crosslinking), and the surface functionalization of the chip. Based on the high accuracy and stability observed in GelSH hydrogels, as well as published reports of biocompatibility,^{13,37} we utilized GelSH for all subsequent experiments.

3.4.12 NHS Rhodamine as a cell tracker

When setting up cell-laden hydrogel patterning experiments, it is often useful to stain cells prior to patterning in order to track their initial positions and/or ensure that your cells are equally dispersed throughout the hydrogels and obtain an initial “cell count.” NHS Rhodamine (5/6-carboxy-tetramethyl-rhodamine succinimidyl ester) is often used for bioconjugation with antibodies, or other proteins.³⁸ It is widely used due to its great overlap with RHODAMINE or TRITC filters and empirically, we found it useful with the photopatterning setup using a 405 nm light due to minimal bleaching. While it is often used as a general cell tracker, due to its specificity toward primary amines, we found it to preferentially stain live cells, with only ~60% of DAPI+ cells being double stained with NHS-Rhodamine (Figure 3-13). When used to account for a “total cell count,” it consistently underreported the total count.

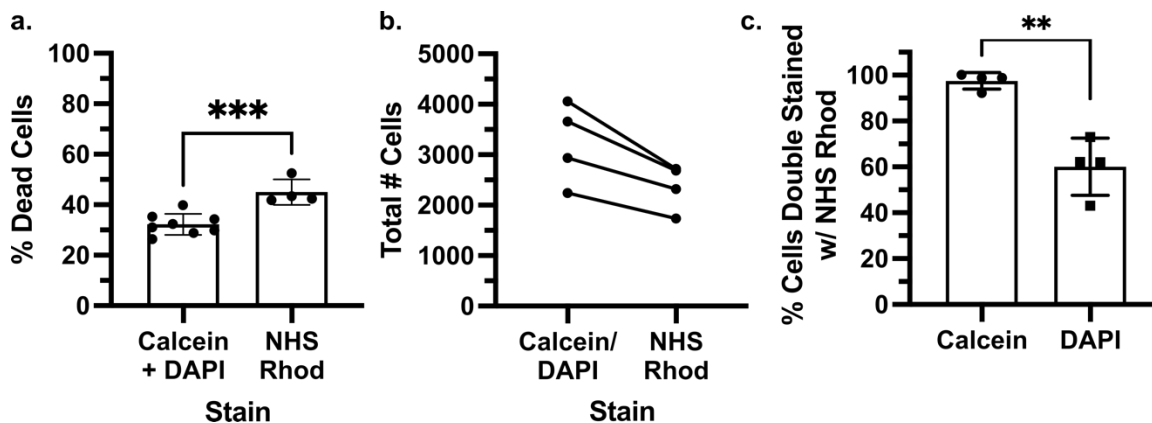


Figure 3-13 Characterization of staining specificity of NHS-Rhodamine on mixed splenocytes. Quantification of (a) Total dead cells with total cell count being a combination of Calcein (+) cells + DAPI (+) cells, or NHS Rhodamine (+) cells. (b) Actual # of total cell counts by Calcein (+) cells + DAPI (+) cells, or NHS Rhodamine (+) cells. (c) Percentage of cells double stain with NHS+Rhodamine and Calcein or DAPI.

Thus, while NHS-Rhodamine can be useful as a cell tracker for qualitative assessment, it is important to quantify the total cell population using a live/dead stain combination, such as Calcein-AM and Propidium Iodide, or Calcein-AM and DAPI (at the correct concentrations).

3.4.13 Minimization of non-specific cell adhesion via temperature

Embedding cells in a 3D matrix offers the advantage of seeding cells at higher densities than regular cell cultures due to additional space in the z dimension. In preliminary studies, when testing how many cells we could pack in our 3D cultures without inhibiting gelation, we observed an upper limit at to 25×10^6 cells/mL, where anything higher than that introduced irreproducibility to the patterning. One drawback of this high density was the potential of non-specific cell adhesion due to the high number of cells introduced in the chamber. This could create problems when in the future discrete and “clean” regions were to be patterned. To address these concerns first, we quantified the non-specific

adhesion to cells by quantifying the number of cells outside of the designated, patterned, areas. First, cell density was increased from 5, 10 and 25×10^6 cells/mL, followed by PBS to remove the un-crosslinked material. We observed a general trend of non-specific adhesion reduced as a function of cell density, with lower densities producing lower values of non-specific adhesion. However, even the lowest cell densities yielded a ~30% non-specific adhesion which was unacceptable for the micropatterning purpose (Figure 3-14a). The literature suggests that cells lose their ability to adhere when they are in environments below 8 °C³⁹ with integrin-mediated adhesion being disrupted with temperatures as high as 16 °C.⁴⁰ Based on this knowledge, we tested the rinsing efficiency as a function of cell density with a 4 °C PBS rinse. We observed a great decrease in the overall number of non-specific adhesion with, both 1 and 10×10^6 cells/mL samples, yielding less than 15% non-specific adhesion (Figure 3-14b). We decided to maintain the cell density at 10×10^6 cells, which is commonly used in the field and still an order of magnitude greater than those commonly used in 2D cultures.

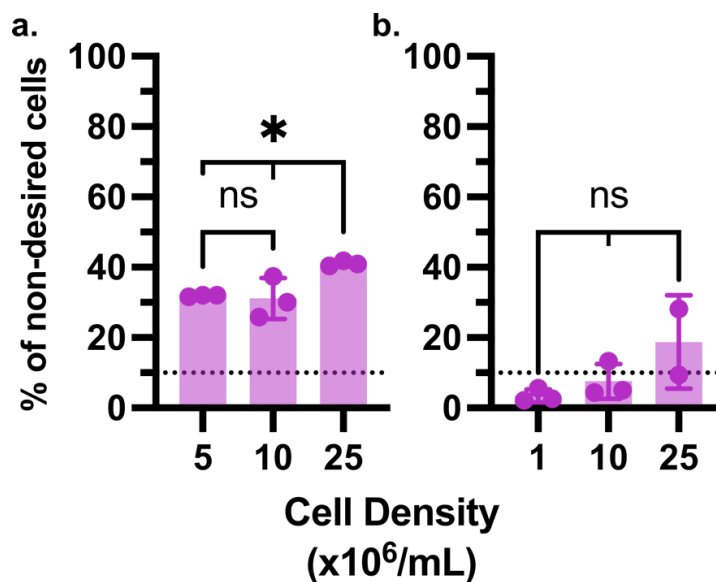


Figure 3-14 Rinsing optimization after micropatterning as a function of cell density with a) RT rinse (* $p < 0.05$, One-way ANOVA with Tukey's multiple comparisons) and b) 4°C rinse ($p > 0.05$, One-way ANOVA with Tukey's multiple comparisons).

3.4.14 Viability of murine splenocytes based on gel chemistry

In the initial stages of the project, the access to lymphocytes was limited to those isolated from murine spleens. Thus, initial short-term assessment of viability was done on primary murine splenocytes. Splenocytes were resuspended in hydrogel precursor, either GelNB/PEGSH or GelMA, loaded into the microfluidic chip, exposed, rinsed and chips were connected to media perfusion for 1 hour, in an incubator. After this culture period, media was removed with a PBS rinse and a live/dead stain was flowed in. The results showed that splenocytes cultured in GelNB had better viability than those in GelMA, agreeing with published literature. More specifically, splenocytes in GelNB hydrogel retained viability within 15% of that from fresh, unexposed cells (Figure 3-15a) while splenocytes cultured in GelNB retained viability within ~30% of that of fresh, never exposed cells an hour after patterning (Figure 3-15b).

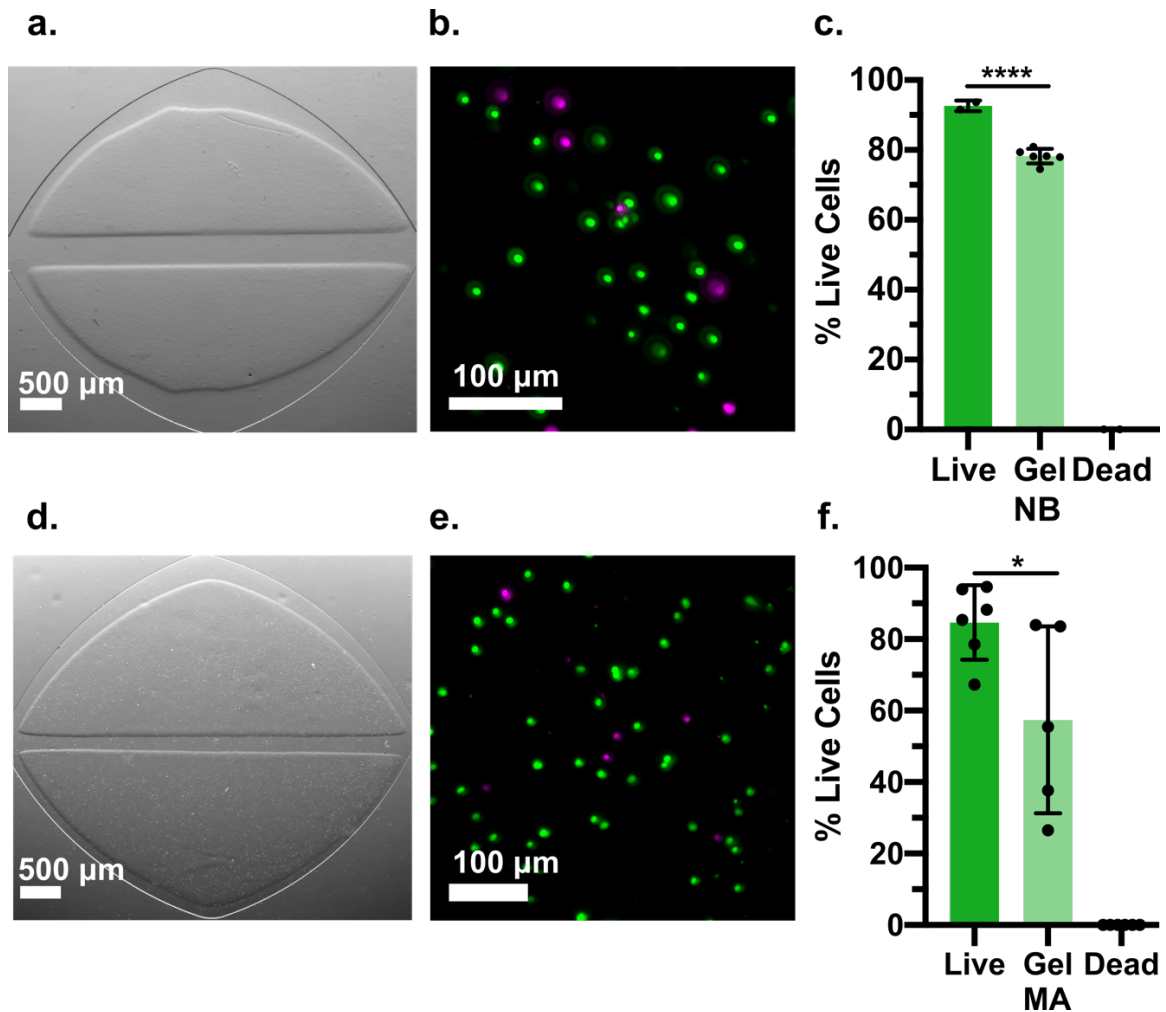


Figure 3-15 Viability of mixed splenocytes after patterning in GelNB, and GelMA. a) Brightfield and b) fluorescence image of splenocytes within GelNB hydrogel, 1 hour after patterning. Cells labelled with Calcein-AM (green) and PI (magenta). c) Quantification of viability 1 hr after patterning. ($p < 0.0001$, One-way ANOVA with Tukey's multiple comparisons). d) Brightfield and e) fluorescence Image of splenocytes within GelMA hydrogel, 1 hour after patterning. Cells labelled with Calcein-AM and PI. f) Quantification of viability 1 hr after patterning. Splenocytes retained viability within ~30% of that of fresh, never exposed cells an hour after patterning. (* $p < 0.05$, One-way ANOVA with Tukey's multiple comparisons).

3.4.15 Accessing biomimetic structures via patterning

Based on the data resulting from stability and initial viability experiments, we decided to keep working only with the thiol-norbornene hydrogel system. We tested the extent to which on-chip photolithography provided access to micropatterned hydrogel geometries at increasing levels of complexity. These experiments were intended to test the patterning system's ability to generate biomimetic features of interest in future organ-on-chip, rather than to test particular biological functions. First, we tested the ability to pattern open channels and a curved fluidic path (Figure 3-16a), which will be critical for future use in patterning vascularized systems or multiple stand-alone culture regions. By preventing exposure of the precursor solution in the center and near the walls of the chamber, we were able to pattern two self-standing lobes divided by an open, central channel through which fluid could flow. Next, we tested geometries that are challenging to achieve by standard microfluidic patterning methods. It was straightforward to pattern regions with shared, non-linear boundaries, e.g., by creating a self-standing island followed by a second surrounding hydrogel (Figure 3-16b). The two regions were visually in contact under microscopic imaging, without a gap. We extended this system to pattern three sequential regions in concentric circles (Figure 3-16c). Nonlinear adjacent regions will be useful in the future for cellular invasion assays, angiogenesis assays, and patterning of biomimetic tissue structures for organ-on-chip applications. Finally, to test the versatility with more intricate geometries and alignment capabilities, we recreated the University of Virginia (UVA) historic Rotunda by patterning hydrogels in three sequential steps: 1) the columns, 2) the negative space surrounding the columns, and 3) the dome and foundation (Figure 3-16d).

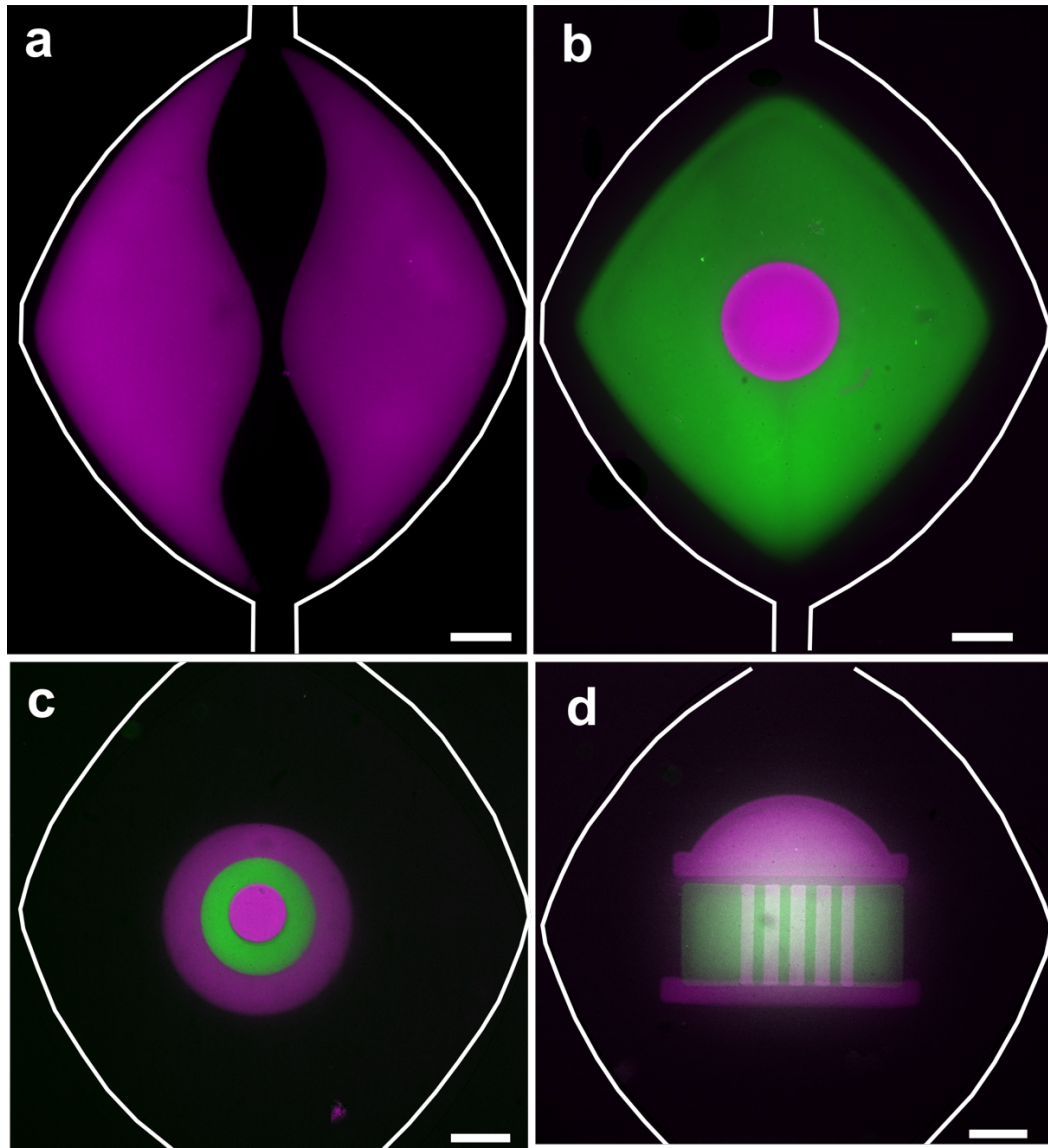


Figure 3-16 Geometric versatility achieved by on-chip photo-patterning of GelSH hydrogels. (a) NHS-rhodamine-labelled hydrogel (magenta) used to pattern a curved fluidic path in culture chamber. (b) A central circular island (magenta) surrounded by NHS-fluorescein-labelled GelSH (green). (c) Concentric circles patterned with hydrogel labelled with NHS-rhodamine and NHS-fluorescein in three sequential steps. (d) A patterned UVA Rotunda in three sequential steps. The corresponding photomasks used to achieve patterns are shown above each panel. All scalebars are 500 μm .

In all cases, the second and subsequent patterns were achieved through the use of photomasks that covered the previously patterned constructs, ensuring that each region only received one dose of light. We note that these experiments used the same parent microfluidic chamber for all designs; only the photomasks were changed. Thus, the spatial organization of the patterned gel was altered rapidly between subsequent devices, without time-consuming master fabrication.

3.4.16 Cell-laden features on-chip

Next, we tested the ability to pattern cell-laden features in targeted locations on chip. Primary naïve human T cells (CD4+) were used as a rigorous case study; these non-proliferative cells are of interest for organ-on-chip models of immunity and testing of immunotherapies.^{41,42} The T cells were suspended in the precursor solution immediately before loading it onto the chip for patterning. As with the cell-free patterns, the cell-laden un-crosslinked hydrogel-precursor was readily washed out from designated regions in the center and edges of the chamber, to generate open channels (Figure 3-17a,b). Next, we tested the ability to pattern complex, cell-laden geometries with a lobular organ pattern inspired by a stylized facial pattern. The central lobes were patterned first, followed by the surrounding parenchyma-like space (Figure 3-17c,d). The resulting features were composed of two separate cell populations that shared non-linear boundaries with one another. This arrangement demonstrates the ability to recapitulate complex tissue architectures, where one or more cell types are organized into distinct substructures that are in contact with one another. These geometries would be challenging to obtain on-chip by laminar flow or by surface-tension, even with the inclusion of micropillars.

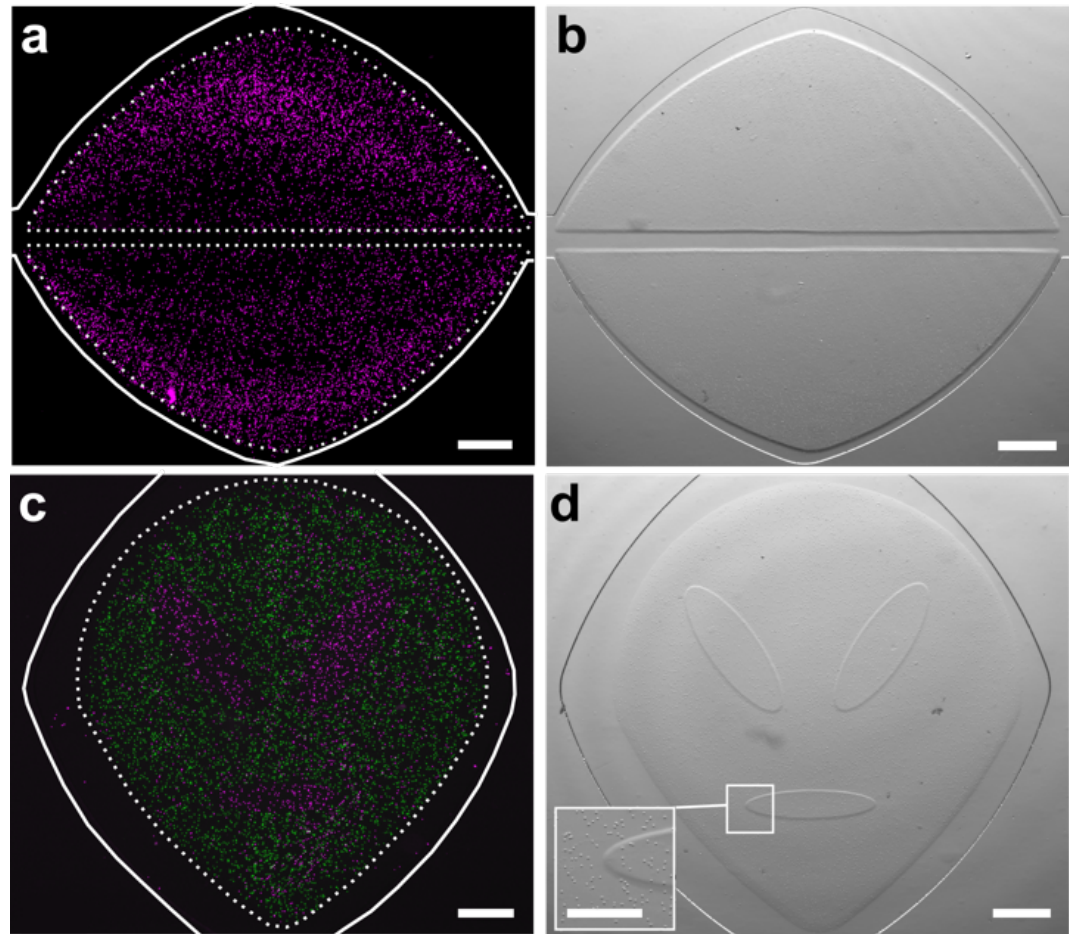


Figure 3-17 In situ photo-patterned cell-laden hydrogel constructs. (a) Fluorescence and (b) brightfield images of a patterned 3D cell culture (cells labelled magenta), patterned into two self-standing lobes. A linear fluidic path was patterned between them, and a second, curved fluidic path surrounded them for better distribution of media. (c) Fluorescence and (d) brightfield images of two distinct cell populations patterned into a lobular organ geometry. First cell population labelled with NHS-rhodamine (magenta); second population labelled with CFSE (green). Inset shows magnified boundary between two patterned regions. Scale bar is 500 μm in (a-d), 250 μm in inset. Dashed lines denote the boundary of the hydrogel regions; solid white lines indicate the edges of the microfluidic culture chamber.

It is important to note that while there is great flexibility to the types of geometries that can be achieved with this method, one is limited by the requirement to rinse out uncrosslinked materials. In particular, concave structures and shapes with voids, such as the letters A and O, are not directly accessible, but multi-step patterning offers a potential solution to this issue. For example, to pattern a cell-laden ring around a cell-free center, the inner region would be patterned first using gel without cells, followed by the surrounding ring.

3.4.17 Precise patterning of CD4 T cells in GelSH microarray on chip

Next, we investigated the spatial precision of cellular patterning and whether it was dependent on hydrogel formulation. During the loading of the chip, the cell-laden hydrogel-precursor fills the entire culture chamber, giving cells an opportunity to non-specifically adhere to the surfaces of the chip outside the intended patterned regions. To rigorously quantify the specificity of cell location in the patterns, we created an array of 9 circular features per chip in diameters of 200, 400, and 600 μm . These dimensions are representative of the length scale of tissue substructures in complex organs like brain, lymph nodes, and solid tumors.^{43,44} Cells were patterned at high density ($> 10^7$ cells/mL) in GelSH hydrogels with 2.5- or 10-mM NB linker (Figure 3-18a), and incubated under continuous fluid flow overnight. As expected, the mean density per unit area in the patterned regions was high (Error! Reference source not found.b), and feature size had no effect on cell density (data not shown). Non-specific adhesion was minimal outside of patterned hydrogels, as the cell density in the non-exposed regions was less than 4.5% of that in the patterned areas (Figure 3-18b).

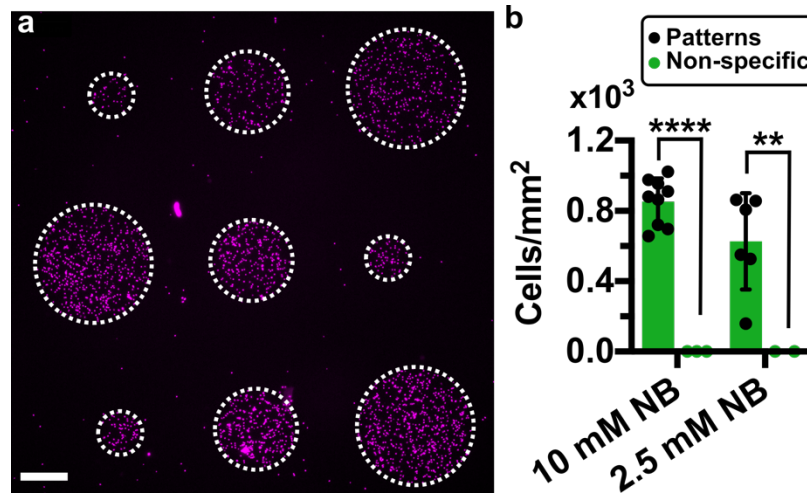


Figure 3-18 Precision of photo-patterned microarray of human CD4 T cells on chip. (a) Nine-circle culture array patterned on-chip with cells pre-labelled with NHS-rhodamine. Scalebar 250 μm . (b) Quantification of cell density inside and outside of the patterned regions in GelSH hydrogels (n=2 and n=3 chips respectively). Two-way ANOVA with Sidak's multiple comparisons; **** $p \leq 0.0001$, ** $p \leq 0.01$.

The high efficiency of targeted patterning may be the result of the rapid precursor loading and short exposure times, which allowed for the rinsing step to start less than one minute after cells enter the chamber. Thus, cells were patterned precisely in the intended regions, with minimal adhesion elsewhere.

3.4.18 Overnight culture of patterned human lymphocytes

In initial experiments where overnight viability of primary human cells was being tested, the geometry of the patterned cultures was designed to maximize the number of cells that could be seeded in a given chip. For this purpose, we designed two self-standing lobes of 4.7 mm in length and 1.5 mm at the widest point, separated by a 400 μm channel through which media would be delivered (Figure 3-19a). After 18 hours of culture, cells exhibited similar viability to off-chip live controls in the "outer" regions of the hydrogel pattern, i.e. closer to fluid flow, and diminished viability in "inner" regions (Figure 3-19b,c).

We hypothesized that O₂ diffusion is limiting in regions further from fluid flow, reducing cell survival. To test this hypothesis, we designed a microarray of 9 circular features per chip in diameters of 200, 400, and 600 μm (Figure 3-19d) based on the critical distances established in literature for O₂ diffusion in 3D cultures.⁴⁵

The micropatterned GelSH-based culture arrays were cultured overnight to test the initial effects of patterning and pattern geometry on overnight survival of these fragile primary cells. Cultures were held under continuous flow of media to ensure replenishment of nutrients and oxygen in the microfluidic chip. Using the microfluidic culture system, it was straightforward to deliver staining reagents at the end of the experiment to measure viability in situ by flowing in a Calcein-AM/DAPI (live/dead) solution, incubating, rinsing, and imaging (Figure 3-19e). In 10 mM NB hydrogels, there was no significant difference in the percentage of live cells between on-chip cultures and off-chip unpatterned controls (Figure 3-19f) nor between the feature dimensions. Interestingly, viability was slightly reduced in the 2.5 mM NB hydrogels compared to off chip controls (20% decrease, $p=0.0089$, One-way ANOVA with Tukey's multiple comparisons), though still in an acceptable range. As the focus of this work was on the development of the micropatterning method, we did not further explore the impact of gel chemistry and the internal structure of the hydrogel on longer term cell viability and behavior; these will be exciting areas for future investigation.⁴⁶⁻⁴⁹

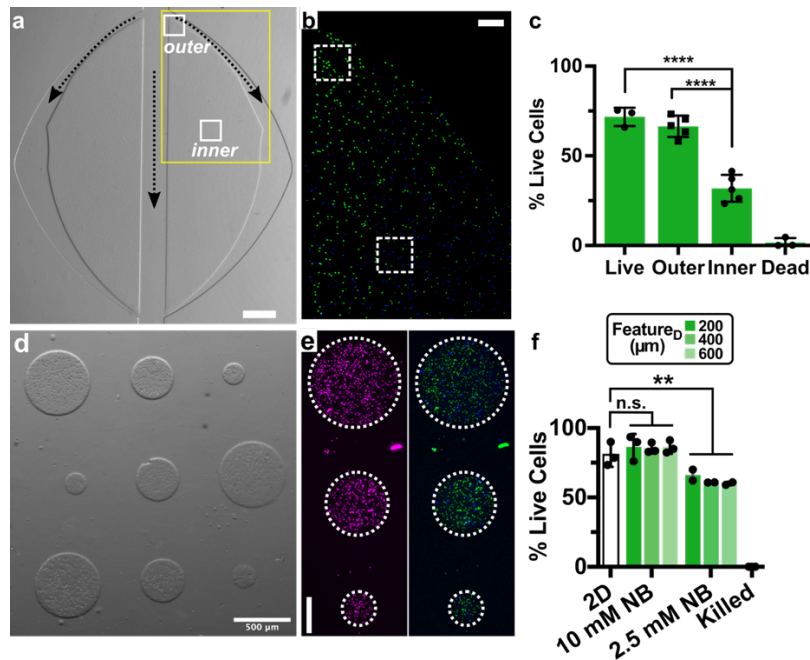


Figure 3-19 Overnight viability of CD4 T cells in patterned cultures. (a) Photo-patterned 3D cultures on chip. White boxes denote “outer” and “inner” areas. Dashed lines represent fluid flow pathways. Scalebar 500 μm . (b) Zoomed-in representative image of yellow outlined-region shown in 1a. Fluorescent image of patterned 3D culture, stained with live (green-Calcein AM) / dead (blue-DAPI) stain after 18 hours of culture under fluid flow. Scalebar 200 μm . (c) Quantification of viability 18 hrs post-patterning. No significant difference was observed between live control and “outer regions.” One-way ANOVA, $n=5$. (d) Nine-circle culture array patterned on-chip. Scalebar 250 μm . (e) Zoomed-in view of 3D culture row from panel d. (Left) Image of NHS-rhodamine labelled cells; (Right) image after viability staining with Calcein-AM (green) and DAPI (blue). Scalebar 250 μm . (f) Quantification of the viability of patterned CD4+ T cells in 5% GelSH with 2.5 and 10 mM NB hydrogels as a function of feature dimensions after overnight culture under continuous fluid flow, versus off-chip (2D) controls (n.s. $p > 0.05$, ** $p \leq 0.01$ One-way ANOVA with Tukey’s multiple comparisons, $n=3$ and $n=2$ for 10 mM and 2.5 mM NB chips, respectively).

These experiments confirm that the on-chip photopatterning method was cytocompatible and ready for future implementation to study the impact of spatial organization on cell function, including with primary cells.

3.4.19 Long term culture conditions: bubbles

3.4.19.1 Formation of bubbles during culture

The formation of undesired bubbles inside a microfluidic chip is ubiquitous in the field. However, the tricks or ways that researchers combat air bubbles often do not make it to published articles or are buried within other experimental details. Consistent and unavoidable formation of bubbles can cause many issues on an experiment, including destabilizing or hindering flow, and damage fragile microstructures (like patterned 3D cultures) and cells. This section will cover tricks I have found useful and have enabled performance of overnight culture experiments under constant perfusion without significant loss of samples/replicates to undesired abundance of air bubbles.

3.4.19.2 What causes bubbles?

Liquids in equilibrium with a contacting gas phase contain molecules of this gas in its bulk volume. Thus, common reagents, like buffers or media, used in cell culture will contain a certain concentration (c) of air molecules (mostly N_2 and O_2). The equilibrium concentration of these gas particles (c_s) in the liquid solution (mass or mols of gas per volume of liquid) is given by Henry's law:

Equation 3-3

$$c_s = H(T)p_g$$

Where where p_g is the pressure of the gas in the vapor phase and $H(T)$ is Henry's law solubility constant, different for every gas species and lower with increasing temperature, primarily. When in equilibrium ($c = c_s$), the liquid is said to be in the saturated

state.²⁴ Dynamic changes in pressure or temperature lead to variations in c_s that can result in the solubility c being higher or lower than c_s until the diffusion of gases from/to the gas phase re-equilibrates the system.

In microfluidic culture experiments, both pressure differences and temperature shifts can be introduced given the nature of the experimental set-up. For example, media will experience pressure changes as it travels from a reservoir, often stored in closed conical tubes which are connected to microfluidic tubing, and finally enter the chip. Specifically, with the photopatterning set-up discussed earlier in this chapter, all steps are performed in a biosafety cabinet, which is at room temperature, but the culture takes place inside an incubator, creating temperature shifts.

3.4.19.3 *Bubble traps*

One of the main sources of bubbles during culture experiments is the media. Cell culture media is often stored at 4°C, and people unfamiliar with the perils of bubbles in microfluidics may not think twice about using media straight from the fridge to culture cells at 37°C. However, this increase in temperature, as discussed above, will lead to dissolved O₂ to be “degassed” creating bubbles that while small, can be detrimental once they enter the microfluidic chip. One way to remedy this effect is to pre-equilibrate the cell culture media inside the incubator. We found this method led to a great decrease in bubble formation when it was performed at least 12 hours in advance. However, bubbles from media can come from additional sources, such as added surfactants or proteins. For example, bovine serum albumin (BSA) is routinely used in media formulations as a carrier protein⁵⁰, which prevents adhesion of proteins to the microfluidic tubing, but it is also characteristic of increasing the “foamability” of media.²⁴ In order to remove bubbles arising from a media reservoir, PDMS bubble traps were fabricated in-house, and connected to

the LN chips in a daisy-chain like manner (Figure 3-20), inspired by a published design by Jiang et al.²¹

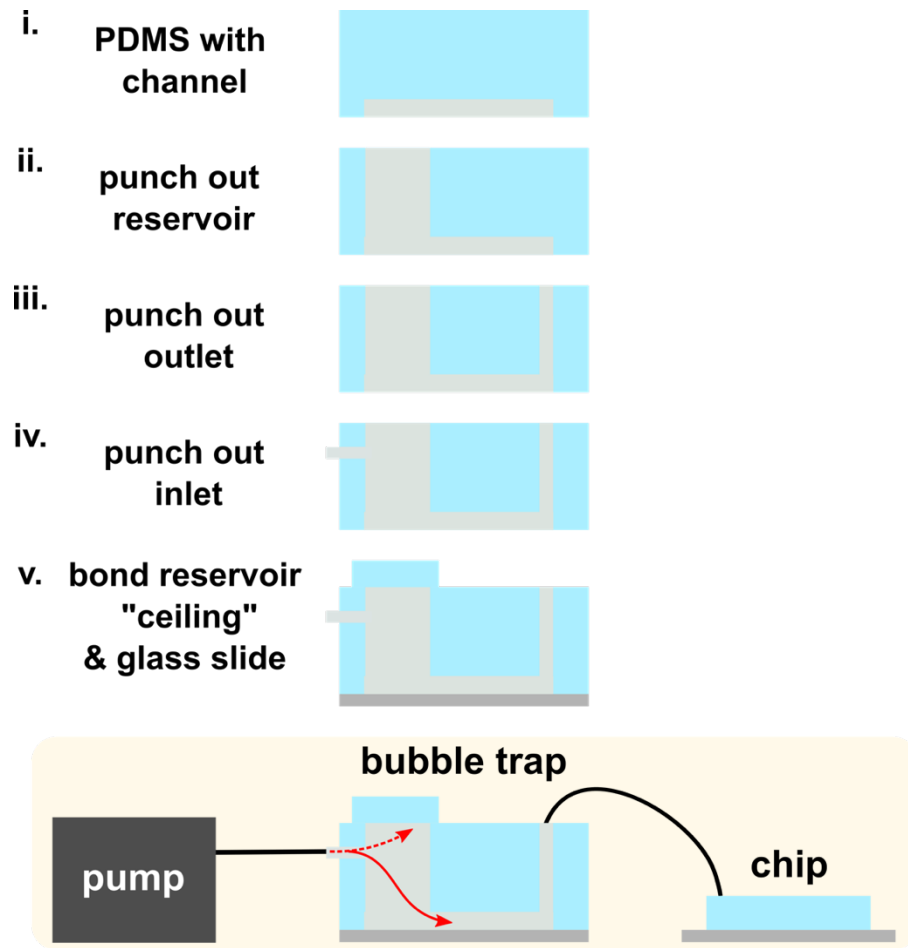


Figure 3-20 PDMS bubble trap fabrication and final connections to pump and chips. Channels (light grey), PDMS (aqua) and coverslip (dark grey), arrows (red) show path for bubbles (dashed) and bubble-free fluid.

The bubble traps are connected directly to the tubing driving the flow, which intersects in a perpendicular manner the gas reservoir. Once a bubble arrives, through the principle of buoyancy, it will rise towards the roof of the reservoir while bubble free media will be driven through the channel and can be connected through additional tubing to the final microfluidic device.

3.4.19.4 Other considerations to avoid bubbles

Besides reducing the propensity of bubbles emerging from a reservoir of media, it is important to remember that many devices, like the aforementioned bubble traps and the LN chip, are made of PDMS. This choice in material is often advantageous given its inherent gas permeability which acts (in addition to cell culture media) as another source of O₂ replenishment for cells. However, O₂ dissolved inside of the PDMS at room temperature, could also expand and enter the culture chamber during incubation. It is critical to be aware of any gas permeable component in the experimental set-up and take proactive action to equilibrate prior to an experiment run. This includes: microfluidic devices, peristaltic or other microfluidic tubing, connectors and adapters. Equilibration can be achieved through active degassing (vacuum) or storing components at higher temperatures than one would need for cell culture settings.

3.4.20 Permeability of hydrogels as a proxy to mesh density

One key function of lymphocytes, T cells in particular, is their ability to migrate. However, when closely analyzing data collected in prior experiments, we noticed the arrangement of cells did not seem to vary after the culture periods. This was unexpected, since migration (at least non-directional) was expected even in the absence of a chemoattractant. One hypothesis was that the hydrogel meshwork may have been too densely packed. This had been an advantage previously, allowing generation of stable microstructures under fluid flow, but perhaps it was too packed to allow for cell migration. Since the set-up to visualize the actual pore size and interconnectivity of the matrix required extensive training, we decided to measure the hydrogels permeability and use it as a proxy for mesh density. Our hypothesis was that densely cross-linked gels would have a lower permeability and that by varying the composition of the hydrogel precursor

a combination that was densely-packed enough to produce mechanically stable gels but loose-enough to allow migration could be identified.

To measure permeability, we utilized a modified Boyden chamber set-up, which are normally used to study cell migration and are made up of a hollow plastic insert divided into two sides by a permeable membrane.⁵¹ In this set-up, a cell suspension or 3D culture can be set-up on the top side of the membrane and signaling molecules can be placed in media on the down side of the membrane, influencing movement downstream. This set-up can be modified (Figure 3-21a) by introducing the hydrogel of interest onto the top side of the membrane and inducing a pressure-driven flow that can be correlated in to the permeability of the biomaterials through the use of the hydraulic permeability equation (details in the Methods). Hystem-C is a thermally gelled hydrogel comprised of thiolated hyaluronic acid, thiolated gelatin and PEG-diacrylate (PEGDA), was selected as a positive control given its known permeable nature. The formulation, and wavelength used for crosslinking, of GelSH/PEGNB hydrogels was varied as described on Table 3-5 and permeability assessed. Results are shown in Figure 3-21b, in short, a significant decrease ~ 1 order of magnitude was observed between all GelSH/PEGNB conditions and Hystem-C. While we do expect pore size to vary based on precursor formulation, this did not seem to impact permeability in a significant way. Next steps will focus on imaging the internal structure of hydrogels, through SEM or confocal microscopy, to have a better idea of porosity and how this may impact mesh density, stability, and cell migration.

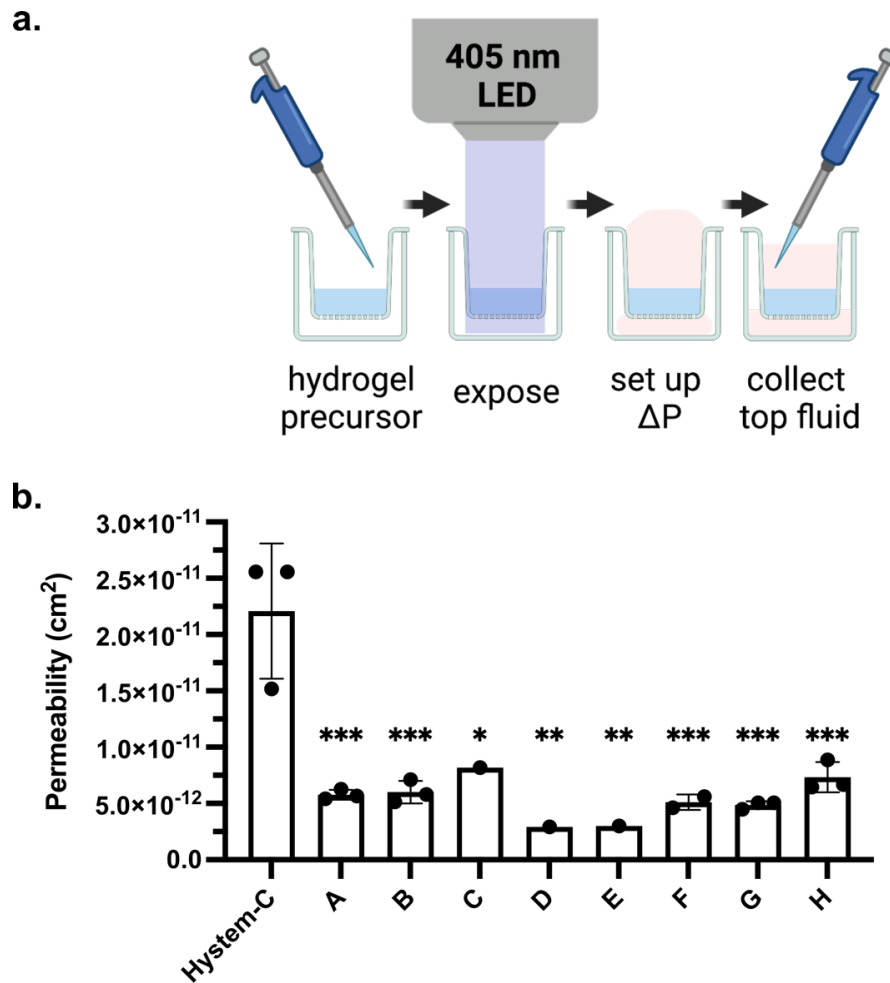


Figure 3-21 Assessing permeability of hydrogels (a) Assay set-up. (b) Measured permeability of various formulations of hydrogels. * $p \leq 0.05$, ** $p \leq 0.01$, *** $p \leq 0.005$ via One-way ANOVA with Tukey's multiple comparisons, all statistical comparisons are between that sample and Hystem-C, all other comparisons were n.s. > 0.05 .

Based on literature, we know pore size can often be controlled by the concentration and length of linkers, although most studies are based on PEG-based hydrogels.^{52,53} Given that this hydrogel's main component is GelSH, with an expected size of ~ 200 kDa, we expect it to be the main contributor to the mesh's architecture. Optimization of mesh crosslinking density may be a combination of very low concentrations of GelSH and long

PEG-NB linkers. Additional parameters to test include modulation of light intensity and photoinitiator concentration.

Table 3-5 Formulations for GelSH hydrogels tested for permeability. Except where noted [SH] was based on contribution from GelSH and [NB] contribution was based on 8-arm PEG-NB 20 kDa.

Legend Name	GelSH (w/v)	[SH] mM	[NB] mM	Linker Used	[LAP] mM	Wavelength (nm)
A	5	11.2	10	3.4	3.4	405
B	5	11.2	10	3.4	3.4	405
C	2	4.66	4.66	3.4	3.4	405
D	3	6.99	6.99	3.4	3.4	405
E	4	9.32	9.32	3.4	3.4	405
F*	0	10	10	1.7	1.7	405
G	5	11.2	10	1.7	1.7	385
H	2.5	11.2	5.58	1.7	1.7	385

*No GelSH was used in this formulation and [SH] contribution was based on 4-arm PEG-SH 5 kDa and [NB] from 4-arm PEG-NB 10 kDa.

3.5 Conclusion

In summary, we have described a protocol for in situ micropatterning of spatially organized biomaterials and 3D cell cultures on a microfluidic chip and established the impact of crosslinking chemistry on the storage modulus, stability, and spatial resolution of the patterns. By simply aligning a photomask prior to light exposure, the user may pattern a wide variety of design configurations in the xy-plane without altering the microfluidic housing. The resulting patterned cultures were modular and free-standing, without the need for physical supports such as micropillars to guide the hydrogel in place. Gelation chemistry had a significant impact on the accuracy and mechanical stability of patterned microfeatures. While features were patterned down to 100 μm in both GelSH

and GelMA hydrogels, the GelSH hydrogels in stiffer formulations provided the highest accuracy and greater stability under fluid flow. Complex geometries such as concentric circles, architectural designs, and microarrays were all accessible, as were open flow paths to distribute media to the patterned 3D cultures. When used with thiol-ene polymerization chemistry, the micropatterning method had high specificity and low cytotoxicity with primary human cells. We envision that this micropatterning strategy will enable researchers to organize 3D cultures directly onto organs-on-chip in arrangements that capture the complexity of tissue organization, thus granting access to mechanistic experiments while maintaining control over cellular and fluidic components.

3.6 References

1. Rajan, S. A. P., Skardal, A. & Hall, A. R. Multi-Domain Photopatterned 3D Tumor Constructs in a Micro-Physiological System for Analysis, Quantification, and Isolation of Infiltrating Cells. *Adv. Biosyst.* **4**, e1900273 (2020).
2. Takeuchi, M. *et al.* On-Chip Fabrication of Cell-Attached Microstructures using Photo-Cross-Linkable Biodegradable Hydrogel. *J. Funct. Biomater.* **11**, (2020).
3. Sato, K. *et al.* Patterned Co-culture of Live Cells on a Microchip by Photocrosslinking with Benzophenone. *Anal. Sci.* **32**, 113–116 (2016).
4. Zhu, M. *et al.* Gelatin methacryloyl and its hydrogels with an exceptional degree of controllability and batch-to-batch consistency. *Sci. Rep.* **9**, 6863 (2019).
5. Skardal, A., Devarasetty, M., Soker, S. & Hall, A. R. In situ patterned micro 3D liver constructs for parallel toxicology testing in a fluidic device. *Biofabrication* **7**, 031001 (2015).

6. Aung, A., Kumar, V., Theprungsirikul, J., Davey, S. K. & Varghese, S. An Engineered Tumor-on-a-Chip Device with Breast Cancer–Immune Cell Interactions for Assessing T-cell Recruitment. *Cancer Res.* **80**, 263–275 (2020).
7. LeValley, P. J. *et al.* Fabrication of Functional Biomaterial Microstructures by in Situ Photopolymerization and Photodegradation. *ACS Biomater. Sci. Eng.* **4**, 3078–3087 (2018).
8. Fairbanks, B. D., Schwartz, M. P., Bowman, C. N. & Anseth, K. S. Photoinitiated polymerization of PEG-diacrylate with lithium phenyl-2,4,6-trimethylbenzoylphosphinate: polymerization rate and cytocompatibility. *Biomaterials* **30**, 6702–6707 (2009).
9. Loessner, D. *et al.* Functionalization, preparation and use of cell-laden gelatin methacryloyl–based hydrogels as modular tissue culture platforms. *Nat. Protoc.* **11**, 727–746 (2016).
10. McCall, J. D. & Anseth, K. S. Thiol–Ene Photopolymerizations Provide a Facile Method To Encapsulate Proteins and Maintain Their Bioactivity. *Biomacromolecules* **13**, 2410–2417 (2012).
11. Lin, C.-C., Ki, C. S. & Shih, H. Thiol-norbornene photo-click hydrogels for tissue engineering applications. *J. Appl. Polym. Sci.* **132**, (2015).
12. Lim, K. S. *et al.* New Visible-Light Photoinitiating System for Improved Print Fidelity in Gelatin-Based Bioinks. *ACS Biomater. Sci. Eng.* **2**, 1752–1762 (2016).
13. Muñoz, Z., Shih, H. & Lin, C.-C. Gelatin hydrogels formed by orthogonal thiol–norbornene photochemistry for cell encapsulation. *Biomater. Sci.* **2**, 1063–1072 (2014).
14. Yue, K. *et al.* Synthesis, properties, and biomedical applications of gelatin methacryloyl (GelMA) hydrogels. *Biomaterials* **73**, 254–271 (2015).
15. Van Hoorick, J. *et al.* (Photo-)crosslinkable gelatin derivatives for biofabrication applications. *Acta Biomater.* **97**, 46–73 (2019).

16. Belanger, M. C., Anbaei, P., Dunn, A. F., Kinman, A. W. L. & Pompano, R. R. Spatially Resolved Analytical Chemistry in Intact, Living Tissues. *Anal. Chem.* **92**, 15255–15262 (2020).
17. Zatorski, J. M., Montalbino, A. N., Ortiz-Cárdenas, J. E. & Pompano, R. R. Quantification of fractional and absolute functionalization of gelatin hydrogels by optimized ninhydrin assay and ¹H NMR. *Anal. Bioanal. Chem.* **412**, 6211–6220 (2020).
18. Haubert, K., Drier, T. & Beebe, D. PDMS bonding by means of a portable, low-cost corona system. *Lab. Chip* **6**, 1548–1549 (2006).
19. Kepp, O., Galluzzi, L., Lipinski, M., Yuan, J. & Kroemer, G. Cell death assays for drug discovery. *Nat. Rev. Drug Discov.* **10**, 221–237 (2011).
20. Gillissen, M. A. *et al.* The modified FACS calcein AM retention assay: A high throughput flow cytometer based method to measure cytotoxicity. *J. Immunol. Methods* **434**, 16–23 (2016).
21. Zheng, W., Wang, Z., Zhang, W. & Jiang, X. A simple PDMS-based microfluidic channel design that removes bubbles for long-term on-chip culture of mammalian cells. *Lab. Chip* **10**, 2906–2910 (2010).
22. Jafarnejad, M., Zawieja, D. C., Brook, B. S., Nibbs, R. J. B. & Moore, J. E. A Novel Computational Model Predicts Key Regulators of Chemokine Gradient Formation in Lymph Nodes and Site-Specific Roles for CCL19 and ACKR4. *J. Immunol.* **199**, 2291–2304 (2017).
23. Vowell, S. *Microfluidics: The Effects of Surface Tension.* (2009).
24. Pereiro, I., Khartchenko, A. F., Petrini, L. & Kaigala, G. V. Nip the bubble in the bud: a guide to avoid gas nucleation in microfluidics. *Lab. Chip* **19**, 2296–2314 (2019).
25. Regehr, K. J. *et al.* Biological implications of polydimethylsiloxane-based microfluidic cell culture. *Lab. Chip* **9**, 2132–2139 (2009).

26. Bowden, N., Huck, W. T. S., Paul, K. E. & Whitesides, G. M. The controlled formation of ordered, sinusoidal structures by plasma oxidation of an elastomeric polymer. *Appl. Phys. Lett.* **75**, 2557–2559 (1999).
27. Price, R. B. T., Ehrnford, L., Andreou, P. & Felix, C. A. Comparison of quartz-tungsten-halogen, light-emitting diode, and plasma arc curing lights. *J. Adhes. Dent.* **5**, 193–207 (2003).
28. Mills, R. W., Uhl, A., Blackwell, G. B. & Jandt, K. D. High power light emitting diode (LED) arrays versus halogen light polymerization of oral biomaterials: Barcol hardness, compressive strength and radiometric properties. *Biomaterials* **23**, 2955–2963 (2002).
29. Vu, N. H., Pham, T. T. & Shin, S. LED Uniform Illumination Using Double Linear Fresnel Lenses for Energy Saving. *Energies* **10**, 2091 (2017).
30. Pynaert, R., Buguet, J., Croutxé-Barghorn, C., Moireau, P. & Allonas, X. Effect of reactive oxygen species on the kinetics of free radical photopolymerization. *Polym. Chem.* **4**, 2475–2479 (2013).
31. Murphy, M. C. *et al.* Measuring the Characteristic Topography of Brain Stiffness with Magnetic Resonance Elastography. *PLOS ONE* **8**, e81668 (2013).
32. de la Zerda, A., Kratochvil, M. J., Suhar, N. A. & Heilshorn, S. C. Review: Bioengineering strategies to probe T cell mechanobiology. *APL Bioeng.* **2**, 021501 (2018).
33. Purwada, A. *et al.* Ex vivo engineered immune organoids for controlled germinal center reactions. *Biomaterials* **63**, 24–34 (2015).
34. Anseth, K. S. *et al.* In situ forming degradable networks and their application in tissue engineering and drug delivery. *J. Controlled Release* **78**, 199–209 (2002).
35. Lee, J. B., Choi, K.-H. & Yoo, K. Innovative SU-8 Lithography Techniques and Their Applications. *Micromachines* **6**, 1–18 (2015).

36. Mehta, S. M., Jin, T., Stanciulescu, I. & Grande-Allen, K. J. Engineering biologically extensible hydrogels using photolithographic printing. *Acta Biomater.* **75**, 52–62 (2018).
37. Greene, T. & Lin, C.-C. Modular Cross-Linking of Gelatin-Based Thiol–Norbornene Hydrogels for in Vitro 3D Culture of Hepatocellular Carcinoma Cells. *ACS Biomater. Sci. Eng.* **1**, 1314–1323 (2015).
38. Goding, J. W. Conjugation of antibodies with fluorochromes: modifications to the standard methods. *J. Immunol. Methods* **13**, 215–226 (1976).
39. Ueda, M. J., Ito, T., Okada, T. S. & Ohnishi, S. I. A correlation between membrane fluidity and the critical temperature for cell adhesion. *J. Cell Biol.* **71**, 670–674 (1976).
40. Rico, F., Chu, C., Abdulreda, M. H., Qin, Y. & Moy, V. T. Temperature Modulation of Integrin-Mediated Cell Adhesion. *Biophys. J.* **99**, 1387–1396 (2010).
41. Hammel, J. H., Cook, S. R., Belanger, M. C., Munson, J. M. & Pompano, R. R. Modeling Immunity In Vitro: Slices, Chips, and Engineered Tissues. *Annu. Rev. Biomed. Eng.* (2021) doi:10.1146/annurev-bioeng-082420-124920.
42. Maharjan, S., Cecen, B. & Zhang, Y. S. 3D Immunocompetent Organ-on-a-Chip Models. *Small Methods* **4**, 2000235 (2020).
43. Griffith, L. G. & Swartz, M. A. Capturing complex 3D tissue physiology in vitro. *Nat. Rev. Mol. Cell Biol.* **7**, 211–224 (2006).
44. Pompano, R. R., Chiang, A. H., Kastrup, C. J. & Ismagilov, R. F. Conceptual and Experimental Tools to Understand Spatial Effects and Transport Phenomena in Nonlinear Biochemical Networks Illustrated with Patchy Switching. *Annu. Rev. Biochem.* **86**, 333–356 (2017).
45. McMurtrey, R. J. Analytic Models of Oxygen and Nutrient Diffusion, Metabolism Dynamics, and Architecture Optimization in Three-Dimensional Tissue Constructs with

Applications and Insights in Cerebral Organoids. *Tissue Eng. Part C Methods* **22**, 221–249 (2016).

46. Raza, A., Ki, C. S. & Lin, C.-C. The influence of matrix properties on growth and morphogenesis of human pancreatic ductal epithelial cells in 3D. *Biomaterials* **34**, 5117–5127 (2013).

47. Ahearne, M. Introduction to cell–hydrogel mechanosensing. *Interface Focus* **4**, (2014).

48. Goldshmid, R. & Seliktar, D. Hydrogel Modulus Affects Proliferation Rate and Pluripotency of Human Mesenchymal Stem Cells Grown in Three-Dimensional Culture. *ACS Biomater. Sci. Eng.* **3**, 3433–3446 (2017).

49. Kim, H. N. & Choi, N. Consideration of the Mechanical Properties of Hydrogels for Brain Tissue Engineering and Brain-on-a-chip. *BioChip J.* **13**, 8–19 (2019).

50. Schrott, W. *et al.* Study on surface properties of PDMS microfluidic chips treated with albumin. *Biomicrofluidics* **3**, 044101 (2009).

51. Chen, H.-C. Boyden Chamber Assay. in *Cell Migration: Developmental Methods and Protocols* (ed. Guan, J.-L.) 15–22 (Humana Press, 2005). doi:10.1385/1-59259-860-9:015.

52. Russell, L. N. & Lampe, K. J. Oligodendrocyte Precursor Cell Viability, Proliferation, and Morphology is Dependent on Mesh Size and Storage Modulus in 3D Poly(ethylene glycol)-Based Hydrogels. *ACS Biomater. Sci. Eng.* **3**, 3459–3468 (2017).

53. Akalin, O. B. & Bayraktar, H. Alteration of cell motility dynamics through collagen fiber density in photopolymerized polyethylene glycol hydrogels. *Int. J. Biol. Macromol.* **157**, 414–423 (2020).

4 Conclusions and Future Directions

4.1 Conclusions

In summary, we have described a protocol for in situ micropatterning of spatially organized biomaterials and 3D cell cultures on a microfluidic chip and established the impact of crosslinking chemistry on the storage modulus, stability, and spatial resolution of the patterns. By simply aligning a photomask prior to light exposure, the user may pattern a wide variety of design configurations in the xy-plane without altering the microfluidic housing. The resulting patterned cultures were modular and free-standing, without the need for physical supports such as micropillars to guide the hydrogel in place. Gelation chemistry had a significant impact on the accuracy and mechanical stability of patterned microfeatures. While features were patterned down to 100 μm in both GelSH and GelMA hydrogels, the GelSH hydrogels in stiffer formulations provided the highest accuracy and greater stability under fluid flow. Complex geometries such as concentric circles, architectural designs, and microarrays were all accessible, as were open flow paths to distribute media to the patterned 3D cultures. When used with thiol-ene polymerization chemistry, the micropatterning method had high specificity and low cytotoxicity with primary human cells. We envision that this micropatterning strategy will enable researchers to organize 3D cultures directly onto organs-on-chip in arrangements that capture the complexity of tissue organization, thus granting access to mechanistic experiments while maintaining control over cellular and fluidic components.

4.2 Future Work

4.2.1 *Enhancing T cell interactions in photopatterned hydrogels*

When thinking of applying this micropatterning strategy to create a lymph node on a chip (LN chip), cell motility is vital. An important behavior during an immune response is

the rapid and efficient motility of T cells in search of their antigen. At rest, T cells follow a modified random walk with 7 - 10 $\mu\text{m}/\text{min}$ average velocity, which slows to 1 – 4 $\mu\text{m}/\text{min}$ upon activation or inflammation of the tissue.¹ Prior scaffolds have been developed by other groups and have shown that upon introducing T cells, they are able to migrate at biomimetic speeds. A key architectural parameter in these scaffolds has been the pore size and pore inter-connectivity, with increased interconnectivity and pore sizes of $\sim 80 \mu\text{m}$ being preferable.^{2,3} At the moment, one of the unsolved problems is the constricted motility of cells within and across hydrogel regions. Based on this information, I am hypothesizing that an increase in the porosity, as well as the pore size, in our hydrogels will enhance T cell motility. Thus, I propose a method to create photo-patternable macroporous GelSH/PEGNB hydrogels.

Macro-porosity of hydrogels can be controlled by a variety of strategies including: 3D printing, cryotemplating and particle leaching. Additive manufacturing, like 3D printing grants exceptional control over pore distribution, given that the final architecture of the construct relies on information provided by a computer aided-design (CAD) file.⁴ On the other hand, cryotemplating relies on the formation and subsequent removal of ice crystals to introduce porosity. The general procedure for cryotemplating requires bringing the hydrogel precursor down to temperatures below $-10 \text{ }^\circ\text{C}$, to allow for ice crystal formation, crosslinking the frozen construct, followed by warming up the construct to melt the crystals, leaving behind pores.⁵ While the first two strategies have been successful at creating pore sizes in the range of a few μm 's to hundreds of μm 's⁴, their implementation with on-chip photopatterning is not straight-forward and in some cases, such as aggressive temperature shifts, could negatively impact cell viability. Alternatively, particle leaching consists of incorporating microspheres in the hydrogel precursor and subsequent dissolution using the appropriate solvent.⁴ Depending on the chemical composition of the

microparticles either organic or aqueous solvents could be used. Given the necessary presence of cells during photopolymerization on-chip, it would be preferable to use an aqueous, more biocompatible solvent.

Gelatin microspheres can be formed via an emulsification process, where a warm viscous gelatin solution is added drop-wise to a solution of cold oil that is constantly stirred. The formed microspheres can be sieved to separate them based on size. While previous studies have shown the ability to create gelatin microspheres using a bulk emulsification process,⁶⁻⁸ I have performed preliminary testing following published protocols and found it difficult to control the size of the spheres, with the majority being in the few hundreds of micron's scales, much larger than needed for this application. Additionally, mechanically sieving the spheres can be tricky, particularly with smaller particles being prone to bounce off. A solution to this problem can be found using droplet microfluidics. For this application, a T-junction geometry can be used for emulsification of the aqueous phase (gelatin) with oil phase (oil + surfactant) (Figure 4-1a). The size of the microspheres can be controlled by the channel dimensions as well as the ratio of flow rates, using the following equation:

Equation 4-1

$$\frac{L_D}{W} = \alpha_1 + \alpha_2 \frac{Q_{dispersed}}{Q_{continuous}}$$

where L_d is the length of the dispersed segments, W the width of the side channel, Q_{disp} and Q_{cont} are the volumetric flow rates of dispersed (aqueous) and continuous (oil) phase, respectively, and α_1 and α_2 , are of the order one and depend on the geometry of the T-junction.⁹

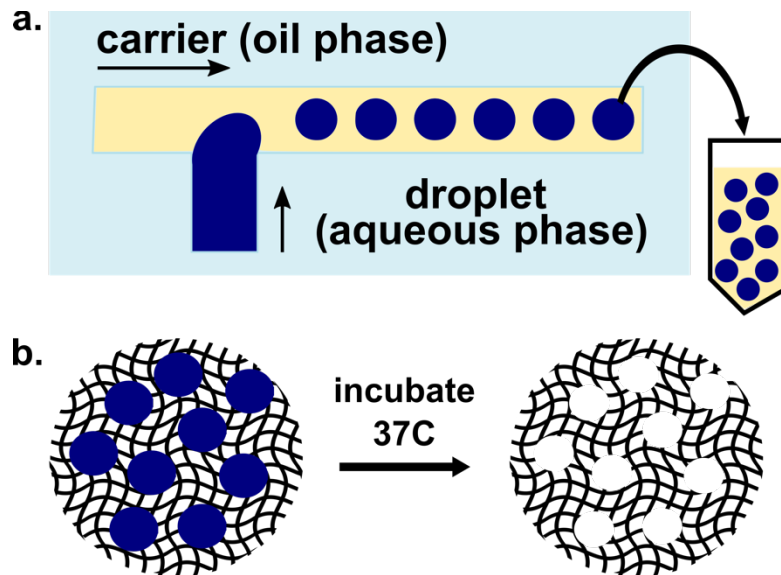


Figure 4-1 Synthesis of gelatin microspheres on chip. (a) Schematic of microsphere generation using T-junction microfluidic device. Carrier (yellow; oil phase) and aqueous gelatin solution (blue). Droplets generated and collected in a centrifuge tube. (b) Gelatin microspheres (blue) embedded in crosslinked matrix (black wavy lines). After hydrogel is formed, it is placed in 37°C which dissolves the gelatin, leaving behind a macro-porous scaffold.

The photopatterning process is ideal for incorporating of gelatin microspheres, given the cooling step which brings down the temperature of the inside of the chip to ~21 °C, ensuring that gelatin microspheres will not dissolve, until placed in the incubator at 37 °C (Figure 4-1b). Some fine tuning is to be expected by including microspheres during photo-crosslinking; as shown in the beginning of Chapter 3, inclusion of cells at high densities caused differences in the resulting storage moduli of hydrogels. It is recommended the *in situ* rheology measurements be taken to understand the impact of microspheres in the gelation kinetics of hydrogels, too many spheres may create mechanically unstable 3D cultures. Similar techniques have been used previously with PEG-based hydrogels to create macro-porous scaffolds.^{2,10} A particularly relevant

example is the work done by Irvine *et al*, in which a PEG-based macro-scaffold was created by colloidal templating and was used to investigate the motility of T cells². In this work, it was necessary to fill the pores with a collagen solution in order for cells to migrate at the correct speeds. These may not be the case in our gelatin-based system, since gelatin preserves the RGD motifs necessary for cell adhesion and migration, however it may mean that the architecture of the scaffold should be carefully examined to account for high levels of pore-interconnectivity. Once cell motility is confirmed in these new-generation of 3D patterned hydrogels, they can be integrated to test immune function on chip.

4.2.2 Establish T-B cell interactions on chip

Much has been learned from studying the lymph node *in vivo*, particularly by *in vivo* two-photon microscopy.¹¹⁻¹⁴ These studies investigated events such as cell motility, homing, lymphocyte differentiation during trafficking, lymphocyte interaction with dendritic cells, lymphocyte migration along stromal cell networks and T cell activation following antigen recognition. However, *in vivo* models can suffer from complexity, inaccessibility, and most importantly, a lack of experimental control over parameters such as ligand density and selective presentation, fluid flow, or cellular or molecular composition.¹³

In comparison to *in vivo* models, *in vitro* or *ex vivo* models often have to make assumptions and/or simplifications about extracellular matrix components, fluid flow patterns, or effects of multi-organ communication through recirculation, etc. However, parameters or conditions discovered through these reductionist models can be incorporated into more sophisticated platforms later on, allowing a continuous build-up of knowledge across laboratories and fields.

When looking at the literature and searching which *ex vivo* or *in vitro* models of immunity in the lymph node have been developed, it becomes clear that interactions between T cells and antigen presenting cells (APC's) are very popular. Particularly interactions between T cells and dendritic cells, the general approaches to model these are summarized on Figure 4.2. Examples of these models include studying the chemotactic response of T cells to CCL19 and CCL21^{15,16}, interactions between T:DC following capture in microwells,¹⁷ the influence of shear stress during T cell priming and activation¹⁸, and the chemotactic ability of dendritic cells during antigen presentation¹⁹.

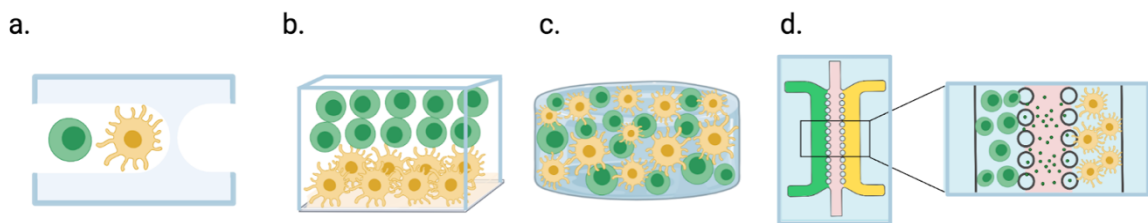


Figure 4-2 Current approaches to modeling T cell (green) - DC (yellow) interactions. a) Pairwise trapping of cells in microwells. b) 2D monolayer of cells with cell suspension added above. c) 3D culture of mixed cells. d) Cells seeded in distinct regions of a microchip to investigate chemotaxis.

Less studied, are interactions between T and B cells. This is an important phenomenon to study because production of long-lived, high affinity antibodies against a T-dependent antigen requires cognate interaction between T and B cells.²⁰ For the initial step of corroborating complex immune function on chip, I propose a study that will track the response of T and B cells to a superantigen, Staphylococcal Enterotoxin B (SEB), which activates up to 20% of human T cells, in contrast to typical antigens that activate < 1 in 10^5 T cells.²¹ The experiment is designed to take advantage of the spatial organization accessible through the photopatterning method; the workflow and expected outcomes are outlined in Figure 4-3. For the initial stages of these experiments, cells will be differentiated

on-chip and loaded. However, future iterations could start with naïve T cells and B cells to corroborate the process of differentiation can take place on chip.

The first stage of the experiment, will require creating a 3D region that contains a mixed population of Tfh's and B cells (Figure 4-3a). In the presence of SEB, a random distribution of cells is expected, since cells will be migrating through the matrix. However, in the presence of SEB, we expect to see T cells creating stable long-lived conjugates with B cells, in the scale of 10- 40 min, although it has been shown some interactions can persist > an hour, whereas noncognate interactions are expected to dissociate in less than 10 min.²³ Ideally, these visual outcomes could be confirmed through antibody staining to show change in activation states by both T and B cells, which would include upregulation in surface expression of CD40 and CD40L, respectively.

The second stage, would separate B cells and T cells in distinct regions, as they would be found in the native LN tissue, in the B follicular area and the paracortex, respectively (Figure 4-3b). This configuration would introduce a physical barrier between the cell types and would test the directed migration of B cells towards the interfollicular zone. While we expect cells to be able to migrate both within and between hydrogel zones, it would be interesting to see if there are differences in the distances or the number of cells that make it from one zone to the other. Prior work with other types of lymphocytes has shown that even within a given cell type, there are subpopulations that have enhanced migratory ability through sub-continuous matrices.²⁴

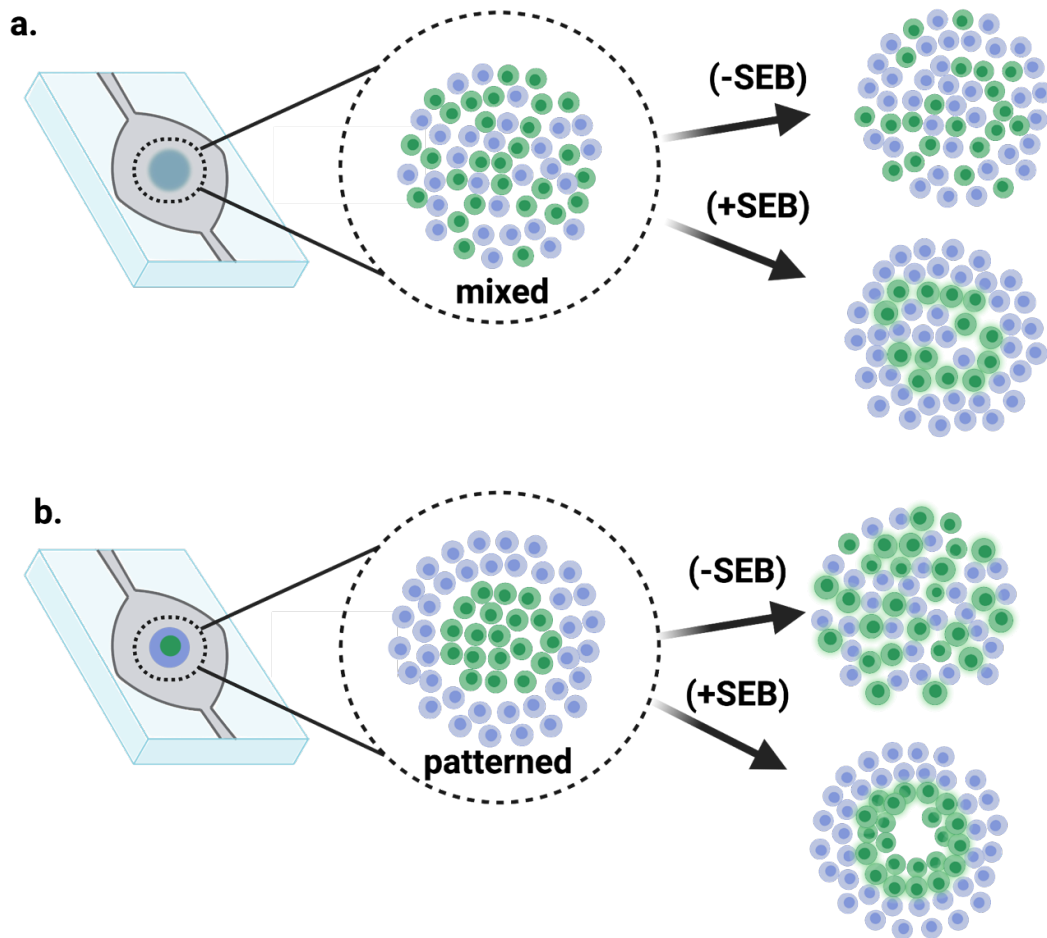


Figure 4-3 T_{FH} cells (blue) and B cells (green). a) Mixed population of T and B cells. In the absence of SEB, cells will be scattered heterogeneously across hydrogel, whereas in presence of SEB will form T-B conjugated. b) Separated two-region co-culture of T and B cells, in biomimetic organization of B-cell follicle/T cell zone.

In addition, we would expect to see the same type of long-lived conjugates between T and B cells, but perhaps in a more evident manner by accumulation at the T-B interface. Similar staining of surface markers should be performed to corroborate function.

4.3 References

1. Worbs, T. & Förster, R. T Cell Migration Dynamics Within Lymph Nodes During Steady State: An Overview of Extracellular and Intracellular Factors Influencing the Basal Intranodal T Cell Motility. in *Visualizing Immunity* (eds. Dustin, M. & McGavern, D.) 71–105 (Springer, 2009). doi:10.1007/978-3-540-93864-4_4.
2. Stachowiak, A. N. & Irvine, D. J. Inverse opal hydrogel-collagen composite scaffolds as a supportive microenvironment for immune cell migration. *J. Biomed. Mater. Res. A* **85A**, 815–828 (2008).
3. Pérez del Río, E. *et al.* CCL21-loaded 3D hydrogels for T cell expansion and differentiation. *Biomaterials* **259**, 120313 (2020).
4. Nicol, E. Photopolymerized Porous Hydrogels. *Biomacromolecules* **22**, 1325–1345 (2021).
5. Thomas, A. M. & Shea, L. D. Cryotemplation for the rapid fabrication of porous, patternable photopolymerized hydrogels. *J. Mater. Chem. B* **2**, 4521–4530 (2014).
6. Park, H., Temenoff, J. S., Holland, T. A., Tabata, Y. & Mikos, A. G. Delivery of TGF- β 1 and chondrocytes via injectable, biodegradable hydrogels for cartilage tissue engineering applications. *Biomaterials* **26**, 7095–7103 (2005).
7. Wang, L., Lu, S., Lam, J., Kasper, F. K. & Mikos, A. G. Fabrication of Cell-Laden Macroporous Biodegradable Hydrogels with Tunable Porosities and Pore Sizes. *Tissue Eng. Part C Methods* **21**, 263–273 (2015).
8. Goh, M. *et al.* In situ formation of injectable and porous heparin-based hydrogel. *Carbohydr. Polym.* **174**, 990–998 (2017).

9. van Steijn, V., Kreutzer, M. T. & Kleijn, C. R. μ -PIV study of the formation of segmented flow in microfluidic T-junctions. *Chem. Eng. Sci.* **62**, 7505–7514 (2007).
10. Akalin, O. B. & Bayraktar, H. Alteration of cell motility dynamics through collagen fiber density in photopolymerized polyethylene glycol hydrogels. *Int. J. Biol. Macromol.* **157**, 414–423 (2020).
11. Miller, M. J., Wei, S. H., Cahalan, M. D. & Parker, I. Autonomous T cell trafficking examined in vivo with intravital two-photon microscopy. *Proc. Natl. Acad. Sci.* **100**, 2604–2609 (2003).
12. Mempel, T. R., Henrickson, S. E. & von Andrian, U. H. T-cell priming by dendritic cells in lymph nodes occurs in three distinct phases. *Nature* **427**, 154–159 (2004).
13. Bajénoff, M. *et al.* Stromal Cell Networks Regulate Lymphocyte Entry, Migration, and Territoriality in Lymph Nodes. *Immunity* **25**, 989–1001 (2006).
14. Bajénoff, M., Glaichenhaus, N. & Germain, R. N. Fibroblastic Reticular Cells Guide T Lymphocyte Entry Into and Migration Within the Splenic T Cell Zone. *J. Immunol.* **181**, 3947–3954 (2008).
15. Nandagopal, S., Wu, D. & Lin, F. Combinatorial Guidance by CCR7 Ligands for T Lymphocytes Migration in Co-Existing Chemokine Fields. *PLOS ONE* **6**, e18183 (2011).
16. Loef, E. J., Sheppard, H. M., Birch, N. P. & Dunbar, P. R. Live-Cell Microscopy Reveals That Human T Cells Primarily Respond Chemokinetically Within a CCL19 Gradient That Induces Chemotaxis in Dendritic Cells. *Front. Immunol.* **12**, (2021).
17. Faley, S. *et al.* Microfluidic platform for real-time signaling analysis of multiple single T cells in parallel. *Lab. Chip* **8**, 1700–1712 (2008).
18. Rosa, P. M., Gopalakrishnan, N., Ibrahim, H., Haug, M. & Halaas, Ø. The intercell dynamics of T cells and dendritic cells in a lymph node-on-a-chip flow device. *Lab. Chip* **16**, 3728–3740 (2016).

19. Mitra, B. *et al.* Microdevice integrating innate and adaptive immune responses associated with antigen presentation by dendritic cells. *RSC Adv.* **3**, 16002–16010 (2013).
20. Cassatt, D. R. & Cohen, D. A. ARTIFICIAL T CELL:BCELLCONJUGATION. 9.
21. Li, H., Llera, A., Malchiodi, E. L. & Mariuzza, R. A. The structural basis of T cell activation by superantigens. *Annu. Rev. Immunol.* **17**, 435–466 (1999).
22. Acharya, K. R. *et al.* Structural basis of superantigen action inferred from crystal structure of toxic-shock syndrome toxin-1. *Nature* **367**, 94–97 (1994).
23. Okada, T. *et al.* Antigen-Engaged B Cells Undergo Chemotaxis toward the T Zone and Form Motile Conjugates with Helper T Cells. *PLOS Biol.* **3**, e150 (2005).
24. McMinn, P. H., Hind, L. E., Huttenlocher, A. & Beebe, D. J. Neutrophil trafficking on-a-chip: an in vitro, organotypic model for investigating neutrophil priming, extravasation, and migration with spatiotemporal control. *Lab. Chip* **19**, 3697–3705 (2019).